UNIVERSITY OF TOURS

DOCTORAL SCHOOL SSBCV

EA6295 NanoMedecines and NanoProbes

Ph.D. Thesis

presented by:

Mathias PACAUD

Defended on the **16th of december 2019**

For the grade of: **Doctor of the University of Tours**

Discipline/Speciality: **Chemistry**

Synthesis and physico-chemical evaluation of gold nanoflowers (AuNFs) as new substrates for bioanalytical SERS

Ph.D. Thesis directed by:

Mr. CHOURPA Igor	Professor, University of Tours
Mr. FAHMI Amir	Professor, University of applied sciences of Kleve

REFEREES:

Mrs. BEGIN-COLIN Sylvie	Professor, University of Strasbourg
Mr. SOCKALINGUM Ganesh	Professor, University of Reims

JURY:

Mr. CHOURPA Igor	Professor, University of Tours
Mr. FAHMI Amir	Professor, University of applied sciences of Kleve
Mrs. HERVE-AUBERT Katel	Lecturer - HDR, University of Tours
Mrs. BEGIN-COLIN Sylvie	Professor, University of Strasbourg
Mr. SOCKALINGUM Ganesh	Professor, University of Reims
Mr. BOUAKAZ Ayache	Research supervisor, University of Tours

Un chapitre s’achève pour qu’un autre commence.

ACKNOWLEDGEMENTS

First of all, I would like to personally thank all those who participated in this thesis, directly or indirectly, for their support, presence, and advice.

I would particularly like to thank Mr. Igor Chourpa, Professor and director of the EA 6295 Nanomedicines and Nanoprobes laboratory at the University of Tours and Mr. Amir Fahmi Professor and director of a laboratory at Hochschule Rhein-Waal University of Applied Sciences who agreed to supervise me throughout this thesis and shared with me their brilliant intuitions and for welcoming me to their teams. I am very grateful to them for having supported me throughout these 3 years despite the extra work it may have required.

I would also like to thank Mrs. Katel Hervé-Aubert, lecturer and co-supervisor of this Ph.D. thesis, for her involvement in this project all along these 3 years and for the time she has devoted to the various reading and corrections of this manuscript.

I would like to thank all the MINERVA project members and collaborators, in particular, Mr. Alexey V. Feofanov, Professor and director of a laboratory at Shemyakin and Ovchinnikov Institute of Bioorganic Chemistry of Moscow for its work in the biological part of the project and its contribution to my first publication, Ms. Anastasiya Ignatova that I had the chance to meet in Moscow, Mr. Markus Heildelmann and Mr. Julien Burlaud-Gaillard for the TEM images of my samples and their teaching on the use of the microscope, Ms. Hiba Chamekh and Ms. Marion Cousin for their work on the gold nanoflowers, Ms. Alaa Makki and Mr. Franck Bonnier for their help on the spectroscopic part of this Ph.D. thesis and Mr. Martin Soucé who always take time to help and answer questions.

I would like to thank Mrs. Sylvie Begin-Colin, Professor, and director of the ECPM at the University of Strasbourg, and Mr. Ganesh Sockalingum, Professor at the Department of Pharmacy of the University of Reims, for the honor they have given me by agreeing to be referees for this Ph.D. thesis.

I would like to thank all the members of both teams, who took the time to answer to my questions and advised me all along these 3 years.

I do not forget to thank the whole group of masters/Ph.D. students/postdocs: Louise van Gheluwe, Christophe Eklouh-Molinier, Linda Miloudi, Sahar Fadlalla, Joacquim Pena, Lucia Lombardi, Sanaa Ben Djemaa, Viraj Nirwan, Yuri Dančík, Hichem Kichou, Alaa Makki, Duygu Disçi, Vladimir Astachov, Almar Assaad, Vinh Nguyen, Jonathan Bruniaux, Dilshad Hussein, Hiba Chamekh, and Kamilia Kemel. These years would not have been the same

without all of you. Thank you for the support, the affection, the laughs and the exchanges we shared.

I thank my whole family, to always have respected my choices and always ready to support me.

I thank also Christa and Debby Zimmermann for their support, their help and all the good moments we had together during my time in Germany.

RÉSUMÉ

Les nanostructures métalliques anisotropes font l'objet d'études intensives dont le nombre croît de façon spectaculaire. L'intérêt immense vers de tels nano-objets s'explique par des propriétés uniques qu'ils procurent et qui peuvent servir dans divers domaines, dont les applications biomédicales. Dans le cas de nanostructures d'or, on profite de l'inertie chimique de ce métal et on cherche à maitriser ses propriétés optiques liées aux oscillations collectives d'électrons de surface appelées plasmons de surface. Les nano-objets d'or de forme anisotrope telles que les nanofleurs (AuNFs) étudiées dans cette thèse possèdent une bande de résonance plasmonique localisée de surface (LSPR comme *localized surface plasmon resonance*) située dans le rouge - proche infrarouge (proche IR) (> 600 nm), tandis que celle des nanosphères d'or se situe dans le vert (520-530 nm). La capacité des AuNFs d'interagir avec la lumière rouge - proche IR les rend intéressantes en tant qu'agent d'imagerie optique et opto-accoustique, puisque les tissus biologiques sont plus transparents dans cette région spectrale. Dans le cas particulier de la diffusion Raman exaltée de surface (SERS, comme *surface-enhanced Raman scattering*), les AuNFs sont capables de procurer de multiples zones d'exaltation, comme leurs pointes et les jonctions entre leurs pétales appelées « hot spots ». Par conséquent, on peut les utiliser comme substrat SERS sans avoir besoin de les agréger, à la différence des nanosphères d'or. Afin de pouvoir profiter de tels avantages, on a besoin de protocoles de synthèse fiables et efficaces. Malheureusement, malgré le fait que de nombreux articles sont publiés sur ce sujet, il n'existe à ce jour pas de protocole de synthèse des AuNFs que l'on pourrait qualifier de « gold standard ».

Dans le cadre de cette thèse, nous avons proposé un nouveau protocole (brevet en cours et une publication parue) de synthèse des AuNFs qui surpasse pratiquement toutes les limites des protocoles publiés précédemment. À la différence des protocoles complexes et peu fiables décrits dans la littérature, notre protocole de synthèse des AuNFs est rapide, en une seule étape et n'utilise qu'un nombre réduit de réactifs connus qui sont peu ou pas toxiques. De plus, notre protocole permet de contrôler les caractéristiques des AuNFs telles que la taille et la position de la bande LSPR, entre 600 et 900 nm. Afin de garantir une stabilité colloïdale dans des milieux divers, nous avons enrobé nos AuNFs avec des polymères biocompatibles (alginates, chitosan, Pluronics, PVP et PEG) ou les avons encapsulées dans une matrice de silice. La caractérisation physico-chimique de ces nanosystèmes a été réalisée au moyen de la MET (microscopie

électronique en transmission), de la diffusion dynamique de la lumière (notée DLS comme *dynamic light scattering*) et de la spectroscopie d'absorption UV-visible. De plus, nous avons étudié les effets de ces enrobages sur l'intensité et la forme de spectres SERS d'un chromophore, le bleu de nil (noté NB comme *Nile blue*), fluorescent dans le proche infrarouge. Les substrats colloïdaux à base de ces AuNFs enrobées d'enveloppes biocompatibles ont ainsi montré leur potentiel pour procurer l'effet SERS sans agrégation et permettre l'analyse ultrasensible de petits chromophores. De plus, nos résultats montrent que ces nouveaux substrats sont capables de délivrer une charge de molécules dans des cellules cancéreuses. Leur détection dans les cellules a été démontrée, en utilisant les modalités SERS, fluorescence et diffusion élastique de lumière. Ainsi, ils semblent prometteurs en tant qu'agents théranostiques, applicables non seulement en SERS, mais également en imagerie optique et en thérapie.

Mots clés: Nanofleurs d'or, AuNF, plasmon de surface, spectroscopie SERS.

ABSTRACT

Anisotropic metallic nanostructures are nowadays the object of intensive studies, their number increases dramatically. The immense interest in such nano-objects can be explained by the unique properties that they provide which can be used in various fields, including biomedical applications. In the case of gold nanostructures, one can take advantage of the chemical inertness of this metal and can try to control its optical properties related to the collective oscillations of surface electrons called surface plasmons. The gold nano-objects of anisotropic form, such as the nanoflowers (AuNFs) studied in this thesis, have a localized surface plasmon resonance band (LSPR) located in the red - near-infrared (NIR) region (> 600 nm), while that of gold nanospheres is situated in the green (520-530 nm). The ability of AuNFs to interact with NIR light makes them attractive as optical and opto-acoustic imaging agents, since biological tissues are more transparent to the light within the NIR region. In the particular case of surface-enhanced Raman scattering (SERS), AuNFs are able to provide multiple areas of enhancement, like the tips of their petals and junctions between their petals called "hot spots". Thus, they can be used as SERS substrates without the need to aggregate them, unlike gold nanospheres. In order to benefit from such advantages, reliable and efficient synthesis protocols are needed. Unfortunately, despite the fact that thousands of articles are published on this subject, to date there is no protocol for the synthesis of the AuNFs that could be described as "gold standard".

As part of this thesis, we have proposed a new protocol (patent in progress, a paper published) of synthesis of the AuNFs which surpasses practically all the limits of the protocols published before. Unlike the complex and unreliable protocols described in the literature, our protocol for the synthesis of the AuNFs is fast, single-step and uses only a small number of known reagents which are slightly or not toxic. In addition, our protocol allows to control the characteristics of the AuNFs such as the size and the position of their LSPR band, between 600 and 900 nm. To ensure a good colloidal stability in various media, we coated our AuNFs with biocompatible polymers (alginates, chitosan, Pluronics, PVP and PEG) or encapsulated them in a silica matrix. The physico-chemical characterization of these nanosystems was carried out using TEM (scanning electron microscopy), DLS (dynamic light scattering) and UV-visible spectroscopy. In addition, we studied the effects of these coatings on the intensity and shape of the SERS spectra of a fluorescent chromophore named Nile blue (NB) emitting in the NIR

region. The colloidal substrates based on our AuNFs coated with biocompatible shells have thus shown their potential to provide the SERS effect without the need to their aggregation and to allow ultra-sensitive analysis of small chromophores. In addition, our results show that these novel substrates are able to deliver a molecular cargo to cancer cells. Their detection in cells has been demonstrated, using several modalities, namely fluorescence, SERS and elastic light scattering. Thus, they appear promising as theranostic agents, applicable not only in SERS, but also in multimodal optical imaging and therapy.

Key words: Gold nanoflowers, AuNF, surface plasmon, SERS spectroscopy.

TABLE OF CONTENT

RÉSUMÉ ... 3
LIST OF TABLES ... 11
LIST OF FIGURES ... 12
LIST OF ABBREVIATIONS ... 16
INTRODUCTION GÉNÉRALE *(French version)* ... 18
GENERAL INTRODUCTION *(English version)* ... 21
CHAPTER I. ANALYSIS OF LITERATURE. Raman and surface-enhanced Raman scattering (SERS) bioanalytical spectroscopy ... 24
1. Raman spectroscopy ... 24
1.1. History ... 24
1.2. What is the Raman spectroscopy? ... 25
1.3. Raman scattering process ... 25
1.4. Complementarity of Raman with IR ... 28
1.5. Raman spectrometers ... 29
1.6. Bioanalytical Raman spectroscopy ... 31
2. Surface-enhanced Raman scattering (SERS) ... 32
2.1. History ... 32
2.2. Mechanisms of enhancement of the Raman scattering ... 32
2.3. 3D substrates for SERS spectroscopy ... 33
2.4. Colloids of conventional sphere-like NPs as SERS substrates ... 38
2.5. Gold colloids as aggregation-free SERS substrates ... 39
2.5.1. Core-multishell NPs (nanomatryoshka) ... 39
2.5.2. Anisotropic NPs ... **Erreur ! Signet non défini.**
2.6. Coating of the AuNPs to increase their colloidal stability ... 44
2.7. Coating of the AuNPs to increase their biocompatibility and stealthiness against the immune system. ... 46
2.8. Functionalization of the AuNPs to expand their targeting capabilities ... 47
CHAPTER II. MATERIALS AND METHODS ... 50
1. Characterization techniques and instruments ... 50
1.1. Raman spectroscopy ... 50

1.1.1. Raman technique 50
1.1.2. Raman spectrometer 50
1.1.3. Preparation & measurements of the SERS samples 51
1.2. UV-visible absorption spectroscopy 52
1.2.1. UV-visible absorption technique 52
1.2.2. UV-visible absorption instrument 52
1.2.3. Preparation & measurements of the UV-visible samples 53
1.3. Dynamic light scattering (DLS) spectroscopy 53
1.3.1. DLS technique 53
1.3.2. DLS instrument 54
1.3.3. Preparation & measurements of the DLS samples 54
1.4. Transmission electron microscopy (TEM) 55
1.4.1. TEM technique 55
1.4.2. TEM instrument 56
1.4.3. Preparation & measurements of the TEM samples 56
2. Protocols of synthesis 57
2.1. Preparation of the surfactant-free AuNFs 57
2.2. Preparation of the polymer-coated AuNFs 58
2.3. Preparation of silica-coated AuNFs 60
CHAPTER III. RESULTS. Synthesis of novel SERS substrates in a form of gold nanoflowers (AuNFs) 61
Introduction *(French version)* 61
Introduction *(English version)* 63
CHAPTER IV. RESULTS. Stabilization of the gold nanoflowers using surface coating 73
Introduction *(French version)* 73
Introduction *(English version)* 74
1. Time-dependant evolution of the AuNF colloids 75
2. Effect of the temperature on the synthesis of the AuNFs 78
3. Effect of the AuNF coating with polymers other than PVP (PEG, Pluronics F68 and F127, alginates and chitosan) 80
3.1. Coating the AuNFs with polyethylene glycol (PEG) 81
3.1.1. Effect of PEG on the chemical and colloidal stability of the AuNFs 82
3.1.2. Effect of PEG on the SERS activity of the AuNFs 84

3.2. Coating the AuNFs with the Pluronics F68 & F127 84
3.2.1. Effect of Pluronics F68 and F127 on the chemical and colloidal stability of the AuNFs. 85
3.2.2. Effect of poloxamers on the SERS activity of the AuNFs 87
3.3. Coating the AuNFs with the alginates 87
3.3.1. Effect of alginate on the chemical and colloidal stability of the AuNFs 88
3.3.2. Effect of alginates on the SERS activity of the AuNFs 89
3.4. Coating the AuNFs with the chitosan 90
3.4.1. Effect of chitosan on the chemical and colloidal stability of the AuNFs 90
3.4.2. Effect of chitosan on the SERS activity of the AuNFs 91
3.4.3. Effect of the pH (pH = 7 and pH = 5) 91
3.5. Comparison of the effect between the different polymers on the SERS activity of the AuNFs 94
4. Silica coating of the AuNFs 95
4.1. Effect of silica shell on chemical and colloidal stability of the AuNFs 95
4.2. Effect of the AuNF pre-coating with PVP on the silica shell 98
4.3. Encoding the silica-coated AuNFs with Nile blue 99
4.3.1. Effect of the NB on the silica shell formation and on the LSPR bands 100
4.3.2. Effect of the NB inclusion method on the SERS activity of the silica-coated AuNFs 101
DISCUSSION GÉNÉRALE *(French version)* 103
1. Un nouveau protocole de synthèse de substrats SERS respectant les contraintes bionanalytiques 103
2. Capacité de ce protocole à ajuster la position de la bande plasmonique à la longueur d'onde souhaitée 104
3. Les faiblesses et limites des nanofleurs d'or 105
4. Amélioration de la stabilité et fonctionnalisation des AuNFs par habillage 105
CONCLUSION GÉNÉRALE *(French version)* 109
PERSPECTIVES *(French version)* 110
1. Imagerie bioanalytique et nanovectorisation de médicaments 110
2. Les AuNFs comme base de nanosondes multimodales magneto-plasmoniques . 110
GENERAL DISCUSSION *(English version)* 112

1. **A new synthesis protocol of SERS substrate respecting bioanalytical constraints** 112
2. **Tunability of the LSPR band characteristics brought by this protocol** 113
3. **Weaknesses and limitations of the AuNFs** 113
4. **Improvement of the stability and functionalization of the AuNFs by coating** ... 114

GENERAL CONCLUSION ***(English version)*** 117

PERSPECTIVES ***(English version)*** 118

1. **Bioanalytical imaging and drug delivery** 118
2. **The AuNFs as a base for the design of magneto-plasmonic multimodal nanoprobes** 118

REFERENCES 120

ANNEX 1. Fluorescence Microscopy as a Tool for Nanomedicine-Cell Interactions Study: Input of Particle Design and of Analytical Strategy 130

LIST OF TABLES

Table I. Table showing the different concentrations of the MPTES solutions used to coat the surfactant-free and the PVP-coated AuNFs with their corresponding R3 defined as the MPTES/Au molar ratio. 60

Table II. Table presenting the position of the main studied peaks on the SERS spectra in all the sections below within this chapter. 82

LIST OF FIGURES

Figure 1. Schematic showing the elastic (Rayleigh) and inelastic (Raman Stokes) scattering of the photons on an organic molecule (Nile blue in this study). $n_{Rayleigh}$ and n_{Raman} represent respectively the number of photons corresponding to the elastic and inelastic scattering. 25

Figure 2. A: Jablonski diagram of the energy levels involved in IR absorption, Raman and Rayleigh scattering, resonant Raman scattering and fluorescence emission where the "E" represent an electron energy levels and the "ν" represent vibrational energy levels. B: Schematic presentation of intensities of the three types of light scattering (from left to right: Raman Stokes, Rayleigh, and Raman anti-Stokes). 27

Figure 3. Schematic comparing the activity of vibrational modes in IR absorption and Raman scattering for a carbon dioxide molecule. 28

Figure 4. Schematic of typical Raman instrumental setup for macroscopic (A) and microscopic (B) samples analysis. 30

Figure 5. A: Schematic presentation of how the localized surface plasmon is excited by the incident light at the surface plasmon resonance frequency. B: Simulated distribution of plasmon-enhanced electric field around the NP showing the dependence on the distance from the NP surface of the SERS effect [5]. 34

Figure 6. Schematic of the SERS phenomenon as a short-range phenomenon. 35

Figure 7. A: "Hot spot" corresponds to a high electromagnetic field created in the junction (gap) between two plasmonic nanoparticles. B: SERS enhancement decrease with the increase of the interparticle distance [5]. 36

Figure 8. Typical UV-visible absorption of spherical AgNPs (grey curve), spherical AuNPs (red curve), and gold nano-seeds (GNS) around 1 - 2 nm of diameter (brown curve). ... 37

Figure 9. Gold nanomatryoshka (AuNM) synthesis. [18]. 40

Figure 10. A: Left: 3D scheme of a gold nanoflower and TEM image of AuNFs produced in this work. Right: Left: 3D scheme of a gold nanorod and TEM image of AuNRs from Vigderman et al. [15]. B: Typical UV-visible absorption spectra given by both anisotropic gold NPs. 42

Figure 11. Schematic of typical gold AuNRs on which the two plasmon resonance modes are shown. 42

Figure 12. Schematic of a typical AuNS showing the strong increase of the magnetic field at the tip of the petals and the junctions at their base where the Raman is the most enhanced. 43
Figure 13. Schematic of gold stabilized nanoparticles 45
Figure 14. Conformation of PEG molecules grafted on the surface of spherical nanoparticles. 45
Figure 15. Picture of the Raman spectrometer that was used for our SERS characterizations. The arrows show the sample holder position on the spectrometer and the P96 multiwell plate position on the sample holder. 51
Figure 16. Picture of the UV-visible absorption spectrophotometer that was used to characterize the LSPR band position, intensity and shape of our AuNPs. The arrows show the sample holder position on the spectrometer and the cuvette position in the sample holder. 53
Figure 17. Picture of the DLS spectrometer that was used for our AuNFs hydrodynamic size and zeta potential characterizations. The arrows show the sample holder position on the spectrometer and the cuvette position in the sample holder. 54
Figure 18. Picture of the Transmission electron microscope that was used to observe the 2D morphology of our nano-objects. The arrows show the sample holder position on the microscope and the grid position on the sample holder. The picture of the microscope and the grid holder are from www.jeolusa.com and the picture of the grid is from www.2spi.com. 56
Figure 19. A: Evolution over the time of the absorbance spectra of the surfactant-free AuNFs. B: Diagram showing the evolution of the LSPR band position of the surfactant-free AuNFs. C: Comparison of the absorbance spectra. D: TEM micrographs. 76
Figure 20. A**:** Evolution over the time of the absorbance spectra. B: Diagram showing the evolution of the position of the maximum absorption peak 76
Figure 21. A: Stability over the time of the LSPR band of the AuNF@PVP. B: Comparison of the absorbance spectra of the AuNF@PVP batch before (black curve) and once centrifugated twice then aged of 2 min, 24 h, 3, 7, 10 and 14 days. 77
Figure 22. LSPR bands of AuNF synthesized at two different temperatures, 0°C and 25°C, at NH_2OH/NaOH molar ratio R = 0.3 (dashed grey and solid black curves, respectively) and R = 0.6 (dashed pink and solid red curves respectively). The spectra were normalized on the intensity of the black curve at 400 nm, for easier comparison. 78

Figure 23. TEM analysis of the AuNFs synthesized at 0°C and 25°C at R = 0.3 and 0.6. All the pictures are on the same scale. The histograms below show the distribution of the AuNF size, petal length, and width as seen in the TEM images. For the size, two orthogonal diameters were measured on each of 60 nanoflowers randomly selected for each batch. The petals' length and width were measured as shown in the schemes at the bottom. 79
Figure 24. Chemical structure of Polyvinylpyrrolidone (PVP)..... 81
Figure 25. Chemical structure of PEG. 81
Figure 26. A: Effect of PEG on the LSPR band of the AuNFs. B: Effect of the Nile blue (NB) on the LSPR band of the PEG-coated AuNFs. C: Effect of PEG on the AuNF morphology. D: Effect of PEG on the SERS spectra of NB. E: Histogram representing the intensity ratio of the main SERS bands of NB 83
Figure 27. Chemical structure of a poloxamer composed of EO and PO arranged in a triblock structure. 85
Figure 28. A: Effect of poloxamers on the LSPR band of the AuNFs. B: Effect of the Nile blue (NB) on the LSPR band of the poloxamer-coated AuNFs. C: Effect of poloxamers on the SERS spectra of NB. D: Histogram representing the intensity ratios of the main SERS bands of NB 86
Figure 29. Chemical structure of alginate polymer composed of M and G monomers. 88
Figure 30. A: Effect of alginate on the LSPR band of the AuNFs. B: Effect of the Nile blue on the LSPR band of the alginate-coated AuNFs. C: Effect of alginate on the SERS spectra of NB. D: Histogram representing the intensity ratios of the main SERS bands of NB.. 89
Figure 31. Chemical structure of chitosan..... 90
Figure 32. A: Effect of chitosan on the LSPR band of the AuNFs. B: Effect of the Nile blue on the LSPR band of the chitosan-coated AuNFs. C: Effect of chitosan on the SERS spectra of NB. D: Histogram representing intensity ratio of the main SERS bands of NB. 91
Figure 33. Effect of pH on the chitosan-coated AuNFs. 92
Figure 34. Effect of the pH on the SERS activity of NB at 1 µmol/L on the chitosan-coated AuNFs. 92
Figure 35. A: Comparison of the NB SERS spectral shape on the AuNFs coated with the different polymers. B: The NB SERS spectra representing the two most distinct shapes observed in this study. C: Histogram of the SERS bands intensity ratio from the spectra. 94

Figure 36. A: Typical TEM images of silica shell thickness on the AuNFs. B: LSPR band of the AuNFs freshly synthesized (grey) and silica-coated. C and D: Diagrams representing respectively the evolution of the LSPR band maximum 97

Figure 37. A: Typical TEM images of silica shell thickness on the AuNFs. B: LSPR band of the AuNFs freshly synthesized (solid) and silica-coated 99

Figure 38. Influence of the NB addition modalities on the structure of the silica shell of the AuNFs (R3 = 1). A: TEM pictures of AuNFs coated with silica. B: LSPR bands of 3 reproduced batches. C: Comparison of silica-coated AuNFs prepared with and without NB. 101

Figure 39. Influence of the NB addition modalities on the SERS/fluorescence activity of silica-coated AuNFs. A: SERS spectra. B: Intensity ratio of main SERS bands of NB. C: SERS and fluorescence signals 102

LIST OF ABBREVIATIONS

Acronyms	Definitions
AgNP	Silver nanoparticle
AuNF@PEG	PEGylated AuNF(s)
AuNF@PVP	PVP-coated gold nanoflower(s)
AuNF@SPION	SPION-coated gold nanoflower(s)
AuNFs	Gold nanoflowers
AuNM	Gold nanomatryoshka
AuNP	Gold nanoparticle
AuNR	Gold nanorod
AuNS	Gold nanostar
AuNU	Gold nanoourchin
BET	Brunauer, Emmett and Teller Theory
CDD	Charge-coupled device
CE	Chemical enhancement
CPP	Cell-penetrating peptide
C-SPION	Citrated SPION
CTAB	Cetyl trimethylammonium bromide
CVD	Chemical vapor deposition
D_H	Hydrodynamic diameter
DLS	Dynamic light scattering
EM	Electromagnetic mechanism
EPR	Enhanced permeability retention
FA	Folic acid
FDA	Food and drug administration
FR	Folate receptor
GNS	Gold nanoseed
HER2	Human epidermal growth factor receptor 2
HIV-1	Human immunodeficiency virus type 1
IR	Infrared
IRM	Imagerie par resonance magnétique
LSPR	Localized surface plasmon resonance
MET	Microscopie électronique en transmission
MRI	Magnetic resonance imaging
Na_3Cit	Trisodium citrate
NF	Nanoflower
NIR	Near-infrared
NM	Nanomatryoshka
NP	Nanoparticle
NR	Nanorod
NU	Nanourchin
PEG	Polyethylene glycol
PEO	Poly(ethylene oxide)

PPO	Poly(propylene oxide)
P-SPION	PEGylated SPION
R	NH_2OH / NaOH molar ratio
R2	Polymer / Au w/w ratio
R3	MPTES / Au molar ratio
RR	Resonant Raman
RS	Raman scattering
SBF	Simulated body fluid
ScFv	Single-chain fragment variable
SEF	Surface-enhanced fluorescence
SERS	Surface-enhanced Raman scattering
SHINERS	Shell-isolated nanoparticle-enhanced Raman scattering
SiRNA	Small interfering ribonucleic acid
SPION	Superparamagnetic iron oxide nanoparticle
SPR	Surface plasmon resonance
Tat	Trans-activator of transcription
TEM	Transmission electron microscopy
TNBC	Triple-negative breast cancer
UV	Ultraviolet
UV-Vis	UV-Visible absorption spectroscopy
VNIR	Very near-infrared

INTRODUCTION GÉNÉRALE *(French version)*

English version down below (p. 21).

Depuis la découverte du phénomène de diffusion Raman exaltée de surface (SERS, comme *surface-enhanced Raman scattering*) en 1974 par M. Fleischmann et coll. [1], la technique correspondante a été considérablement développée, à la fois comme spectroscopie pour l'analyse de biomolécules et comme stratégie de détection de cellules et de tissus pour le diagnostic. Par exemple, le SERS a été utilisé pour détecter des médicaments, des agents pathogènes, des cellules cancéreuses ou pour l'imagerie tumorale *in vivo* [2–7]. Actuellement, le SERS bioanalytique est devenu une technique essentielle à la compréhension des processus biologiques et au diagnostic précoce des maladies. En effet, le SERS bioanalytique présente de nombreux avantages par rapport aux autres méthodes optiques sensibles: (i) composé de dizaines de bandes de vibration étroites, le spectre SERS peut être utilisé comme un code-barres pour identifier les molécules; (ii) la sensibilité de la détection SERS est extrêmement élevée, comparable à celle de la fluorescence et compatible avec la spectroscopie de molécule unique; (iii) le signal SERS est généralement plus résistant au photoblanchiment et à la photodégradation que la fluorescence [8, 9]. Comparé aux larges bandes de fluorescence, le signal SERS de type code-barres [10] permet une détection multiplexée plus pertinente avec une seule longueur d'onde d'excitation. Pour les applications biologiques, la diversité des substrats SERS en termes de taille, forme et surface permet d'utiliser la lumière dans la région spectrale du rouge-proche infrarouge, de 600 à 900 nm (une partie de la « fenêtre optique tissulaire » [11–13]). Dans cette plage spectrale, les avantages sont liés à une absorption/autofluorescence limitée des échantillons biologiques et à la disponibilité des lasers et des détecteurs [11, 12]. Cependant, des améliorations de la sensibilité et de la fiabilité de la détection SERS doivent être apportées avant que le SERS puisse être appliqué au diagnostic clinique pratique.

L'amélioration de la détection SERS implique l'optimisation des substrats SERS qui jouent un rôle clé. Par conséquent, au cours des 40 dernières années, de nombreux efforts ont été consacrés à la préparation de divers types de nanoparticules et nanostructures métalliques [14–23]. La caractéristique commune de ces substrats métalliques est leur forte interaction avec

la lumière via des oscillations collectives d'électrons de surface appelées plasmons [9]. L'effet SERS exige que la bande d'absorption du substrat liée aux résonances plasmoniques (LSPR, comme *localized surface plasmon resonance*) s'adapte à la longueur d'onde du laser utilisé pour l'excitation. Ainsi, l'obtention de l'effet SERS avec une longueur d'onde laser souhaitée, notamment dans la zone du proche infrarouge utile en bioanalyse, nécessite une conception rationnelle des nanostructures en contrôlant leur taille, leur forme, leur matériau et leur état de surface. En effet, l'effet SERS est particulièrement fort pour les molécules situées dans des zones dites "points chauds" (« hot spots » en anglais), qui sont des zones étroites en jonction entre deux surfaces plasmoniques [5]. Les nanoparticules d'or et d'argent sont les substrats les plus utilisés pour le SERS bioanalytique. En raison de sa biocompatibilité, l'or est utilisé préférentiellement pour les tests *in vivo*, tandis que l'argent sera utilisé principalement pour les tests *in vitro,* en raison de son efficacité [5]. Pour obtenir des performances optimales, différentes formes de nanostructures plasmoniques ont été synthétisées et utilisées en SERS. Parmi celles-ci, on trouve des nanobâtonnets [15, 24, 25], nanocubes [21], nanocavité [26], nanoétoiles/nanofleurs [14, 16, 27–29], et des nanostructures cœur-coquille ou noyau-satellite [30][23]. Les nanostructures coeur-coquille/noyau-satellite et les nanoétoiles/nanofleurs sont particulièrement intéressantes pour obtenir des spectres SERS sans agrégation de particules, car au lieu de générer des points chauds dans les jonctions inter-particules, ils offrent un couplage intra-particule des surfaces plasmoniques, entre les couches adjacentes [18] ou des rayons/pétales adjacents [31], respectivement. Ainsi, les nanostructures stables, protégées contre agrégation représentent la nouvelle génération de substrats SERS la plus prometteuse, car elles fournissent une exaltation Raman beaucoup plus uniforme/reproductible, sans compromettre la sensibilité. Comparées aux nanostructures multi-composants cœur-coquille/cœur-satellite, les nanoétoiles/nanofleurs ont une composition plus simple et sont plus faciles à fabriquer.

L'effet SERS a donné d'excellents résultats pour la détection sensible et spécifique de biomolécules, ce qui a permis de créer un champ de recherche qui croît rapidement, appelé SERS bioanalytique [3, 7, 27]. Cependant, il reste encore beaucoup à faire sur le terrain avant que le SERS puisse être pleinement mis en œuvre dans la pratique pour répondre à des questions biomédicales importantes. La détection de la molécule unique dans des milieux biologiques complexes ou la résolution temporelle de la technique SERS sont suffisants pour étudier les systèmes dynamiques, tels que les cellules vivantes. Pour atteindre ces objectifs, il est

nécessaire d'optimiser non seulement les substrats mais également les protocoles de leur application. En effet, des limitations sérieuses doivent être surmontées compte tenu de la variabilité spectrale et des interférences possibles liées à une adsorption compétitive de plusieurs molécules sur la surface plasmonique du substrat.

Dans le cadre de cette thèse, nous nous sommes proposés pour développer de nouveaux substrats SERS basés sur des nanofleurs d'or (AuNFs). Ces nano-objets en or de forme anisotrope ont été conçus pour fournir leur bande LSPR située dans la région de 600 à 900 nm, sans agrégation. En effet, ces AuNFs sont capables de fournir de multiples effets de pointe à l'extrémité de leurs pétales et "points chauds" dans les jonctions entre celles-ci [31]. Etant donné que les tissus biologiques sont plus transparents à la lumière dans la région du proche IR, la capacité de nos AuNFs à interagir avec la lumière proche IR les rend attractifs en tant que substrats pour la spectroscopie bioanalytique à base de SERS, comme le démontrent cette thèse et ses perspectives supplémentaires, par exemple en imagerie optique.

Ce manuscrit de thèse comprend quatre chapitres. Le premier chapitre présente une brève introduction décrivant les techniques Raman et SERS. Tout d'abord, le principe de ces phénomènes sera expliqué, puis une description des substrats SERS existants, pour des applications en bioanalytique, sera présentée. Le second chapitre décrit dans un premier temps, les différents appareils et les méthodes utilisés pour caractériser les nano-objets synthétisés puis, décrit les protocoles de synthèse et d'habillage de ces objets. Le troisième chapitre décrit notre nouveau protocole (brevet en cours de dépôt, un article publié) de synthèse de nanofleurs d'or. Ce protocole dépasse pratiquement toutes les limites des protocoles publiés précédemment pour les applications bioanalytiques. Le quatrième chapitre porte sur l'habillage des nanofleurs afin d'améliorer leur stabilité et leur biocompatibilité. Ensuite, une discussion générale et les conclusions de cette thèse sont présentées, concernant les avantages du protocole de synthèse de nos nanostructures pour les applications en bioanalytique, leur efficacité SERS ainsi que leurs forces et leurs faiblesses. Enfin, les perspectives de ce projet de thèse sont discutées.

GENERAL INTRODUCTION *(English version)*

Since the discovery of the surface-enhanced Raman scattering (SERS) phenomenon in 1974 by M. Fleischmann et al., [1] the related technique has been developed considerably, both as spectroscopy for analysis of biomolecules and as cell and tissue sensing strategy for diagnostics. For example, SERS has been used to detect drugs, pathogens, cancer cells or *in vivo* tumor imaging [2–7]. Currently, the bioanalytical SERS has become an essential technique in the understanding of biological processes and the early diagnosis of diseases. Indeed, the bioanalytical SERS has many advantages over other sensitive optical methods: (i) the SERS spectrum composed of tens of narrow vibrational bands can be used like a barcode [10] to identify the molecules; (ii) the sensitivity of SERS detection is extremely high, comparable with that of fluorescence, and compatible with the single-molecule spectroscopy; (iii) SERS signal is generally more resistant to photobleaching and photodegradation than fluorescence [8, 9]. Compared to large fluorescence bands, the barcode-like SERS signal allows more relevant multiplexed detection with a single excitation wavelength. For biological applications, the diversity of SERS substrates in terms of size, shape and surface allows, to use the light in the red - near-infrared spectral region 600-900 nm (a part of the "tissue optical window" [11–13]), where the advantages are related to a limited absorption/autofluorescence of the biological samples and to the availability of lasers and detectors [11, 12]. However, improvements in the sensitivity and reliability of the SERS detection should be made before that the SERS can be applied in practical clinic diagnosis.

The improvement of SERS detection involves the optimization of SERS substrates which play a key role. Therefore, over the past 40 years, many efforts have been devoted to the preparation of various types of metal nanoparticles and nanostructures [14–23]. The common feature of those metal substrates is their strong interaction with light via collective oscillation of surface electrons called plasmons [9]. The SERS effect requires that localized surface plasmon resonance (LSPR) band of the substrate fits with the laser excitation wavelength. Thus, the SERS effect at a desired laser wavelength, especially in the near-infrared laser for bioanalysis, requires the rational design of nanostructures by controlling their size, shape, material and surface state. Indeed, the SERS effect is particularly strong for the molecules situated in so-called "hot spots", tight areas in the junction of two plasmonic surfaces [5]. Gold

and silver nanoparticles are the most used substrates for the bioanalytical SERS. Because of its biocompatibility, gold is preferentially used for *in vivo* assays, whereas silver will be used predominantly for *in vitro* assays due to its efficiency. To achieve optimized performance, different forms of plasmonic nanostructures have been synthesized and used in SERS, such as nanorods [15, 24, 25], nanocubes [21], nanohollow [26], nanostars/nanoflowers [14, 16, 27–29], and core-shell [18, 32] or core-satellite nanostructures [30][23]. Core-shell/nucleus-satellite nanostructures and nanostars/nanoflowers are particularly interesting to get SERS without particle aggregation, because instead of generating hot spots in the inter-particle junctions, they offer intra-particle coupling of plasmonic surfaces, between the adjacent shells [18, 33] or tips/petals [31], respectively. Thus, the aggregation-free, colloidally stable nanostructures represent the most promising new generation of SERS substrates, since they provide much more uniform/reproducible enhancement without compromising the sensitivity. Compared to multicomponent core-shell/core-satellite nanostructures, the nanostars/nanoflowers have more simple composition and are easier to fabricate.

SERS effect has produced excellent results for the sensitive and specific detection of biomolecules, resulting in a fast-growing field called bioanalytical SERS [3, 7, 27]. However, there is still much work to be done in the field before SERS can be fully implemented in practice to answer significant biomedical questions. Several challenges remain to be accomplished as is the detection of single-molecule possible in complex biological media or is the time resolution of the SERS sufficient technique to study dynamic systems, such as living cells. To achieve these goals, it is necessary to optimize not only the substrates but also their application protocols. Indeed, the serious limitations have to be overcome in view of spectral variability and possible interferences related to competitive adsorption of several molecules on the plasmonic surface of the substrate.

As part of this thesis, we propose to develop new SERS substrates based on gold nanoflowers (AuNFs). These gold nano-objects of anisotropic form have been designed to provide their LSPR band located in the region between 600 and 900 nm, without aggregation. Indeed, these AuNFs are able to provide multiple lightning rod effects on the endpoint of their petals and "hot spots" in the junctions between them [31]. Since biological tissues are more transparent to the light in the near-IR region, the ability of our AuNFs to interact with near-IR

light makes them attractive as substrates for SERS-based bioanalytical spectroscopy, as demonstrated in this thesis, and in further perspective for optical imaging.

This Ph.D. manuscript consists of four chapters. The first chapter presents a brief introduction to Raman and SERS techniques. First, the phenomena principle is explained and then a description of the existing SERS substrates mainly focused on the bioanalytical applications is presented. The second chapter describes the different instruments and methods used to characterize the synthesized nano-objects and then describes the protocols of synthesis and coating of these objects. The third chapter describes our new protocol (patent in progress, a paper published) for synthesizing gold nanoflowers which surpasses practically all the limits of the protocols published before for bioanalytical applications. The fourth chapter focuses on the surface coating of the nanoflowers to improve their stability and biocompatibility. Then, a general discussion and the conclusions of this Ph.D. thesis work are presented, describing the advantages of the synthesis protocol of our nanostructures for the bioanalytical applications, their SERS efficiency as well as their strengths and weaknesses. Finally, the perspectives of this Ph.D. project are discussed.

CHAPTER I. ANALYSIS OF LITERATURE. Raman and surface-enhanced Raman scattering (SERS) bioanalytical spectroscopy

English version down below.

Ce chapitre est dédié à l'analyse bibliographique. Le début de ce chapitre est consacré au principe de l'effet Raman, à l'instrumentation typique utilisée en spectroscopie Raman et ses avantages et limites. Par la suite, nous abordons le principe de l'effet Raman exalté de surface connu sous le nom SERS (comme surface-enhanced Raman scattering), des particularités de la spectroscopie SERS, puis on décrira les substrats SERS nanoparticulaires, l'état de l'art sur leur synthèse et leur utilisation en bioanalytique.

English version.

This chapter is dedicated to the literature review. The beginning of this chapter is devoted to the principle of the Raman effect, the typical instrumentation used in Raman spectroscopy and its advantages and limitations. Next, we discuss the principle of the surface-enhanced Raman effect known as SERS (as surface-enhanced Raman scattering), the particularities of SERS spectroscopy, then we will describe the nanoparticle SERS substrates, the state of the art on their synthesis and their use in bioanalytics.

1. Raman spectroscopy

1.1. History

The Raman scattering (RS) corresponds to an inelastic scattering of light (Figure 1). This phenomenon was predicted by A. Smekal in 1923, first observed in liquids by Sir C.V. Raman [34] in 1926 (Nobel prize in 1928) and has since been named after him. It has led to Raman spectroscopy, which is an optical spectrometry that highlights molecular vibrations and is thus complementary to infrared (IR) absorption spectrophotometry.

1.2. What is the Raman spectroscopy?

As IR, Raman spectroscopy is an optical molecular spectroscopy technique that relies on the interaction of light with vibrational energies of the molecules composing the studied matter. Since the vibrational energy levels depend directly on the molecular structure and/or conformation, the vibrational spectroscopy techniques allow obtaining information on the composition of the material studied [35]. The information obtained by IR and Raman spectroscopy is often used in a complementary way, since Raman is the result of inelastic scattering of light (Figure 2), whereas IR spectroscopy is based on light absorption [36].

The Raman spectrum is composed of characteristic bands of molecular bond vibrations ("molecular fingerprint") and thus allows to identify an organic substance. In addition, Raman spectroscopy provides additional information on the lower frequency modes and vibrations characteristics of crystal lattices and molecular structures. The intensity of Raman scattering increases as the number of contributing bonds increases. Therefore, qualitative (detection of the presence of a chemical species) and quantitative (comparison of the band intensities) information on the sample can be obtained from the Raman spectra [35].

1.3. Raman scattering process

When the light of a frequency ν_0 irradiates a molecule in a gaseous, liquid or solid medium, some of the photons are scattered, either in an elastic or in an inelastic manner (Figure 1).

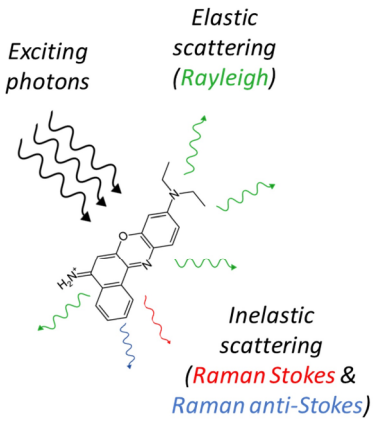

Figure 1. Schematic showing the elastic (Rayleigh) and inelastic (Raman Stokes and anti-Stokes) scattering of the photons on an organic molecule (Nile blue in this study). $n_{Rayleigh}$ and n_{Raman} represent respectively the number of photons corresponding to the elastic and inelastic scattering.

It occurs even with non-resonant exciting radiations, which means that it does not verify the Bohr condition:

$$h\nu_0 = E_1 - E_2, \quad (1)$$

where h is the Planck constant, ν_0 the frequency of the excitation photon emitted by the laser source and E_1 and E_2 the electronic energy levels of the molecule. The elastic scattering which occurs without loss or gain of energy ($h\nu_{scatt} = h\nu_0$, with ν_{scatt} the frequency of the scattered photon) is the dominant scattering-type called Rayleigh scattering. In contrast, the inelastic scattering, involving energy exchanges between photons and molecules, is called Raman scattering and is much less probable (it corresponds to ca. 10^8 times fewer photons than in the case of the Rayleigh scattering [37]). As a result of the exchange, the molecule changes its vibrational state, either to a higher vibrational energy level (+ $h\nu_{vib.}$ $h\nu_{vib}$ represents the energy exchanged with the molecule during the vibrational transition) or to a lower vibrational energy level (- $h\nu_{vib}$). Thus, the difference in energy (frequency) between the photons from the laser and those scattered by the molecules (so-called Raman shift) corresponds to the difference between vibrational levels (frequencies) belonging to the same electronic state of the molecule (Figure 2) [38]. Their energy state (E_v) is defined as:

$$E_v = (v + 1/2)\, h\nu, \quad (2)$$

where v = 0, 1, 2, … represents the vibrational quantic number, h the Planck constant and ν the vibration frequency.

Therefore, there are two types of Raman scattering occurring in parallel: the Raman scattering is called Stokes when the scattered photon has a lower energy than the photon from the laser source ($h\nu_{scatt} = h\nu_0 - h\nu_{vib}$) and it is called anti-Stokes when the scattered photon has a higher energy ($h\nu_{scatt} = h\nu_0 + h\nu_{vib}$). The Raman Stokes and anti-Stokes bands can be observed as shifted to symmetric positions situated on both sides of the excitation frequency. This shift is so-called Raman shift. For each vibration mode, the anti-Stokes Raman scattering has a lower probability of occurring than the associated Stokes Raman scattering. Thus, being of higher probability (and therefore of higher intensity on the resulting Raman spectrum), the Raman Stokes component is used by default in analytics [35]. Usually, only Raman Stokes bands are detected in conventional Raman spectroscopy and their positions are shown as shifts relative to

the excitation light, measured in cm^{-1} which are units of wavenumber ($\bar{\upsilon} = 1/\lambda$, with λ in cm). The shifts are admitted to be positive for the Raman Stokes bands.

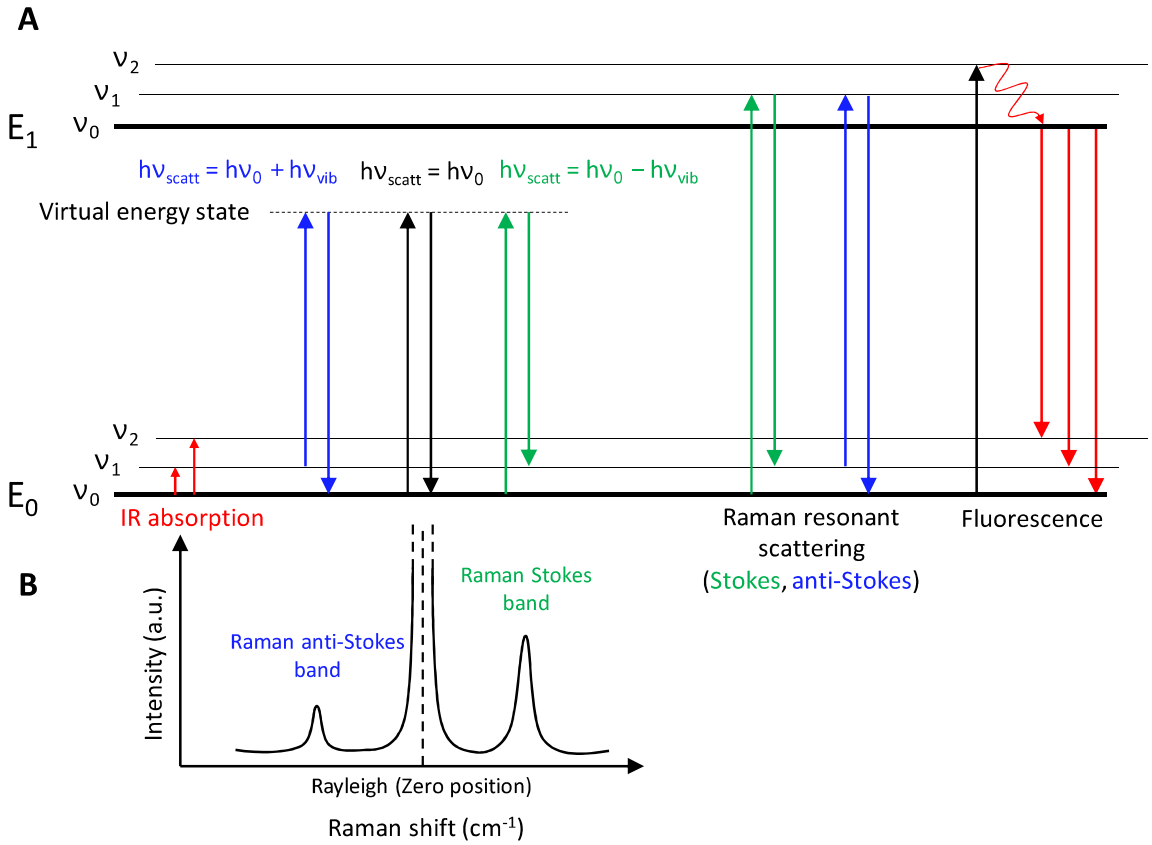

Figure 2. A: Jablonski diagram of the energy levels involved in IR absorption, Raman and Rayleigh scattering, resonant Raman scattering and fluorescence emission where the "E" represent an electron energy levels and the "ν" represent vibrational energy levels. B: Schematic presentation of intensities of the three types of light scattering (from left to right: Raman Stokes, Rayleigh, and Raman anti-Stokes).

By the nature of the light scattering phenomenon, Raman scattering is observable with the excitation wavelengths (laser source) ranging from the UV to the near IR (NIR), including the visible, making the Raman spectroscopy technique very flexible [39].

If the excitation photons have enough energy to induce an electron transition to an excited state (the laser source wavelength is situated within the UV-vis absorption band of the molecule), the resonant Raman (RR) scattering is observed [35] (Figure 2). The resonance with molecular electronic transition provides about a 1000-fold increase in the probability of the phenomenon [38] and thus of the sensitivity of the RR spectroscopy approach. However, if the molecule is fluorescent, the RR effect suffers from the concurrent phenomenon of higher

probability – fluorescence emission [40], which hides Raman bands [38]. This is the reason for the fact that, instead of RR, non-resonant Raman spectroscopy is more frequently applied in analytical purposes. Furthermore, in order to avoid the interference with any fluorescence emission, whatever it is related to the analyte or to its environment, the general tendency is to use low-energy photons (high wavelength lasers emitting in deep red or near-infrared) for exciting Raman signal [35]. The latter is particularly relevant in the case of bioanalytical Raman spectroscopy.

1.4. Complementarity of Raman with IR

Although Raman and IR spectroscopies provide complementary and often interchangeable information, some practical differences determine the most appropriate solution for a given experiment. For non-symmetric molecules, activation of vibrational modes follows the selection rules which allow most of the bands to be detected in both IR and Raman spectra. In contrast, for molecules with an inversion center, the IR and Raman bands are mutually exclusive (the bond is seen either in IR or in Raman spectrum). The rule that generally applies to the band intensity is as follows: functional groups of high dipole moments give intense bands in IR spectra, while non-polar functional groups or structures with a high degree of symmetry give a better response in Raman spectra [41] (see the example of the CO_2 molecule vibrations in Figure 3).

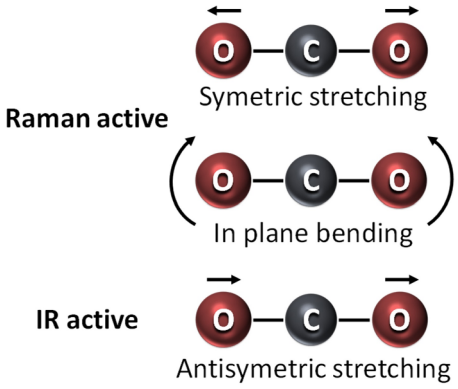

Figure 3. Schematic comparing the activity of vibrational modes in IR absorption and Raman scattering for a carbon dioxide molecule. 3N - 5 = 4 vibrational modes are possible but only 3 are observed due to the degeneration.

The explanation is that, unlike IR spectroscopy which studies changes at the dipole moments, Raman spectroscopy studies changes in the polarizability of molecular bonds. When

a molecule interacts with an electric field ($\vec{E}$) of the incident light (from a laser beam), its electron cloud is distorted and the separation of charges causes the appearance of an induced dipole moment such as

$$\vec{\mu}_{induced} = \alpha\vec{E}, \quad (3)$$

where $\vec{\mu}_{induced}$ is the dipolar moment and α is the polarizability.

The movements of the N atoms of a molecule can be described using 3N normal coordinates. In theory, 3N - 6 and 3N - 5 degrees of movement are observable respectively for non-linear and linear molecules [38]. However, not all of these normal vibration modes can lead to inelastic photon scattering. There are selection rules that make it possible to discriminate between the so-called active modes in Raman. These modes are those which describe the movements of the atoms such as, during these movements, the polarizability of the molecule varies. For example, molecules containing homonuclear bonds (carbon-carbon, sulfur-sulfur or nitrogen-nitrogen) undergo a change in polarizability when they interact with photons. The vibration of these bonds leads to appearance of bands in Raman spectra while they would be invisible or difficult to see in IR spectra.

Raman vibrational signatures are therefore complementary to those observed in IR but have the advantage of not being impacted by the presence of water (no absorption or weak water scattering signal when the sample is illuminated by visible light). Raman spectroscopy is therefore suitable for *in situ* analysis and electrochemical measurements. Due to more strict selection rules than in IR (variation of the polarizability and not of the dipole moment), Raman bands are less numerous and chemical signatures are then more visible. Furthermore, its association with confocal microscopy allows to establish a chemical mapping with a much better lateral resolution than in IR, in the order of 300 nm with traditional apparatus (limitation by diffraction) [38].

1.5. Raman spectrometers

A typical instrumental setup for Raman spectrometry includes the following elements (Figure 4):

1 - a laser source;

2 - an optical system for focusing the laser beam on the sample, collecting the scattered light and sending it to the spectrograph;

3 - a sample holder plate;

4 - a spectrograph, based either on a diffraction grating (dispersive spectrometer) or on an interferometer (Fourier-Transform Raman);

5 - a very sensitive detector controlled by an electronic system for the acquisition and processing of spectral data [35].

In a conventional, macroscopic Raman facility (Figure 4.A), the excitation laser beam is focused on the sample via an objective with a focal length of several millimeters to a couple of centimeters, which allows a relatively large volume/surface of a liquid/solid sample to be irradiated.

In contrast, in a confocal Raman microspectrometer (often called Raman microscope) (Figure 4.B), the analysis is more often done via high magnification microscope objectives (up to x100) with rather short focal length (a few millimeters or less) and large numerical aperture (up to 0.95).

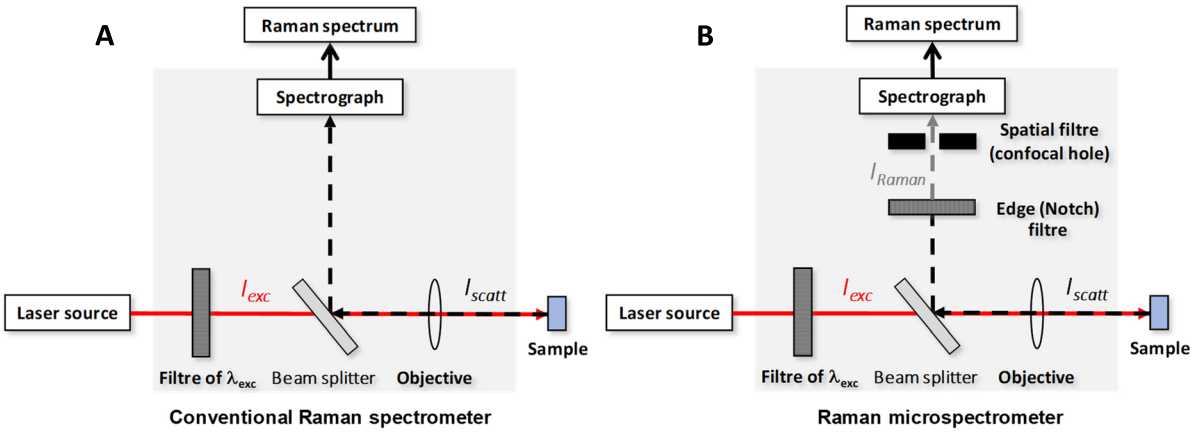

Figure 4. Schematic of typical Raman instrumental setup for macroscopic (A) and microscopic (B) samples analysis.

The diameter of the focusing spot and the spatial resolution are limited by the light diffraction phenomena and therefore depend on the laser wavelength used. The Raman microspectrometers allow a high spatial resolution which can reach down to 0.7 µm in lateral and ca. 2 µm in axial direction when blue light is used. Confocality means that the same objective is used to focus the laser beam on the sample and to collect the back-scattered Raman

signal. Scanning the sample surface or its optical section while recording Raman spectra at each scanned point allows reconstructing specific maps that reflect the spatial distribution of molecular structures, conformations or events. Such an approach is named Raman spectral imaging or Raman chemical imaging [35, 38]. Obviously, the characteristics of optics used to focus the laser beam and collect the scattered light (points 1 and 3 of the set-up) can be adapted to the requirements of each particular application. Furthermore, it is possible to carry out remote Raman analysis using accessories based on optical fibers that may be several meters long.

Depending on the type of the spectral analyzer, diffraction grating or interferometer, a distinction is made between dispersive and Fourier transform (FT) Raman spectrometers, respectively. The FT-Raman instruments are used in the NIR domain (laser source at 1064 nm), where conventional optics is not efficient, namely because of the poor transparency of the glass. The FT-Raman technique has advantages (speed of acquisition, accuracy of the strip position, self-alignment thanks to a pilot laser,…) but also some disadvantages, in particular, the lower spatial resolution for microscopic analysis [35, 38].

Modern Raman instruments are typically equipped with CCD (charge-coupled device) detectors which allow making simultaneous analysis of a large spectral region.
Nowadays, the compact Raman instruments allow working on very small samples (about 1 mm^3 or less) and the acquisition of a spectrum is fast (0.1-10 sec) and can also be done *in situ*. Raman spectroscopy is a non-destructive type of analysis and usually does not require sample preparation. Nevertheless, it is necessary to adjust the laser power, to avoid the sample photodegradation upon measurements.

1.6. Bioanalytical Raman spectroscopy

The Raman vibrational signature of a molecule gives indications on its structure/conformation and on its mode of interaction with its environment. Thus, Raman spectroscopy makes possible to identify/describe molecular structures, conformations, and interactions. Raman spectral imaging allows studying spatial distributions of these molecular parameters over a zone of interest.

Due to that, bioanalytical Raman spectroscopy is used in academic research, industrial R&D and quality control in food, cosmetic and pharmaceutical industry. For instance, Raman spectrometry is particularly well suited to characterize drugs, fatty acids, biological macromolecules (peptides, proteins, nucleic acids) and pharmaceutical polymers [42, 43]. In

the biomedical field, it can be used, for example, to identify the constituents of gallstones [44] and kidney stones [45] or to assist in diagnosis [46], because the Raman spectra of healthy tissues differ from those of pathological tissues, particularly in the case of cancer tissues. It also allows intracorporeal probing of organ tissues by endoscopy using contact probes at optical fibers.

However, all these applications have to deal with the two main limitations of conventional Raman spectroscopy: its low sensitivity and interference with possible fluorescence. In order to overcome these limitations, several solutions exist, namely the surface-enhanced Raman scattering (SERS) technique described below.

2. Surface-enhanced Raman scattering (SERS)

2.1. History

When Fleishmann first observed a Raman signal of an exceptional intensity in 1974, it was not directly associated to a "new" phenomenon, but was rather seen as an increase in the roughness of the silver electrodes after several oxidation and reduction cycles, resulting in an enlargement of the specific surface. Under this hypothesis, the higher density of adsorbed pyridine molecules could explain the enhancement of the Raman signal [1]. It was only 3 years later, in 1977, that two independent groups noted that the concentration of the scattering species taken alone could not explain the about 10^5-fold increase in the signal and both proposed a different mechanism for the observed enhancement. Jeanmaire and Richard Van Duyne [47] proposed an electromagnetic mechanism (EM), while Albrecht and Creighton [48] proposed a chemical enhancement (CE) mechanism involving a charge transfer. Both EM and CE theories are thought complementary to explain the SERS phenomenon.

2.2. Mechanisms of enhancement of the Raman scattering

Since the first observation in 1974 and in parallel with the expansion of SERS technique, numerous experimental and theoretical studies have therefore been carried out to try to understand the phenomena at the origin of the observed enhancement. In particular, the variations of this factor according to the nature of the chemical species, but also the excitation

wavelength, have already led the authors to postulate and highlight the existence of two cooperative phenomena participating in the enhancement process.

First of all, the mechanisms that lead to the enhancement of electromagnetic fields are grouped under the term **“electromagnetic enhancement” (EM)**. It is well accepted that its contribution is dominant over to the total SERS effect, showing enhancements from 4 to 11 orders of magnitude [5].

The second mechanism called **"chemical enhancement" (CE)** would explain the chemical selectivity of the SERS phenomenon, which is not observed on certain species. Although this mechanism contributes less to the total SERS enhancement (~10 to 100 times), it can significantly modify the SERS signal intensity and shape.

Up to now, the basis of the EM mechanism seems relatively well understood and has been successfully applied to guide the experimental design of SERS to achieve a high detection sensitivity, while the CE mechanism is much less clear and requires to be further explored to achieve a better understanding.

Interpretation of SERS experiments by theory remains complex. The convergence cases between the theory and the real measurements are actually special cases in which the experimental parameters of the chosen model systems are well defined (use of nanocrystals with known surface properties and crystallization networks) but cannot be considered as representative of real substrates, generally much more complex and heterogeneous.

2.3. 3D substrates for SERS spectroscopy

The Raman enhancement of the first experiments was not observed on the polished electrode showing a smooth surface. It was only showing up after the electrodes have undergone several redox cycles. However, the size of the surface heterogeneities required after this treatment to get the optimal enhancement of the Raman signal was remaining poorly known. In 1980, while studying an electrode subjected to redox cycles to modify the surface state, Billmann and Otto [49] have highlighted the importance of presence of structures at the nanometric scale.

Instead of rough silver electrodes, other 2D substrates for SERS have been developed, like thin films obtained by electrochemical processes or by chemical vapor deposition (CVD). Nevertheless, the widest range of applications of SERS bioanalytical spectroscopy has been made using 3D substrates like aqueous suspensions (colloids) of nanoparticles made of silver

or gold. The colloidal substrates have been demonstrated as more appropriate for bioanalytical SERS in routine, namely because they are easy and cheap to produce, disposable and of low toxicity. Metal particles (gold and silver but also platinum, copper,...) of different shapes, sizes and degree of aggregation, in solution or deposited, have been developed for SERS [22, 23]. The common feature of those NPs is that they possess so-called localized surface plasmon resonance (LSPR) [50]. Plasmon is defined as a collective oscillation of electrons at a metal surface which can be excited by absorbing radiation of adequate wavelength (Figure 5.A). Nanoparticles that are able to generate a strong LSPR effect are called plasmonic and are usually made of Ag, Au, and Cu because they show strong plasmonic resonance with the light in the visible to the near-infrared region [23]. As a result, an LSPR band is observed in their UV-vis absorption spectra (Figure 8).

The first criterion for the high SERS efficiency is thought to be that the laser excitation wavelength fits to the LSPR absorption band of the NPs used as SERS substrates because it leads to the resonant absorption or scattering of the incident light.

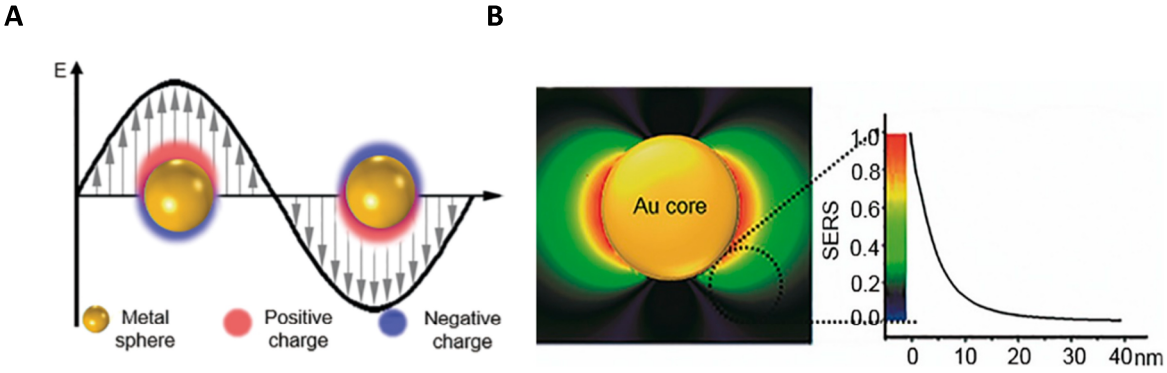

Figure 5. A: Schematic presentation of how the localized surface plasmon is excited by the incident light at the surface plasmon resonance frequency. B: Simulated distribution of plasmon-enhanced electric field around the NP showing the dependence on the distance from the NP surface of the SERS effect [5].

Plasmon excitation induces an amplified electric field (2 to 5 orders of magnitude), which contributes to the enhanced Raman effect. The amplitude of this electric field and thus the SERS efficiency decreases exponentially with the distance from the metal surface (Figure 5.B) [5].

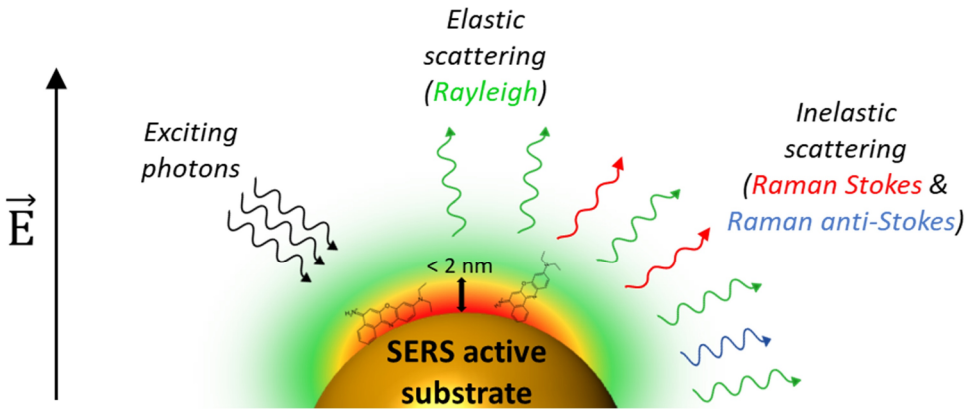

Figure 6. Schematic of the SERS phenomenon as a short-range phenomenon.

Indeed, the electric field is responsible for the EM mechanism of enhancement of the Raman signal: the SERS enhancement factor is approximately proportional to the fourth power of the enhancement of the local electric field [51]. As a result, the contribution to the enhancement of the Raman signal is particularly strong (ca. 80%) for the molecules situated in the close vicinity of the metal surface (< 2 nm) (Figure 6) and becomes much weaker (< 10%) over a distance of about 10 nm. In contrast to the EM mechanism which is considered as being "long-range", the CE mechanism is "short-range", since it requires a direct contact/interaction of the analyte molecule with the plasmonic surface. Therefore, direct contact of the analyte with the plasmonic surface is particularly favorable for the SERS effect, from the EM and the CE both points of view.

In addition to the distance from a given NP surface, the presence of a neighbor NP plays an even stronger role for the SERS effect. Indeed, the efficiency of SERS on isolated NPs is 10^2 to 10^4 lower compared to the same NPs once aggregated [6]. The explanation is that with NP aggregates irradiated by light, a tremendous electric field is created in the very restricted zone situated in the interparticle junction called "hot spots" (Figure **7**.a). Indeed, when two or more NPs are getting close enough to each other, numerous interparticle gaps exhibit extremely high electric field enhancement and produces strong SERS signal. As example, the theoretical calculation of the enhancement factor of an Ag dimer with a 2 nm gap ($\sim 10^9$) is about 10^4 larger than that of a silver sphere ($\sim 10^5$). A single dimer can then produce a SERS signal equal to that of a dozen of thousands of single NPs. Thus, **hot spot formation is the second critical criterion** favorable to high SERS efficiency.

At less than 2 nm of distance between the two AgNPs, the electric field can reach 10^{11} (Figure **7**.b) [5]. Such a high enhancement enables even single-molecule sensitivity for a variety

of resonant and non-resonant molecules. Nevertheless, only a small portion of the whole SERS substrate can be considered as hot spots. It was found that 80% of the total SERS signal, in the case of a spherical AgNP, originated from 35% of its surface, and in the case of an AgNP dimer, from 0.6% of its surface [52, 53].

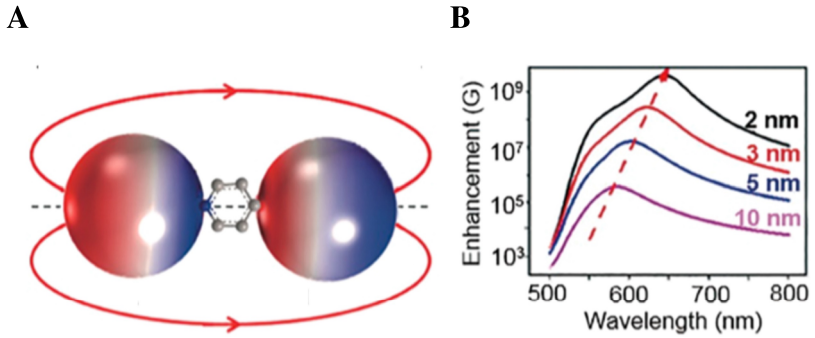

Figure 7. A: "Hot spot" corresponds to a high electromagnetic field created in the junction (gap) between two plasmonic nanoparticles. B: SERS enhancement decrease with the increase of the interparticle distance [5].

For creating hot spots from spherical NPs, typical protocols of SERS analysis include the intentionally induced step of colloid pre-aggregation, usually by increasing the ionic strength via the addition of salts, just before adding analytes. Indeed, added ions-competitors disturb/desorb the stabilizing layer of ions (often citrates) electrostatically adsorbed on the Ag^+ or Au^+ centers present on the surface of the NPs leading to the NP aggregation [54, 55].

The third critical criterion is the modality of the analyte adsorption (affinity and geometry) on the metal surface. In the case of analytes of a very high affinity to the silver or gold, adding of the analyte is enough to pre-aggregate the colloids. However, for the analytes with moderate to low affinity, the pre-aggregation of colloids using the ionic strength increase is desired or even mandatory, since it offers more favorable conditions for the adsorption of those analytes. Indeed, no SERS can be observed without the analyte's adsorption on the substrate metallic surface. Some of the ions, like chlorides, are known to be not only aggregation agents but also to affect the geometry of the analyte adsorption on the metal surface. In this case, one talks about "surface activation" with chlorides [31]. After activation, the reorientation of the chromophore leads to some changes in the SERS spectrum, namely in terms of total intensity increase and/or of selective enhancement of some vibrational bands corresponding to molecular bonds approaching the surface and rising perpendicularly to it [56].

The most commonly used SERS substrates are silver (Ag) and Gold (Au) NPs of a more or less spherical shape, with respective LSPR bands situated around 400-430 [57] and 520-535 nm [58] (Figure 8). Typical diameters of Ag and Au NPs having an LSPR is comprised between 10 to 80 nm, the size below 10 nm does not produce significant LSPR (Figure 8) [59]. The corresponding aqueous colloids have yellow-brownish and ruby red colors, respectively.

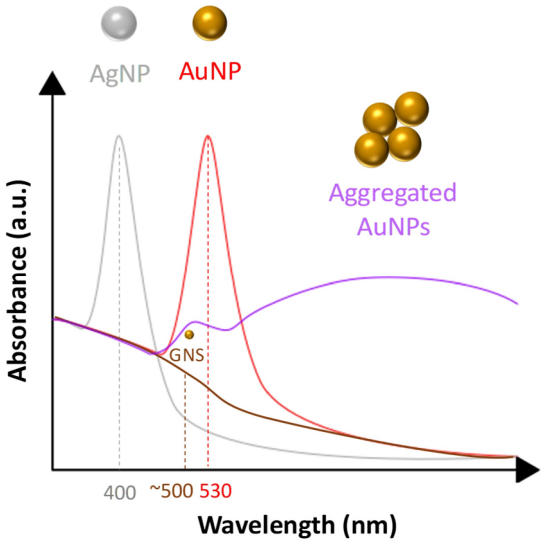

Figure 8. Typical UV-visible absorption of spherical AgNPs (grey curve), spherical AuNPs (red curve), aggregated spherical AuNPs (purple curve) and gold nano-seeds (GNS) around 1 - 2 nm of diameter (brown curve).

Once aggregated, the LSPR band is spread to higher wavelength regions (Figure 8) and colloids turn dark grey (violet first then blue for gold at early aggregation stage) and then become colorless if the NPs are settled down (in ca. 20 - 30 min). The pre-aggregation of the silver and gold colloids has an additional advantage: enlarging the spectral range of the plasmonic absorption. That allows the SERS effect to be generated with laser excitation sources situated in a large wavelength range, from blue to the near-infrared (1064 nm). However, aggregation or pre-aggregation of the colloidal substrates is hard to control and is thought to be the main factor responsible for the poor productivity of the SERS results. For this reason, aggregation-free substrates are under development, as described below.

Among silver and gold, the former is more efficient in SERS but the latter is less chemically reactive and thus is thought to be more appropriate for bioanalytics. For this reason, we further studied gold substrates in this thesis [5].

2.4. Colloids of conventional sphere-like NPs as SERS substrates

The most popular protocol of synthesis of aqueous AuNPs colloid is the citrate-mediated reduction of a chloroauric salt upon boiling [19]. This gives conventional, nearly spherical golden NPs of diameter comprised between 15 and 80 nm (according to TEM) and their colloids are red to violet respectively. These NPs are typically pre-aggregated before their use. As noticed above, the color of such a colloid of AuNPs varies significantly depending on the size of the particles and their degree of aggregation. For instance, adding ions (chloride in particular) to the aqueous colloid of conventional, nearly spherical golden NPs makes it "to turn" from red to blue, then to grey as the size of the aggregates increases with time [54, 55]. The blue color corresponds to a temporary situation when the LSPR band appears shifted to the red region. Such a blue gold colloid would be useful for the bioanalytical purposes, since it would interact with red - deep red lasers, preferred for bioanalytics. However, it is difficult or impossible to fixate this intermediate aggregation state.

The aggregation of AuNPs is not very well controlled. In addition to batch-to-batch poor reproducibility of the SERS intensity, the aggregation leads to an intensity loss over time, due to the substrate sedimentation out of the laser spot. This prevents to study some slow chemical reactions in real-time. Moreover, on a more bioanalytical aspect, the aggregates can't enter the cancer cells and have bad mobility within the body compared with smaller NPs which can induce their accumulations in unexpected areas and lead to bad side effects such as thrombosis.

It is possible to work with colloidally stable, aggregate-free AuNP colloids. Using isolated spherical NPs protected against aggregation has been recently demonstrated by our group [60, 61], using AgNPs coated with PEG shell. The hydrated PEG shell was shown to allow the chromophores of smaller [60] and of bigger [61] size to migrate to the plasmonic surface, in a delay of 0.5 - 1 hour. The advantage of these substrates was their colloidal stability, which offers the possibility to record the SERS spectra over a limit of 30 minutes – we observed the stable SERS signal for up to a week.

Another example of SERS activity of coated NPs is a concept of shell-isolated nanoparticle-enhanced Raman scattering (SHINERS) [62], where gold (Au) or silver (Ag) nanoparticles are surrounded with a shell of silica or alumina. In contrast to PEG, those coatings are much less or non-permeable to chromophores diffusion and require the chromophores being incorporated in the shell during the synthesis. On the other hand, as can be supposed from Figure 5 and Figure 6, when the analyte is located in close vicinity to the AuNP surface (< 10

nm) but not in direct contact with the gold surface, SERS effect can be observed as well, due to the long-range EM effect. As confirmation of this assumption, with the SHINERS which were incubated with the analytes after being coated, the SERS response decreased with an increase of the shell thickness [62]. The SHINERS have been applied to bioanalytical SERS for studying the membrane protein on bacteria and the glycan on the live-cell membrane. More recently, silica-coated NPs were used to study the protein corona. However, in the absence of hot spots, the efficiency of the SERS on those NPs, both PEGylated and silica-coated ones, was several orders of magnitude lower [6]. In addition, in view of their LSPR band position in the green [63, 64], their SERS activity involves the use of the green laser. Thus, in order to overcome these limitations, it is ideal to produce SERS substrates which already have strong hot spots as intrinsic characteristics.

2.5. Gold colloids as aggregation-free SERS substrates

2.5.1. Core-multishell NPs (Nanomatryoshka)

In order to tune the SERS enhancement to the desired red or deep red wavelength region without aggregating NPs, it is possible to couple the plasmons of a metallic core with those of a metallic shell, separated from the core by a dielectric shell (Figure 9). Such a core-multishell NP concept has been called nanomatryoshka (NM) since it resembles to the famous Russian doll [18].

The way to NM has been opened by coating silica NPs with a gold shell reported by S.J. Oldenburg et al. [12]. Then, Ayala-Orozco et al. [18] suggested to generate the gold shell around a silica-coated gold core (Figure 9) and thus to create the AuNM. In the AuNM, the LSPR position can be tuned from visible to near-infrared (NIR) by varying geometric parameters like the gold shell thickness and the inter-shell distance controlled by the thickness of the intermediate dielectric layer (silica or polydopamine [18, 32]). Thus, light absorption and scattering by the NM can be optimized for a wide variety of fields ranging from clinical diagnostics, environmental sensing to basic biomedical research. In addition to the tunable position of the LSPR band, the intra-particle plasmon hybridization allowed by the multilayered gold nanoshells provides another very important advantage: the hot spot space is created in the dielectric layer.

Thus, the organic spacing layer of the NM structure has to be used to encapsulate Raman reporter molecules (aromatic dyes, more or less fluorescent) by their incubation, either before,

during or after the step 2 of the Figure 9. In addition to the SERS effect, the fluorescent dyes confined within the inner dielectric layer of NM can induce until 16-fold enhancement of the fluorescence [18].

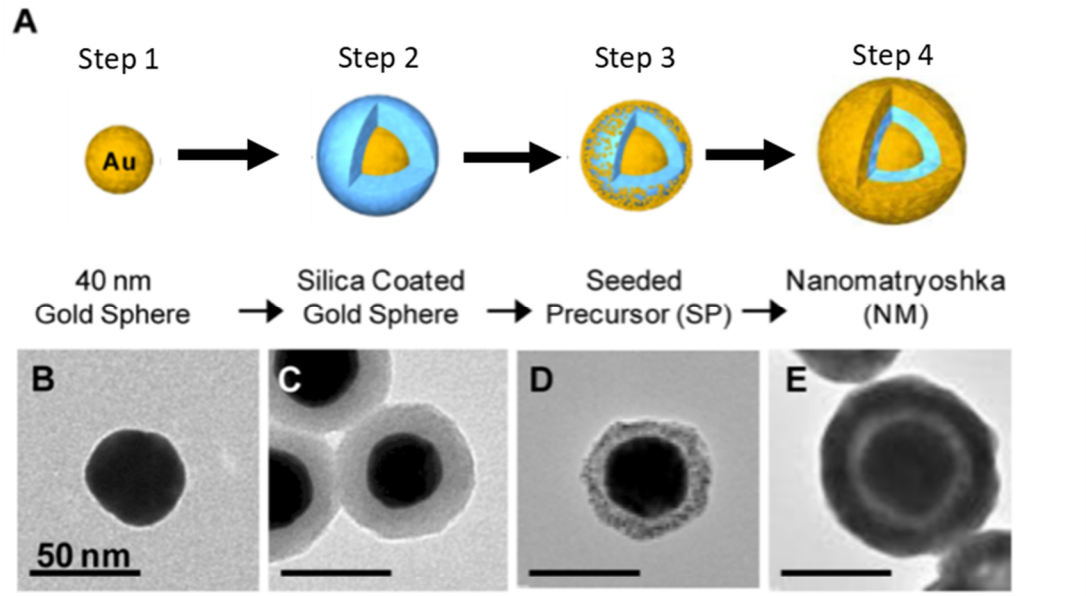

Figure 9. Gold nanomatryoshka (AuNM) synthesis. A: Schematic illustrating the particle structure at each synthesis step. Step 1: An unfunctionalized spherical AuNPs. Step 2: APTES-doped; A silica-coated spherical AuNP. Step 3: Gold nano-seeds covered; A silica-coated gold nanosphere decorated with GNS (ca. 1 - 2 nm) as precursor for the synthesis of the gold layer. Step 4: The gold shell generation; The AuNM is then formed by reduction of the Au^{3+} onto the seeded precursor nanoparticle in the presence of formaldehyde. B – E: Transmission electron microscopic (TEM) pictures corresponding to step 1 to 4 respectively [18].

However, the limitations are also present with the AuNMs. It is a complicated synthesis. Indeed, the layers have to be built one by one and each layer formation may require intermediate steps. For instance, the gold external shell requires adsorption/coalescence of gold nano-seeds (GNSs) on the surface of the silica layer [18]. If the support layer is made of silica, it can be pre-treated with a mercapto/aminosilane precursor which presents quite a high affinity to gold surfaces. The control of the shell synthesis is the main challenge to overcome. In addition, the need for numerous synthetic steps increases the synthesis duration and introduces traces of additional reagents and solvents. Additional purification steps increase the chance to lose a significant part of the initial AuNM. Furthermore, really poor details have been given on the colloidal stability of these newly designed nano-objects. Their colloidal stability in solution is even not mentioned in most of the articles present in literature [18, 32, 65, 66], whereas this

aspect remains of great importance for the medical applications. Indeed, unstable colloids may cause thrombosis, have troubles to reach the targeted cells, get concentrated in unexpected and not aimed areas and eventually become toxic [67]. It is also worth to notice, that the lack of certain details in the experimental parts turns to difficult or impossible the reproduction of the synthesis of these nano-objects [18, 32, 65, 66]. In view of that, we turned our attention to another kind of substrates described below.

2.5.2. Anisotropic NPs

In alternative to the NMs, the SERS enhancement can be tuned to the red or deep red wavelength region without aggregation due to anisotropic gold nanostructures, like nanorods (NRs) [15, 24, 25], nanostars (NSs) [29]/nanoflowers (NFs) [14, 16, 27, 28]/nanourchins (NUs) [68]. The three latter names are often used for very similar objects, the only objective difference may consist in relative dimensions of the petals (tips) which are shorter for the AuNFs than for the AuNSs and is larger for the AuNFs than for the AuNUs.

Particle anisotropy offers features and functions that are difficult to obtain simply by size-tuning of spherical nanoparticles [58]. For example, anisotropic gold nanosystems like gold nanorods (AuNRs), gold nanostars (AuNSs) and gold nanoflowers (AuNFs) are very good candidates to investigate since they are also able to absorb light in the very near-infrared (VNIR) and the NIR within the "tissue optical window" between 600 and 1200 nm [11, 12]. A slight change in particle geometry can produce great changes in the surface plasmon peak position of a metallic nanoparticle, which can hardly be achieved in the spherical nanosystems through a similar change in diameter [29].

Non-aggregated nanorods (AuNRs) allow observing two LSPR bands, one around 535 nm and the other at higher positions, from 600 to 1100 nm (Figure 10). These two bands are respectively assigned to the two plasmon modes: the transversal and longitudinal ones of the nanorods (Figure 11) [25]. These modes correspond respectively to electrons oscillation along the transversal and the longitudinal axis. The longitudinal band is more intense and more red-shifted than what can be reached just by increasing the diameter of spherical gold NPs [58]. The longitudinal band is much more intense compared to the transversal one since the surface charges are more concentrated within a narrower area leading to a higher enhancement of the electromagnetic field on the tips inducing a stronger SERS effect (so-called “lightning rod

effect") [25]. Increasing the ratio of the longitudinal/transversal dimensions of the AuNR increases a red-shift of the long-wavelength LSPR band.

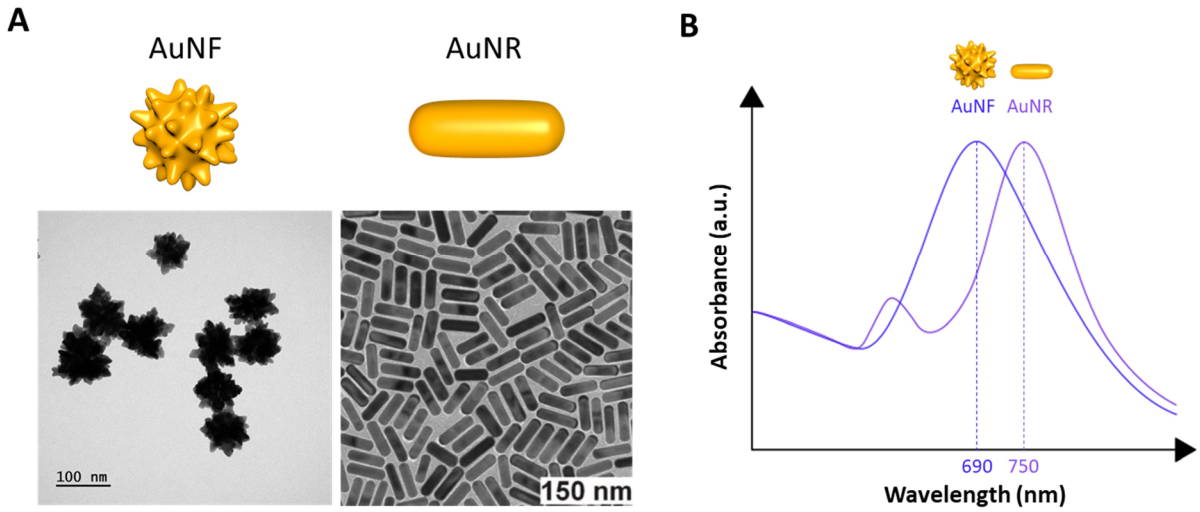

Figure 10. A: Left: 3D scheme of a gold nanoflower and TEM image of AuNFs produced in this work. Right: Left: 3D scheme of a gold nanorod and TEM image of AuNRs from Vigderman et al. [15]. B: Typical UV-visible absorption spectra given by both anisotropic gold NPs.

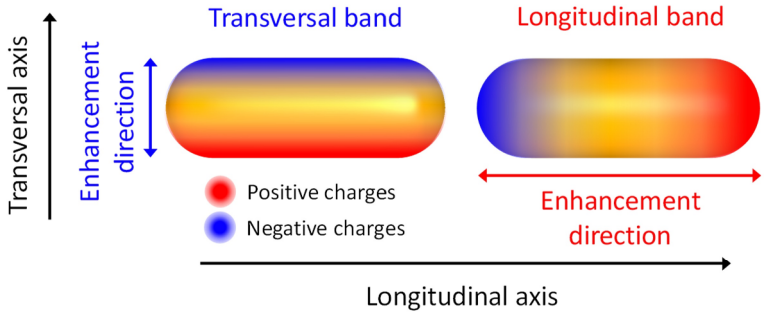

Figure 11. Schematic of typical gold AuNRs on which the two plasmon resonance modes are shown.

An important limitation of the AuNR is that their synthesis imposes the use of toxic surfactants like cetrimonium bromide (CTAB) making their surface hydrophobic [24]. Thus, prior to bioanalytical applications, the CTAB has to be removed.

An alternative anisotropic structure, resembling as an aggregate of thin AuNRs which takes a shape of a nanostar/nanoflower/nanourchin, can be synthesized at some particular conditions. Thereafter, we will call this kind of anisotropic structures: AuNFs. The AuNF

allows combining, in a single nanoparticle, several tips and several junctions of plasmonic surfaces where the plasmon coupling occurs [31, 69] (Figure 12). As a result, the AuNF has a single LSPR band shifted to red or deep-red (Figure 10).

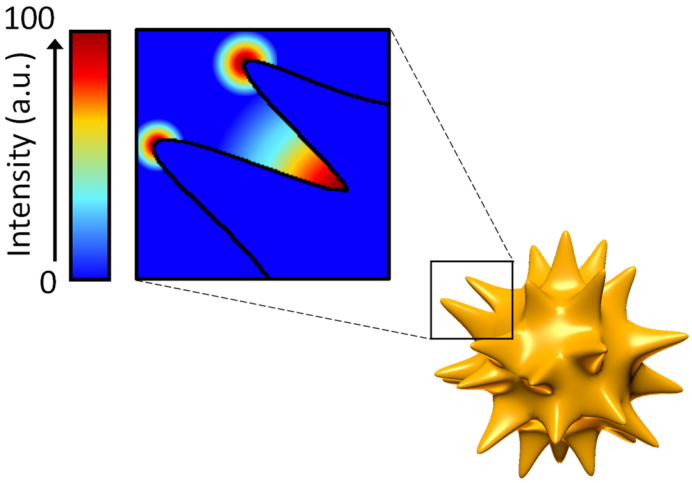

Figure 12. Schematic of a typical AuNS showing the strong increase of the magnetic field at the tip of the petals and the junctions at their base where the Raman is the most enhanced.

Unfortunately, AuNRs and some long-spiked AuNSs may have intrinsical biotoxicity [67], due to their morphology [70] and/or due to the presence of some chemicals (surfactants, metals, solvents) employed in their formulation. Indeed, surfactant-free AuNSs synthesized by H. Yuan et al. [16] had reduced toxicity and permitted an easy surface functionalization. Thus, surfactant-free synthesis protocols have to be developed/preferred for bioanalytical applications.

Other multimeric nanostructures such as linear multimers, core–satellite structures, and superlattice nanostructures have been also reported, but the high-yield synthesis of these nanostructures with a precise conformation remains challenging [30, 71, 72].

Even if the synthesis of these nano-systems is successful, they must be coated to increase their colloidal stability, to make them more biocompatible and so become more stealth to the immune system or more selective for example.

2.6. Coating of the AuNPs to increase their colloidal stability

Indeed, the coating of the NPs has an important role within their colloidal stability. Two main strategies are commonly used to stabilize the colloids (Figure 13).

The first method consists of stabilizing the NPs by their surface charges (Figure 13). In this manner, the NPs are repelling each other by their surface electric charges. A very good colloidal stability can be obtained by this method [19]. The NPs can remain very stable over a long time as long as the charge holders at their surfaces are not degraded, the charges are numerous enough and the colloidal environment does not change [73].
However, even if this way to stabilize the NPs is very effective, it is not suitable in many applications.

In a complex medium, where the pH or the ionic concentration might change, this system will show its limits. For example, in blood, it is more difficult to maintain the charges of the NPs and in addition, these charges can induce their opsonization accelerating their elimination [74]. Furthermore, if the charges are disturbed, it might drive the colloids to an aggregation reducing or even canceling the effectiveness of the NPs to reach their target. On the other hand, aggregates may have potentially negative side effects within the organism.

The second method consists in protecting the NPs from aggregation with the use of a biocompatible polymer such as the poly(ethylene glycol) (PEG) (Figure 13) [75]. PEG neutralizes the NP surface. The stabilizing effect here is from the steric hindrance induced by the polymer chains preventing the nanoparticles to approach each other enough to generate aggregates. Each polymer chain present onto the colloids will behave as a wire in very chaotic and quick movements (a lot quicker than the Brownian motion of the particles) which will make the particles slide on each other every time that one is approaching another [73].

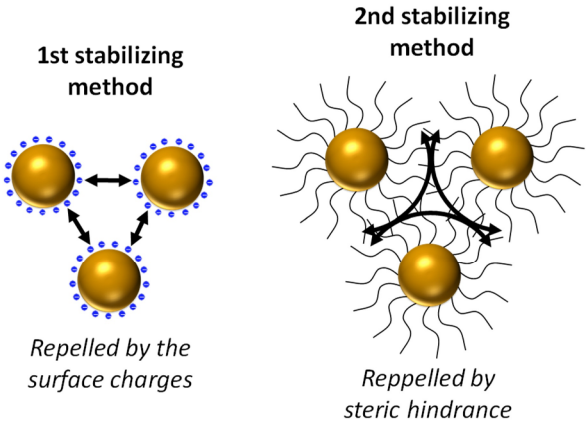

Figure 13. Schematic of gold stabilized nanoparticles; by their surface charges on the left (1st method) and by the steric hindrance of the polymers functionalized at their surface on the right (2nd method).

Two factors of the polymeric shell can influence the stability of the NPs in that case: its density (number of PEG chains per surface unit) and thickness (length of the PEG chains).

According to the grafting density, the polymer molecules can adopt two different conformations (Figure 14). At low grafting density (< 1 chains per nm^2), a "mushroom" conformation is observed, where the PEG chains are folded on themselves. At high grafting density (close to 5 chains per nm^2) [73], a "brush" conformation is then observed, where the PEG molecules are rather stretched [76].

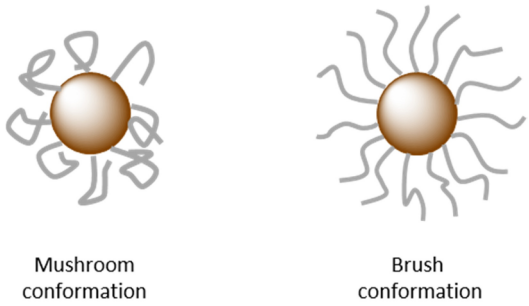

Figure 14. Conformation of PEG molecules grafted on the surface of spherical nanoparticles.

It was proven that the more the chain density per nanometer square was high, the longer the stability of the NPs was in solutions simulating a human physiologic condition. J. Manson et al. [73] compared ability of citrated AuNPs vs PEGylated ones of various chain density to be resuspended in H_2O, PBS, PBS-BSA and DCM over a 24 h period. It was clearly observed that the charged AuNPs were poorly or not resuspendable after centrifugation and drying, while

those coated with high-density PEG shells remained colloidally stable. For example, it was found that at a critical salt concentration of 1 mol/L NaCl, AuNPs functionalized with 16.8 and 25.2 μg/mL of PEG remained stable while citrated AuNPs were completely aggregated.

A second factor plays a role on the colloidal stability of the PEGylated nanoparticles. An investigation driven by V. Cauda et al. [77] on PEGylated mesoporous silica NPs reported that their biodegradation kinetics are slowed down with PEG-shells made of longer PEG chains. After one month, nanoparticles coated with 5000 Da PEG-chains show a higher remaining BET (Brunauer, Emmett and Teller Theory) surface and pore volume compared to the coated silica NPs with 550 Da PEGs, and the quickest drop of surface and pore volume was observed for the unfunctionalized silica NPs in a simulated body fluid (SBF) solution at 37°C.

In addition to being a good stabilizing agent, this polymer increases the biocompatibility of the plasmonic gold NPs.

2.7. Coating of the AuNPs to increase their biocompatibility and stealthiness against the immune system.

For a nanocarrier to be ‘‘stealth’’, that is, almost undetectable by the immune system, the opsonin (plasma protein) adsorption on the NP surface needs to be as low as possible [78]. This is expected for NPs with a charge-free surface, so with a zeta potential close to zero [79]. Stealth NPs can circulate in the blood for a longer time. The prolonged circulation in the blood is expected to delay/reduce NPs accumulation in the main clearance organs (kidney, liver, and spleen) while allowing their accumulation in tumors, namely by the enhanced permeability retention (EPR) effect [80].

For this, the NP hydrodynamic diameter (D_H) needs to be below a critical size which is defined in the literature as between 10 and 200 nm, depending on tumors and studies [81–83]. Nevertheless, the uptake of nanoparticles in cells with a size greater than 100 nm is difficult. NPs not assimilated by the tumor are redirected into the main clearance organs for elimination. NPs of less than 10 nm of diameter are found in the kidney within 15 min after injection and eliminated (renal clearance) [84], while 24 hours after the injection AuNPs of ~10 nm are found in many tissues such as liver, blood, spleen, kidney for the highest concentrations [85] and the AuNPs measuring 50 to 250 nm are most likely found in the liver and the spleen (hepatosplenic clearance) [85, 86].

PEG is known to be an attractive material to reduce opsonization because it is uncharged, hydrophilic, and non-immunogenic [87, 88]. The presence of PEG chains on the NP surface has been shown to increase both their colloidal stability in aqueous suspension at physiologically relevant pH (5 to 8) [89] and the blood half-life *in vivo* [90]. In the study of E. Allard-Vannier et al. [91], results showed that elimination kinetics of citrated SPIONs (C-SPIONs) was very quick because the average concentration of iron-related to nanoparticles in blood was close to zero after 30 min. The half-life time ($t_{1/2}$) for the C-SPIONs in blood was thus estimated to be around 15 ± 9 min. On the contrary, more than 50 % of the PEGylated SPIONs (P-SPIONs) were still circulating in the blood after 60 min to finally totally disappear after 360 min. The $t_{1/2}$ for P-SPIONs was estimated to be 76 ± 6 min. The PEGylation of nanoparticles surface improves their stealthiness, however, for dense inorganic NPs, this improvement is only obtained with polymers of high molecular weight. Indeed, to hinder macrophage-mediated capture of NPs requires the lower limit of PEG size is 2 kDa, while the maximal protection is often obtained with 5 kDa PEG [92].

To summarize, the stealthiness of PEG-coated NPs depends on their D_H and on parameters such as polymer molecular weight, its density, and its conformation on the particle surface [76, 93, 94]. Since both, the biocompatibility and the efficiency of the injectable NPs, depend a lot on their distribution in the body, the targeted nanoparticles are developed to accumulate as much as possible of the injected material in the tumor.

2.8. Functionalization of the AuNPs to expand their targeting capabilities

Once escaped from vessels to tumors, NPs should penetrate into the cancer cells, to increase the accuracy of the diagnostic and/or the efficiency of the therapy. For improved uptake into cancer cells, the PEG shell surface of the NPs has to be decorated with some biologically relevant ligands recognized by receptors overexpressed on cancer cells and/or vessels.

A large variety of such ligands are being studied. Among them, folic acid (FA) [95, 96] is one of the most widely used in anticancer nanomedicine, because of its commercial availability, small size and its easy conjugation [97]. FA is actively consumed by human ovarian and breast cancer cells [98] as well as by some other rapidly dividing cells, due to over-

expression of folate receptors on their plasmic membranes. Kaaki et al. [97] showed that even in breast cancer cells of low folate receptor (FR) expression, the uptake of the FA-decorated PEGylated NPs was increased at least two times. Nevertheless, FA labeling is not very specific, since FR are also present on the surface of some healthy cells which are rapidly dividing. Thus, other more cell-specific targeting agents have been developed, like peptides [99], antibodies or their fragments [100, 101].

Cell-penetrating peptides (CPPs) [99] represent a promising approach. CPPs are able to overcome both extracellular and intracellular barriers and in some cases to enable the release of molecules trapped inside the endosomes/lysosomes into the cytoplasm. Because of their amphiphilic nature, most CPPs at low concentration are able to cross the cell membrane without damaging it. Among the numerous CPPs that are available, Trans-Activator of Transcription (Tat) peptide [102] derived from the HIV-1 Tat protein has been the most intensively studied. The use of Tat facilitated uptake of NPs into immortalized cell lines [103]. Even though there is an enhanced uptake, there are still problems correlated with the endosomal internalization pathway, which is the common mechanism for many nano-objects. Recently, a novel CPP (gH625) derived from a viral protein has been developed and used to enhance the uptake of a variety of cargoes [104, 105]. This unique feature of this gH625 sequence allows the peptide to enter cells allowing the cargo to be more rapidly available in the cytoplasm. In the study of Ben Djemaa et al, [106] the authors investigated the cellular trafficking of SiRNA nanovector functionalized with gH625 peptide in a triple-negative breast cancer model. This study showed that the presence of gH625 allowed to increase the amount of SiRNA found inside the cells and allowed the endosomal escape of SiRNAs.

The targeting properties of the nanoparticles can also be obtained using the specificity of the antibodies. Indeed, conjugation of whole antibodies to nanoparticles is a classical way to specifically target disease cells [107]. MRI nanoprobes decorated with whole HER2-targeting antibodies have been described as being significantly accumulated in HER2-positive cancers [108, 109]. However, the conjugation of whole antibodies to nanoparticles induces several drawbacks that limit the efficiency of cancer targeting, such as poor control of functionalization geometry (which can cause the loss of the biological activity of the antibody [110]) or rapid elimination of nanoparticles via Fc-mediated clearance [100]. Moreover, the conjugation of whole antibodies on the surface of nanoparticles induces an important increase of their surface

charge and/or hydrodynamic diameter [111, 112] and thus decreases their colloidal stability and stealthiness. To circumvent these limitations, one more recently proposed strategy consists in functionalizing the nanoprobes with an antibody fragment such as single-chain fragment variable (scFv) [100, 101]. The scFv have a lower molecular weight (27 vs. 150 kDa) allowing to keep the nanoparticles small, stable and stealth. The ability to engineer them to display desired aminoacids favors the fragment purification/detection and its conjugation to the NPs. Finally, biotechnology protocols allow scFv production to be relatively easy and low cost.

CHAPTER II. MATERIALS AND METHODS

French version (English version down below).

Ce chapitre est consacré à la présentation du matériel et des méthodes utilisés lors de cette thèse de doctorat. La première partie est consacrée à la description des différents instruments et aux méthodes de caractérisation utilisés pour analyser les nano-objets synthétisés. La deuxième partie est consacrée à la description des protocoles de synthèse et de revêtement des AuNFs.

English version.

This chapter is devoted to present the materials and methods used during this Ph.D. thesis. The first part is devoted to the description of the different instruments and the characterization methods used to analyze the synthesized nano-objects. The second part is devoted to the description of the protocols of synthesis and coating of the AuNFs.

1. Characterization techniques and instruments

1.1. Raman spectroscopy

1.1.1. Raman technique

Raman spectroscopy is used to study vibrational, rotational and other low-frequency modes in a system. A monochromatic light beam, usually from a laser source, is focused on the sample by an objective then, a part of the scattered light is collected into a spectrograph which generates the Raman spectrum.

1.1.2. Raman spectrometer

The instrument used was a confocal LabRam Raman microspectrometer (Horiba Jobin-Yvon, France) equipped with an air-cooled CCD detector, a spectrograph (300 nm focal

length, dispersion gratings of 1800 and 300 grooves per mm) and an Olympus BX40 microscope with an automated X-Y-Z scanning range stage (Figure 15).

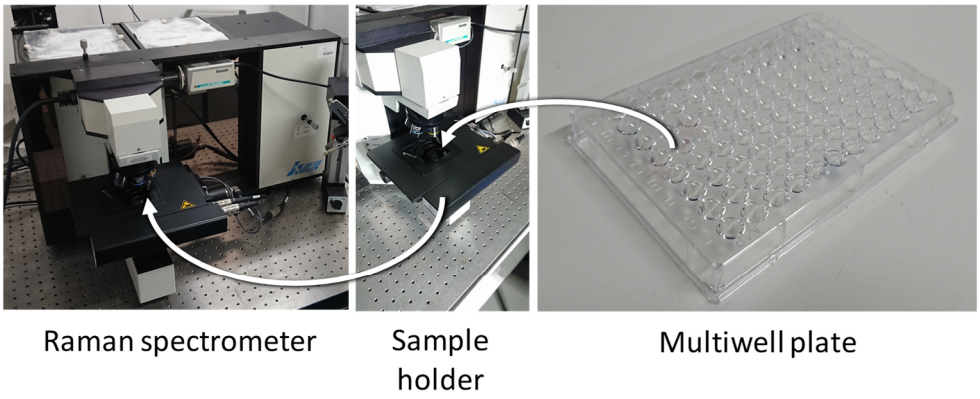

Figure 15. Picture of the Raman spectrometer that was used for our SERS characterizations. The arrows show the sample holder position on the spectrometer and the P96 multiwell plate position on the sample holder.

1.1.3. Preparation & measurements of the SERS samples

Prior to the SERS analysis, the confocal hole was set to 1000 µm, the slit to 100 µm and the grating to 300. No filter was used for the acquisitions. The power of the laser (690 nm, RO691-PLR45, Ondax Inc, Monrovia, CA, USA) at the samples was estimated to be 16 mW. The analyses were performed under a 10x microscope objective (numerical aperture 0.25; MPlan, Olympus, Japan).

Once the previous step done, 200 µL of the suspension ([Au] = 0.4 mmol/L for surfactant-free, PVP and PEG-coated AuNFs. [Au] = 0.2 mmol/L for the Pluronic, alginate, chitosan, and silica-coated AuNFs), incubated with 1 µmol/L of Nile blue, to analyse were injected into a well from a P96 multiwell plate of 200 µL capacity each. By the mean of a semi-reflective mirror which re-direct a part of the laser beam toward a camera and the manual control of a mobile electronic support, the laser beam could be centered and focused at half of the depth of the medium in the well at the most homogeneous point of the suspension. Then the mirror was removed from the laser beam course allowing it to hit the sample at its full power.

By default, the first acquisition was an average of 10 scans performed on 1s of exposure each. If the SERS signal was saturating then, the exposure time was reduced in order to avoid the saturation. Once the right parameters were found, three independent acquisitions at identical conditions were performed on the sample. The SERS spectra presented in this Ph.D. thesis are

averages of these three acquisitions. The spectral data acquisition and treatment were done using a LabSpec software (Horiba SAS, Villeneuve d'Ascq, France).

1.2. UV-visible absorption spectroscopy

1.2.1. UV-visible absorption technique

Ultraviolet-visible absorption spectroscopy is used to measure the absorption of light by a fluid (and solids in some more uncommon cases), within the range of the UV to visible light, to determine the concentration of the specie studied and its interactions with its environment (nowadays the UV-visible absorption spectrometers are even able to go until the VNIR - NIR region and so cover a wavelength range of the light spectrum from 100 up to 1400 nm).
Irradiated within these wavelengths, molecules, ions, complexes, or plasmonic nanoparticles may be excited at different energy levels depending on their configuration, conformation and their interaction with their environments.

A monochromator decomposes the white light coming from the lamp (commonly a xenon lamp nowadays) and selects the wished wavelengths to swipe the wavelength range set before the measurement. Each wavelength goes through the sample and hit the detector behind one after the other. However, some wavelengths hit the detector with a different intensity than the one obtained when they have been through the solvent only. The comparison between the signal of the light transmitted from the solvent only (the blank) with the one from the sample reveals the absorption spectrum of the specie studied within the sample environment.

1.2.2. UV-visible absorption instrument

The spectra were acquired by a ThermoFisher Scientific GENESYS 10 UV-Vis spectrophotometer (Thermo Scientific, France) (Figure 16) with ±1 nm of accuracy, a scanning range from 190 to 1100 nm and from 0.005A to 2A, and a xenon lamp as its light source. The optical system is composed of a split-beam, a grating, and dual detectors.

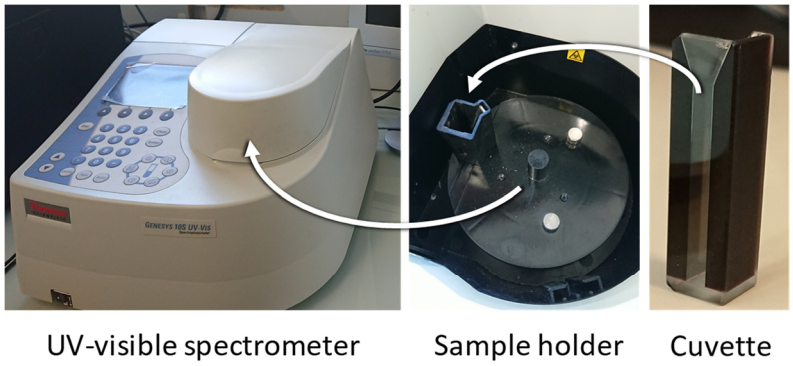

Figure 16. Picture of the UV-visible absorption spectrophotometer that was used to characterize the LSPR band position, intensity and shape of our AuNPs. The arrows show the sample holder position on the spectrometer and the cuvette position in the sample holder.

1.2.3. Preparation & measurements of the UV-visible samples

Prior to the measurements, the spectrometer parameters were set as follow: the scanning range was first set from 400 to 1000 nm with a scanning step of 1 nm. Then, the blank was done with 1 mL of DIW (the solvent) in a quartz cuvette.

The preparation of the samples was carried out as follow: once the spectrometer set and ready, 400 µL of the aqueous suspension ([Au] = 0.8 mmol/L for every samples to remain between 0.5 and 1 A and comparable) were poured into the same 1 mL quartz cuvette used for the acquisition of the blank.

The same cuvette was used for all samples. Prior any measurement the transparency of the cuvette was checked and cleaned with a soaked tissue of ethanol if required and between two sets of measurements or if the inner face of the walls of the cuvette were slightly colored, because of traces of previously analysed colloids, the cuvette was left few minutes in a concentrated (5 mol/L) aqua regia solution (1 volume of nitric acid for 3 volumes of chloridric acid) then abundantly rinsed with distilled water and finally with DIW.

1.3. Dynamic light scattering (DLS) spectroscopy

1.3.1. DLS technique

Dynamic light scattering spectroscopy is used to measure the hydrodynamic size (D_H) (it is the diameter of the particle with its solvation layer included) of particles directly in their

environment. This technique measures the light scattering on particles in Brownian motion and then calculate the hydrodynamic size (D_H) distribution of the particles.

The DLS technique allows also to measure the zeta potential of the particles by the Doppler laser electrophoresis methods. An electric field is applied on a suspension of particles which then move at different speeds depending on their zeta potential then, their speed is measured by an interferometric system called phase analysis light scattering (M3-PAL). Finally, the zeta potential is determined from the electrophoretic mobility of the particles studied.

1.3.2. DLS instrument

The NP sizes and zeta potential were measured with a Zetasizer Nano ZS from Malvern Panalytical (Malvern HPPS, Malvern Instruments, UK) (Figure 17). A laser He-Ne (4 mW, 633 nm, scatter angle 173°) is used as its light source and it can set the temperature of the sample from 0°C to 90°C. It is able to measure NPs from 0.3 nm to 10.0 µm of diameter in suspension of 0.1 mg/mL.

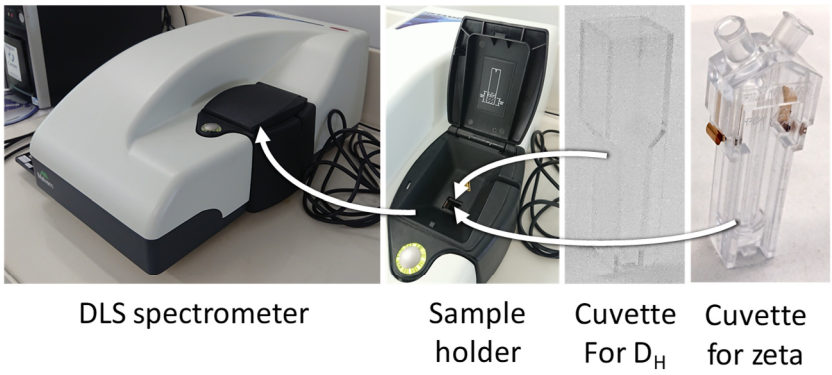

Figure 17. Picture of the DLS spectrometer that was used for our AuNFs hydrodynamic size and zeta potential characterizations. The arrows show the sample holder position on the spectrometer and the cuvette position in the sample holder.

1.3.3. Preparation & measurements of the DLS samples

Prior to the size measurements, the spectrometer parameters were set as follow: the size measurements were done following the model of Smoluchowski, with water as the dispersant and gold as the material. The zeta potential measurements were done by the mean of a DTS1070

capillary cuvette (Figure 17), full of the sample, having two metal foils connected to the electrodes of the spectrometer.

In both cases, before each measurement, the temperature of the sample was set to 25°C for 2 min (except for the AuNFs synthesized at 0°C, for which the temperature was set to 1°C for 5 min).

The preparation of most of the sample was carried out as follow: to measure the average D_H (z-average), 1 mL of the aqueous suspension ([Au] = 0.08 mmol/L) was poured into a 1 mL cuvette. Before each measurement, the transparency of the cuvette walls was checked, and cleaned with ethanol if required, in the same manner as for the cuvette used for the UV-visible absorption measurements; to measure the average D_H of the particles, the DTS1070 cuvette was filled by the suspension until both of the metal foil of the cuvette are fully immersed into the sample.

For our zeta potential measurements, we compared only samples from similar batches in order to avoid to change the colloidal stability of our samples by changing the ionic force of our suspensions.

Finally, each DLS measurement (size or zeta) was done in triplicate.

1.4. Transmission electron microscopy (TEM)

1.4.1. TEM technique

Transmission electron microscopy is used to observe nanostructures which cannot be observed with a classic optical microscope based on visible light which has wavelengths longer than the size of the nanostructures observed. This technique uses an electron beam (commonly tired apart from a tungsten wire) between the source and an anode and focused on the sample (commonly on a copper grid of ca. 2 to 3 mm of diameter) by the mean of an objective made of magnetic or electrostatic lenses. The electron beam interacts then with the sample to pass through but due to the spatial variations or the chemical composition of the nanostructure analyzed, its electron density varies. The intensity of the transmitted beam hit then the detector behind the grid with some variations according to the area of the sample it had been through. Finally, the detector generates a white and black picture, contrasted according to the variations of the electron beam intensity received.

1.4.2. TEM instrument

The pictures were acquired using a JEOL JEM-1400 Plus (10 - 120k) (JEOL Inc., Peabody, MA, USA) (Figure 18) with a camera GATAN OneView and Digitial Micrograph 3.22 as software. The electron source was from a lanthanum hexaboride cristal (LaB_6). The grids used were formvar/carbon nickel grids of 3.05 mm of diameter.

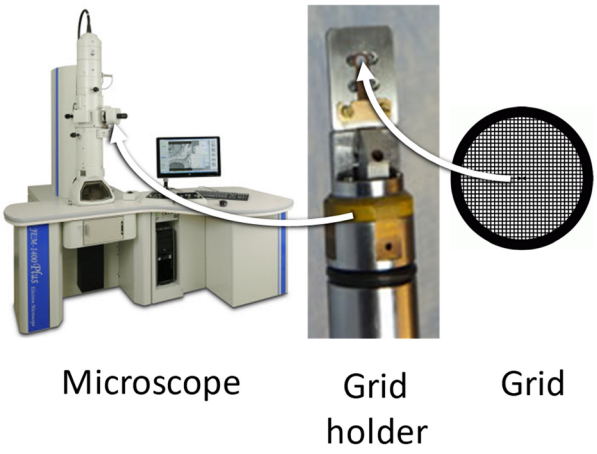

Figure 18. Picture of the Transmission electron microscope that was used to observe the 2D morphology of our nano-objects. The arrows show the sample holder position on the microscope and the grid position on the sample holder. The picture of the microscope and the grid holder are from www.jeolusa.com and the picture of the grid is from www.2spi.com.

1.4.3. Preparation & measurements of the TEM samples

1 mL of the AuNF suspension was transferred into a 2 mL eppendorf ([Au] = 0.4 mmol/L for surfactant-free, PVP and PEG-coated AuNFs. [Au] = 0.2 mmol/L for the Pluronic, alginate, chitosan and silica-coated AuNFs). The grid was immersed into the suspension inside the Eppendorf for about 5 min then dried in the air on a filter paper for about 15 min. Once the grids dried, they were carefully inserted into the microscope after a short vacuum step. The acquisitions were then performed under an electron beam at 120 kV.

Image J software was used to measure the size distribution of the AuNFs.

1 - Measurement of the anisotropic NPs sizes

Two perpendicular dimensions were measured on each of the 60 NPs chosen.

2 - Measurement of the silica shell thicknesses

Four independent areas of the silica shell were measured on each of the 10 NPs chosen.

For each batch, the weighted average size was determined as the center of mass of the corresponding size distribution, calculated according to the equation: $D = \frac{\sum D_i N_i}{\sum N_i}$ where D_i is the AuNF diameter range (for example, for a range of 10 nm per NP size group, 0-10 nm is presented as 5 nm, 10-20 nm is presented as 15 nm and so on), and N_i is the number of AuNFs in the dimension range D_i.

2. Protocols of synthesis

Chemicals

Gold (III) chloride trihydrate ($HAuCl_4 \cdot 3H_2O$) (≥ 99.9%), trisodium citrate dihydrate ($HOC(COONa)(CH_2COONa)_2 \cdot 2H_2O$) (≥ 99.0%), sodium hydroxide (NaOH) (≥ 97.0 %), chitosan (M_w = 110,000 - 150,000), sodium alginate and (3-Mercaptopropyl)triethoxysilane (MPTES) (≥ 80%) were purchased from Sigma-Aldrich (Saint Quentin Fallavier, France). Hydroxylamine hydrochloride ($NH_2OH \cdot HCl$) (≥ 99.0%) was purchased from VWR (Fontenay-sous-Bois). Polyvinylpyrrolidone (PVP, M_w = 7.0 – 11.0 kDa) and Pluronic F68 (M_w = 8.4 kDa) and F127 (M_w = 12.6 kDa) were purchased from BASF (Levallois-Perret, France). Poly(ethylene glycol) methyl ether thiol (CH_3O-PEG-SH) was purchased from Rapp Polymer (Tübingen, Germany). Nile blue A, pure certified, was purchased from Acros Organics, (New Jersey, USA). Deionized water (DIW) was taken from a Merck Millipore Milli-Q water purifier and showed a resistance of 18.2 MΩ at 20°C.

Within the next sections, all the syntheses were done in vials wrapped in parafilm and in an aluminum foil to optimize the gold petal stability and limit the NB fluorophore bleaching during its adsorption onto the AuNFs.

2.1. Preparation of the surfactant-free AuNFs

20 mL of DIW were poured into the cleaned 50 mL glass Erlenmeyer which already contains the TEFLON magnetic rod. 300 µL of the 0.1 mol/L NH_2OH solution, 1 mL of the 0.1 mol/L trisodium citrate (Na_3Cit) solution and 1 mL of the 0.1 mol/L NaOH solution were also consecutively poured into the flask under medium stirring (400 rpm). The Erlenmeyer was immersed in the water bath for (a) 15 min or (b) 5 min. Then, the stirring strength was increased until a vortex is formed (1500 rpm) and 1 mL of the 0.01 mol/L $HAuCl_4$ solution was injected

as fast as possible into the mixture vigorously stirred. The suspension turned deep blue immediately. The stirring was stopped after 5 s to avoid accelerating the degradation of the AuNF petals (discuss later in the next chapter).

Prior to the synthesis of the AuNFs the temperature of the medium was set to the desired value:

a - Synthesis at 25°C: The water bath has to be heated at 25°C under magnetic stirring (400 rpm). All the solutions were at room temperature (20°C) before their use except the gold precursor solution which was immersed in the same water bath (25°C) as the Erlenmeyer flask where the synthesis took place later.

b - Synthesis at 0°C: All the solutions used were placed in the cooled room at 4°C for at least one night before their use. To reach 0°C, the 50 mL Erlenmeyer flask was placed into an ice bath with the vial containing the $HAuCl_4$ solution and a 250 mL Erlenmeyer flask full of DIW capped under parafilm between each use.

2.2. Preparation of the polymer-coated AuNFs

Coating of the AuNFs with PVP

Within 5 s after the preparation of the gold nanoflowers (see II.2.1), 1 mL of a 12.65 mg/mL PVP solution was poured into the AuNF suspension ([Au] = 0.4 mmol/L) still in the 50 mL Erlenmeyer. Then, the suspension was left under magnetic stirring at 300 rpm for 36 hours.

For extensive coating or functionalization, the PVP-coated AuNFs can be washed

The PVP-coated AuNFs were then centrifuged at 3000 rcf for 30 min at 20°C. After, centrifugation the deposit at the bottom of the flask was dark blue while the supernatant was as transparent as water. The PVP-coated AuNFs were then, dispersed back into the same volume as the freshly synthesized surfactant-free AuNFs (23 mL of final volume).

The previously described washing process was repeated once more then the AuNF suspension was finally stored at 4°C in darkness in a capped vial wrapped in parafilm and an aluminum foil.

Coating of the AuNFs with PEG

Within 5 s after the preparation of the gold nanoflowers (see II.2.1), 4 mL of the AuNF suspension ([Au] = 0.4 mmol/L) were poured into a 30 mL vial then 70 µL of a 25 mg/mL PEG solution were added under stirring (400 rpm). Then, the suspension was left under magnetic stirring for 24 hours.

Adsorption of the NB onto the PVP-coated and PEGylated AuNFs

The NPs always had been incubated in presence of NB (1 µmol/L of NB in the final volume) for 24 hours under magnetic stirring (400 rpm). Different volumes of the AuNF suspension ([Au] = 0.4 mmol/L) were used according to the experiment but we kept the same molar ratio between the NB and the gold concentration to remain comparable ([Au] = 0.4 mmol/L for [NB] = 1 µmol/L both concentrations in the final volume).

Coating of the AuNFs with Pluronics F68 and F127, alginates, and chitosan

Within this section, the protocol describes the coating of the AuNFs with Pluronics F68 and F127, alginates, and chitosan, all grouped under the term of polymer, at a Polymer/Au w/w ratio of 10 and 0.01. The quantities in brackets correspond to the ratio of 0.01.

3.38 mL (3.38 µL) of the 1 mg/mL polymer aqueous solution was mixed with 620 µL (4 mL) of DIW in a 30 mL vial. 10 s after the synthesis of the gold nanoflowers (see II.2.1), 4 mL of the AuNF suspension ([Au] = 0.4 mmol/L) were poured into the vial containing the polymer solution under medium magnetic stirring (400 rpm) and left for 1 hour. The stirring was stopped and the suspension was then left incubating at room temperature in the lab for 24 hours.

Lowering of the pH of the chitosan-coated AuNF suspension from 7 to 5

30 mL of a 0.2 mmol/L of HNO_3 were poured into 2 mL of the chitosan-coated AuNF suspension ([Au] = 0.2 mmol/L) in a conical centrifuge tube. The suspension is then shaked for 15 s and sonicated for 1 hour.

Adsorption of the Nile blue (NB) onto the Pluronics F68 and F127, alginates, and chitosan-coated AuNFs

2 mL of the suspension of the coated AuNFs ([Au] = 0.2 mmol/L) were poured into a 15 mL centrifuge tube already containing 10 µL of a 200 µmol/L NB aqueous solution. The tube was then shaken for 20 s and left 24 hours incubating at 4°C in darkness in the cooling room.

2.3. Preparation of silica-coated AuNFs

Encapsulation of the AuNFs in a silica shell directly onto the surfactant-free and of the washed PVP-coated AuNFs (incubated or not in 1 µmol/L of NB).

Within 30 s after the preparation of the surfactant-free AuNFs or after the washing process (previously described in the section II.2.2) of the PVP-coated AuNFs, according to the kind of NP to coat in the silica matrix, 4 mL of the AuNF suspension ([Au] = 0.4 mmol/L) were poured into the pre-hydrolyzed 4 mL MPTES aqueous solution. Different concentrations of MPTES were tried corresponding to the R3 ratio defined as MPTES/Au molar ratio (see Table I for more details of the concentrations of the MPTES solutions). Then, the suspension was left under magnetic stirring (400 rpm) for 24 hours.

Only the syntheses at the R3 ratios of 1 and 10 was tried on the PVP-coated AuNFs.

Table I. Table showing the different concentrations of the MPTES solutions used to coat the surfactant-free and the PVP-coated AuNFs with their corresponding R3 defined as the MPTES/Au molar ratio.

R3	10	1	0.1	0.02
[MPTES] (µmol/L)	4300	430	43	21.5

Preparation of the silica layer in presence of Nile blue onto the surfactant-free AuNFs

30 s after the preparation of the gold nanoflowers, 4 mL of the suspension ([Au] = 0.4 mmol/L) were poured into an aqueous mixture of 4 mL of pre-hydrolyzed 0.43 mmol/L MPTES (corresponding to an R3 ratio of 1) and 1 µmol/L of NB. Then, the suspension was left under magnetic stirring for 12 hours.

Washing process and storage of the silica-coated AuNFs

All batches of silica-coated gold nanoflowers were centrifuged at 5000 rcf for 15 min at 20°C. After centrifugation, the deposit observed at the bottom of the flask was dark blue while the supernatant was as transparent as water. The coated gold nanoflowers were then, dispersed back into 4 mL of DIW and sonicated for 15 min at 20°C to ensure good dispersion of the particles.

The suspensions were finally stored at 4°C in darkness in a capped vial wrapped in parafilm and an aluminum foil.

CHAPTER III. RESULTS. Synthesis of novel SERS substrates in a form of gold nanoflowers (AuNFs)

Introduction *(French version)*

English version down below (p. 63).

Au vu de l'intérêt considérable que suscitent les AuNFs en tant que substrats SERS, de nombreux articles ont été publiés sur les divers protocoles de leur synthèse. En effet, les termes « nanoflower » et « nanostar » s'appliquent généralement à des objets identiques ou très similaires, ayant des pointes plus ou moins allongées en forme de rayons (étoiles) ou de pétales (fleurs) et il n'est donc pas évident de distinguer les protocoles correspondants.

En principe, les protocoles les plus cités traitent d'au moins deux étapes : (i) la formation de graines-amorces (sphères allant jusqu'à 5 nm de diamètre) et (ii) la croissance anisotrope de pétales/rayons. De nombreux ingrédients ont été décrits dans la littérature pour favoriser la première ou la deuxième étape [14, 16, 17, 27, 28, 113, 114]. En conséquence, la liste des produits chimiques (métaux autres que l'or, solvants organiques et/ou tensioactifs) est longue et les colloïdes résultants doivent subir des étapes de purification après la synthèse, sinon ils présenteraient une certaine toxicité. De plus, le contrôle de la réaction implique souvent une régulation du pH [17] et/ou un chauffage de la solution réactionnelle à la température d'ébullition de l'eau [115]. Certains protocoles de chimie plus simples peuvent être trouvés dans la littérature, mais ils demandent du temps et ne permettent pas de contrôler les paramètres des AuNFs : la taille est généralement importante (plus d'une centaine de nanomètres) et très hétérogène, et la concentration en nano-objets est faible. On peut en conclure qu'il n'y a pas de protocole « gold standard » disponible pour la synthèse des AuNFs. Malgré ces difficultés, commencer par ce type de protocoles pris dans la littérature a été la première stratégie tentée au laboratoire.

L'objectif était de générer des AuNFs avec la bande LSPR située autour de 690 nm, afin de s'adapter à la source laser correspondante. Il a donc été essayé tout d'abord de reproduire les protocoles publiés précédemment qui s'approchaient le plus des critères suivants :

a) faire la réaction en milieu aqueux ;

b) ne pas utiliser des ingrédients toxiques (hydrazine, CTAB, etc…) ;

c) pouvoir transposer le protocole facilement à des laboratoires non spécialistes en chimie (équipement limité, expérience en synthèse minime).

Étonnamment, aucun des protocoles que nous avons testés n'a donné de résultat escompté, du moins proches de ce que prétendaient les auteurs. Les colloïdes résultants étaient de couleur soit grise, soit rouge, au lieu de bleue. Certains d'entre eux étaient de couleur bleue, mais la coloration était très légère (absorbance faible), et devenait rapidement incolore ou grise, à cause de l'agrégation. Certains des protocoles suggéraient de concentrer les NPs par centrifugation, mais ces dernières s'agrégeaient lors de cette opération [16].

Compte tenu de la situation décrite ci-dessus, nous avons décidé de rechercher notre propre protocole de synthèse de nanofleurs d'or. En conséquence, un nouveau protocole a été développé en laboratoire et a fait l'objet de l'étude décrite dans l'article présenté ci-dessous.

Introduction *(English version)*

In view of tremendous interest to the AuNFs as SERS substrates, numerous papers have been published on the various protocols of their synthesis. Indeed, the terms "nanoflower" and "nanostar" are usually applied to the same or very similar objects, having more or less elongated spike-like (star) or petal-like (flower) tips and thus, it is not obvious to distinguish the corresponding protocols.

In principle, the most cited protocols deal with at least two steps: (i) formation of seeds (spheres of up to 5 nm of diameter) and (ii) anisotropic growth of the petals/tips. Numerous ingredients have been described in the literature to favor either the 1st or the 2nd step [14, 16, 17, 27, 28, 113, 114]. As a result, the list of chemicals (metals other than gold, organic solvents and/or surfactants) is long and the resulting colloids have to undergo the steps of purification after the synthesis, otherwise they would show certain toxicity. In addition, the reaction control often involves pH regulation [17] and or heating the reaction solution to the water boiling temperature [115]. Some protocols of more simple chemistry are findable in the literature, but they are long and do not allow to control the AuNF parameters: the size is large (more than a hundred of nanometers) and very heterogeneous, and the concentration of nano-objects is low. One can conclude that there is no "gold standard" protocol available for the synthesis of AuNFs. In spite of those difficulties, starting with this type of protocols taken from literature was the first strategy tried in the laboratory.

The aim was to generate AuNFs with the LSPR band situated around 690 nm, to fit with the corresponding laser source. Thus, it had been tried to reproduce the previously published protocols, chosen according to the following selection criteria:

a) making reactions in aqueous medium;

b) non-using toxic/dangerous ingredients (hydrazine, CTAB, etc…);

c) easy transposition to non-chemist labs (minimum equipment, weak experience in synthesis).

Surprisingly, none of the protocols we tested provided an expected result, at least a result close to what was claimed by the authors. The resulted colloids were either grey or red instead of blue. Some of them were of blue colour, but very light (low absorbance) and turned rapidly colourless or grey. Some of the protocols suggested to concentrate the NPs by centrifugation, but they aggregate upon this operation [16].

In view of the situation depicted above, we decided to look for our own AuNF synthesis protocol. As a result, a novel protocol was developed in the lab and made a subject of the study which is described in the paper presented below.

Spectrochimica Acta Part A: Molecular and Biomolecular Spectroscopy 225 (2020) 117502

Contents lists available at ScienceDirect

Spectrochimica Acta Part A: Molecular and Biomolecular Spectroscopy

journal homepage: www.elsevier.com/locate/saa

Short Communication

One-step synthesis of gold nanoflowers of tunable size and absorption wavelength in the red & deep red range for SERS spectroscopy

Mathias Pacaud [a, b], Katel Hervé-Aubert [a], Martin Soucé [a], Alaa Abdelrhman Makki [a], Franck Bonnier [a], Amir Fahmi [b], Alexey Feofanov [c, d], Igor Chourpa [a, *]

[a] EA6295 Nanomédicaments et Nanosondes, Université de Tours, Tours, France
[b] Faculty Technology&Bionics, Rhein-Waal University of Applied Sciences, Kleve, Germany
[c] Shemyakin and Ovchinnikov Institute of Bioorganic Chemistry, Russian Academy of Sciences, Moscow, Russia
[d] Biological Faculty, Lomonosov Moscow State University, Moscow, Russia

ARTICLE INFO

Article history:
Received 16 May 2019
Received in revised form 27 August 2019
Accepted 29 August 2019
Available online 31 August 2019

Keywords:
Gold nanoflower AuNF
Localised surface plasmon resonance (LSPR) band
Surface-enhanced Raman scattering (SERS) spectroscopy

ABSTRACT

We describe a novel protocol for a one-step, seed-less, organic solvent- and surfactant-free synthesis of optically dense aqueous colloids of gold nanoflowers (AuNF), with tunable absorption wavelength between 620 and 800 nm. We demonstrate that simple variation of the ratio of two reagents allows the plasmonic band position to be tuned to any desired wavelength ± 5 nm, namely to those of the laser sources commonly used for SERS spectroscopy. The AuNF size distribution was sufficiently narrow, comparable to that known with seed-mediated synthesis. The AuNF have been validated as efficient aggregation-free substrates for surface-enhanced Raman scattering (SERS) spectroscopy using two common fluorescent dyes, Nile Blue and Crystal Violet, both thiol-free. Their fluorescence was quenched and SERS signal intensity was a linear function of the dye concentration, from nanomolar to micromolar range. Easy to prepare and to use, these AuNF appear as a particularly user-friendly and efficient way to obtain plasmonic substrates for SERS in the red and deep red spectral range.

© 2019 Elsevier B.V. All rights reserved.

1. Introduction

Gold nanoflowers (AuNF) have emerged during the past decade as novel plasmonic nanosystems absorbing light in the red - deep red range (600–900 nm, a part of the "tissue optical window" between 600 and 1200 nm) [1–3]. The AuNF are interesting for many applications [4,5], in particular as agents for photoinduced heating and substrates for surface-enhanced Raman scattering (SERS) spectroscopy [6]. Due to its high sensitivity, molecular specificity and selectivity, SERS spectroscopy is a rapidly developing analytical and bio-analytical technique. SERS excitation in the 630–850 nm region is favourable for bio-analytical SERS applications, because this wavelength range allows a compromise between minimal light interaction with biological tissues [1,2] and the good performance of laser sources and CCD detectors [3].

The SERS effect is observed for organic molecules situated in the vicinity of a nanostructured surface of a noble metal, often in the form of nanoparticles (NP), which displays collective oscillations of surface electrons called plasmons [6]. The SERS effect implies that the excitation wavelength coincides with the localized surface plasmon resonance (LSPR) band of the noble metal NP. Since isotropic smooth AuNP have their LSPR band around 530 nm, their use for SERS with higher wavelength excitation sources is possible only in the case of NP aggregation. For aggregation-free LSPR absorption in the red-deep red range, anisotropic gold nanosystems like nanorods (AuNR), nanostars (AuNS) and nanoflowers (AuNF) are being developed [4,5,7–13]. It has to be noted that the morphology of some short-tipped AuNS is very similar to that of AuNF. Unfortunately, AuNR and some long-spiked AuNS may have an intrinsical biotoxicity [7], due to their morphology [8] and/or due to the presence of surfactants like cetrimonium bromide (CTAB) employed in their formulation. Indeed, surfactant-free AuNS synthesized by Yuan et al. [9] had reduced toxicity and permitted an easy surface functionalization. Thus, surfactant-free synthesis of AuNF has to be preferred for applications like biosensing.

Although a certain number of protocols of generating AuNF and AuNS has been reported by various research groups [4,9–13] they typically involve at least two synthesis steps, corresponding to a nucleation-growth mechanism [14,15]. The first step consists in introducing some seeds (silver [12], gold [9] or magnetic NPs [10] of diameters ca. 5 nm), either synthesized independently or in situ. Nucleation of silver and gold seeds is usually reached with one of the stronger reducing agents such as $NaBH_4$ [4,5]. The second synthesis step is intended to favour slow anisotropic growth of AuNF or AuNS around the seeds, using a mild reducing agent like ascorbic acid or

* Corresponding author at: UFR de Pharmacie, 31 Avenue Monge, F-37200, France.
E-mail address: Igor.chourpa@univ-tours.fr (I. Chourpa).

https://doi.org/10.1016/j.saa.2019.117502
1386-1425/© 2019 Elsevier B.V. All rights reserved.

hydroxylamine. Size, shape and surface properties are usually controlled by the amount and nature of reducing agents and their ratio to the Au precursor. Anisotropic Au nanosystems can be synthesized in the presence of organic solvents and/or of capping agents like silver or other metal ions, surfactant molecules or polymers [4,5]. The latter are intended to direct the anisotropic growth along specific crystallographic directions or to stabilize the surface. As a result, prior to use of those AuNF or AuNS for SERS, further post-synthesis steps are usually required, in order to remove the solvents, the excess of seeds and reagents [4,5]. Only few seed-less [11] or surfactant-free [9,12] approaches have been reported so far. For instance, He et al. [11] have proposed a one-pot seedless protocol for the synthesis of AuNS, using ascorbic acid in the presence of silver nitrate ($AgNO_3$). The group of Vo-Dinh have published a systematic study of well-controlled geometry and optical response of gold nanostars using silver seeds but without surfactant [12].

To the best of our knowledge, the protocols of AuNF synthesis without seeds nor surfactant are even less common. For instance, Jena and Raj [13] used 5-hydroxyindole-3-acetic acid to generate, at room temperature, flower-like gold nanoparticles of a large, ca. 150 nm size, surprisingly showing two absorption bands at 545 and 1250 nm. Thus, there is no 'gold standard method' and there is still a need of a more convenient, rapid and efficient protocol for seed-less and surfactant-free synthesis of AuNF of controlled size and tunable LSPR band position within the 600–800 nm range.

In response to this need, we propose here a novel one-step synthesis method based on a mild chemistry in aqueous medium at room temperature.

2. Materials and methods

2.1. Chemicals

Gold (III) chloride trihydrate ($AuHCl_4.3H_2O$) (≥ 99.9%), trisodium citrate dihydrate ($HOC(COONa)(CH_2COONa)_2 \cdot 2H_2O$) (≥ 99.0%), sodium hydroxide (NaOH) (≥ 97.0%) and Crystal Violet were purchased from Sigma–Aldrich (Saint Quentin Fallavier, France). Hydroxylamine hydrochloride ($NH_2OH \cdot HCl$) (≥ 99.0%), and Polyvinylpyrrolidone (PVP, M_w 7000–11,000) were purchased from VWR (Fontenay-sous-Bois, France) and BASF (Levallois-Perret, France), respectively. Nile blue A, pure certified, was purchased from Acros Organics, (New Jersey, USA). All the reagents were used without further purification. Ultrapure water (Milli-Q) was used for the preparation of all solutions.

2.2. AuNF synthesis

Gold nanoflowers synthesis was carried out as follows: to 20 mL of water under vigorous magnetic stirring, aqueous solutions of hydroxylamine (0.1 M, volumes 0.3, 0.4, 0.45, 0.54, 0.56 or 0.64 mL), trisodium citrate (0.1 M, 1.0 mL) and sodium hydroxide (0.01 M, volumes 1.0, 1.0, 0.9, 0.9, 0.8 or 0.8 mL) were added. Upon addition of a freshly prepared aqueous solution of $HAuCl_4$ (0.01 M, volume 1.0 mL), the initial colourless solution immediately turned dark blue. The resultant colloid was stirred for ca. 30 s and transferred to a hermetically closed tube protected from light with aluminium foil. The final solution was kept at 20 ± 1 °C. In some cases, 0.25 mL of PVP aqueous solution (final concentration 13.5 μM) were added for better stability of the colloids.

2.3. Instrumental

UV–visible absorption spectra were acquired using a Genesys 10S UV–vis spectrophotometer (Thermo Scientific, France).

IR spectra were acquired with a Frontier spectrometer (Perkin Elmer, France) equipped with a Quest multiple reflection diamond attenuated total reflectance (ATR) accessory (Specac, UK) using dried 2 μL drops of NF suspension and citrate solution.

TEM experiments were carried out on a transmission electron microscope JEOL JEM-1011 (JEOL Inc., Peabody, MA, USA) operating at an acceleration voltage of 100 kV. AuNF in aqueous suspension were deposited on carbon-coated Cu grids. Excess water was removed by filter paper. The obtained samples were left to dry under ambient air. Image J software was used to measure the size distribution of AuNF, and for each particle, two perpendicular dimensions were measured. For each batch, the weighted average size was determined as the center of mass of the corresponding size distribution, calculated according to the equation: $D = \frac{\sum D_i N_i}{\sum N_i}$ where D_i is AuNF dimension range (0–10 nm presented as 5 nm, 10–20 nm presented as 15 nm, … 140–150 nm presented as 145 nm), where N_i is the number of AuNF in the dimension range D_i.

The mean hydrodynamic diameter D_H values (z-average) were measured using dynamic light scattering (DLS, Malvern HPPS, Malvern Instruments, UK), at 25 °C and with a He–Ne laser (4 mW, 633 nm, scatter angle 173°). Each measurement was done in triplicate.

The SERS spectra were recorded with a confocal Raman microspectrometer LabRam (Horiba SA, France) equipped with an EM CCD air-cooled detector, a 690 nm laser source (RO691-PLR45, Ondax Inc., Monrovia, CA, USA) providing 26.9 mW on the sample. The spectra were collected via a 10× objective focused on the top of the sample solution (200 μL) placed in a well of a P96 multiwell plate. The spectral data acquisition and treatment were done using a LabSpec software (Horiba SAS, Villeneuve d'Ascq, France).

3. Results and discussion

3.1. AuNF synthesis

Our protocol uses optimized quantities of well-known reagents that are typical for gold reduction (Scheme 1): hydroxylamine (NH_2OH, Solution 1) as a reductant, trisodium citrate (Na_3Citrate, Solution 2) as a stabiliser for particles, sodium hydroxide (NaOH, Solution 3) as a main pH regulator and tetrachloroauric(III) acid ($HAuCl_4$, Solution 4) as a gold precursor (see Materials and methods for more details). The reagent concentrations and volumes are easy to remember, as described below. First of all, aqueous solutions of all the reagents are prepared, at concentrations of 0.1 M for the Solutions 1–3 and 0.01 M for the Solution 4. The preparation is started by adding the Solutions 1 (0.3–0.65 mL), 2 (1 mL) and 3 (0.8–1 mL) to 20 mL of water under vigorous stirring at ambient temperature (21 ± 1 °C). The volumes of the Solutions 1 and 3 are varied in order to adjust the NH_2OH/NaOH molar ratio (hereafter called R) to the values of 0.3, 0.4, 0.5, 0.6, 0.7, 0.8. Then, 1 mL of the Solution 4 is injected into this mixture: the colourless solution immediately turns dark blue (Scheme 1A) and, after ca. 30 s, the stirring can be stopped. No washing steps are needed, the AuNF colloids are useable for SERS spectroscopy as is, and are chemically and physically stable for several days, till about a week for certain batches. Nevertheless, they have to be protected against light by aluminium foil and stored hermetically closed to minimize their oxidation.

In the context of the nucleation-growth mechanism described above, our rapid AuNF synthesis seems to correspond to almost instantaneous nucleation of seeds (Step 1 in Scheme 1B) followed by appearance of anisotropic structures (Step 2) and their fast growth to give nanoflowers (Step 3) with characteristic petal-like structures (Scheme 1 C). This rapid growth in presence of citrate and chloride anions adsorbed on the gold surface may be the reason of its anisotropic nature in the absence of silver ions and surfactants.

Variations in citrate or gold concentration around the optimum value (10:1 M ratio) do not allow controlling the LSPR position. This behaviour is different from that described by Ji et al. [16] who had

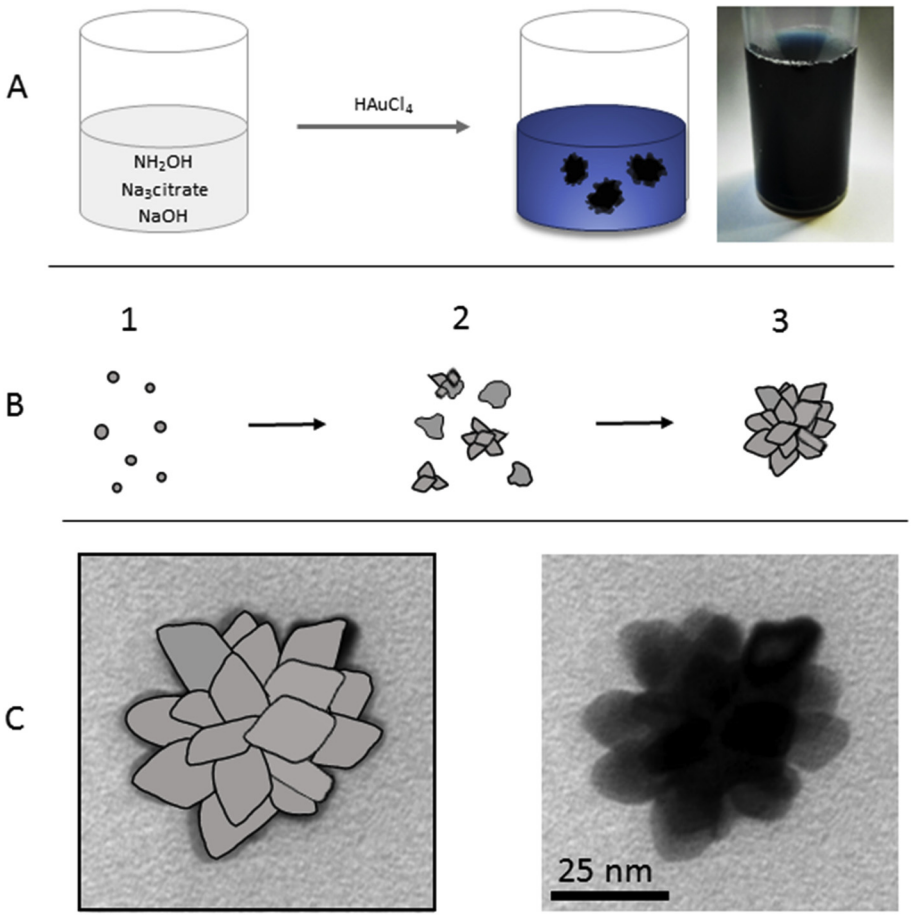

Scheme 1. A. Schematic description of the AuNF synthesis in aqueous media and photograph of the final colloid (optical density between 1.4 and 1.7). B. Hypothetic mechanism of the synthesis including 3 steps: seed formation (Step 1), anisotropic structure initiation (Step 2) and growth to form AuNF (Step 3). C. Schematic drawing of the petal-like morphology of an AuNF (left) compared to its TEM image (right).

shown that the $HAuCl_4/Na_3Ct$ ratio affected both the pH and the growth of isotropic gold nanocrystals at elevated temperatures. In our study, synthesis without any citrate leads to colloids of reddish colours, i.e. with the LSPR band below 600 nm. Therefore, the presence of citrate is mandatory for successful AuNF synthesis by our method.

3.2. AuNF characterisation

The ratio R is the most critical parameter that affects the LSPR band position. An increase in R from 0.3 to 0.8 leads to a red shift of the LSPR band from ca. 620 to ca. 800 nm (Fig. 1). Between 0.4 and 0.8, the LSPR shift is a nearly linear function of R (Fig. 1B) and it is possible to adjust the LSPR position to any of three wavelengths of the laser sources most widely used in bio-analytical spectroscopy: 633 nm ($R = 0.4$), 690 nm ($R = 0.6$) and 785 nm ($R = 0.8$). The LSPR band position was reproducible with a ± 5 nm variation. The maximum absorbance for these LSPR bands was between 1.4 and 1.7.

The pH plays a very important role in such a synthesis. During the reaction, it affects the reactivity of gold complexes [17] and therefore, the kinetics of nanocrystal nucleation and growth. The high pH conditions are known to be favourable for gold reduction. Prior to the addition of gold precursor, the pH of the solutions

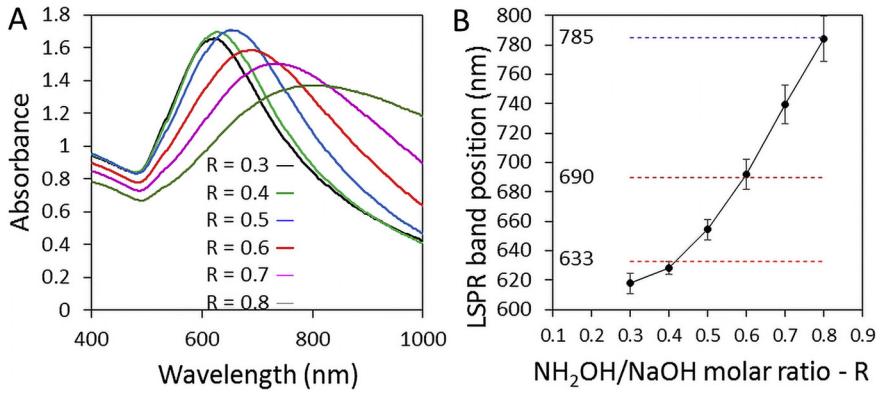

Fig. 1. (A) UV–vis spectra of AuNF synthesized using different $R = NH_2OH/NaOH$ molar ratio. (B) The LSPR band position vs R.

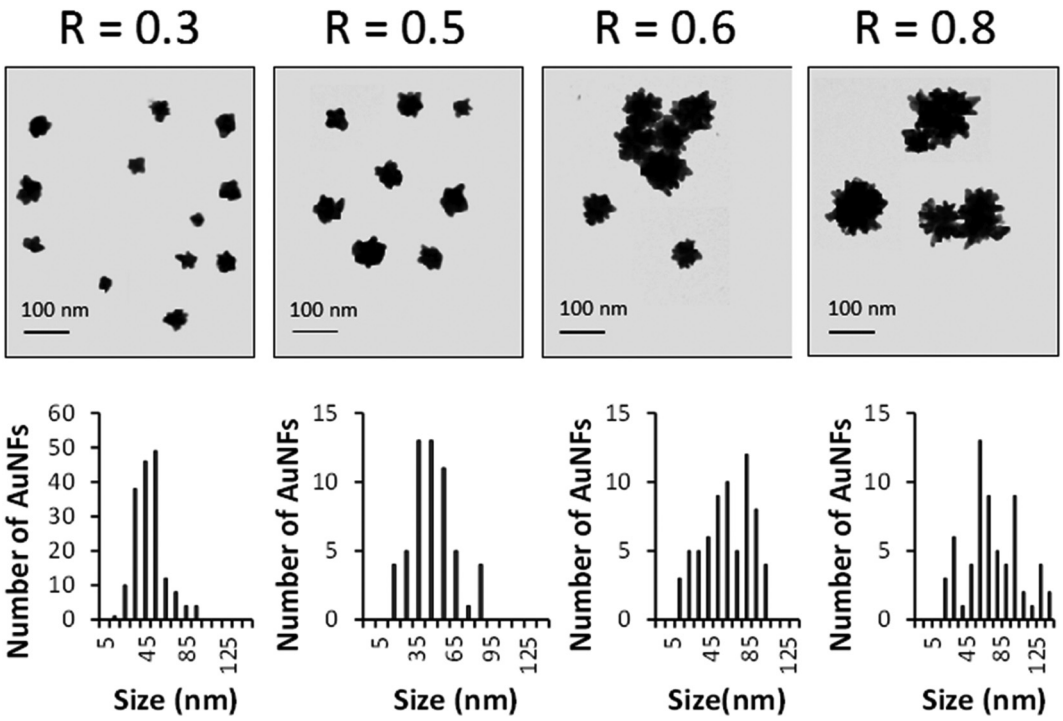

Fig. 2. Top: Selection of typical TEM images of AuNF synthesized using $R = 0.3$, 0.5, 0.6 and 0.8. Bottom: size distribution histograms. The centre of mass of the respective histograms corresponds to the size of 49, 56, 75 and 89 nm.

ranges from 11.5 to 10.6 as a function of R (0.3 to 0.8), as expected from the respective concentrations of $NH_2OH.HCl$ and NaOH.

After the AuNF synthesis, the final pH decreases for all the colloids, down to about 10.9 for $R = 0.3$ and to 6.7 for $R = 0.8$. This is in agreement with the fact that both auric acid dissociation and its reduction generate H^+ species [18]. Counting only dissociation of auric acid, pH should still remain well above 10, permitting a rapid onset of reaction. The H^+ ions liberated due to the redox reaction further lower pH, reaching almost neutral for conditions of high R. At all the pH values described above the citrate is in anionic form (trivalent or partially divalent) to be adsorbed on the gold surface, thus playing a role both in the AuNF growth and colloidal stability. The presence of citrates in the AuNF batches can be confirmed by the characteristic bands of citrates the IR spectra (Figure SI2).

According to transmission electron microscopy (TEM) data (Fig. 2), the red shift of the LSPR band corresponds to bigger AuNF with an increased size and/or number of the 'petals' giving them a flower-like morphology. Coupling of plasmons of neighbouring petals is supposed to favour formation of 'hot spots' where the SERS effect is particularly strong. As seen from the TEM images and the histograms in Fig. 2, the size distribution was narrower in the populations of smaller AuNF. The centre of mass of the histograms corresponds to the size of 49, 56, 75 and 89 nm for the R values of 0.3, 0.5, 0.6 and 0.8, respectively. The hydrodynamic diameter D_H (z-average data from DLS), which includes the hydration layers around AuNF, increases from ca. 84 nm to ca. 112 nm.

As noticed above, the colloids are stable for about a week. However, the AuNF batches of higher R (bigger size and lower pH) show more pronounced sedimentation with time and are more prone to aggregation with time.

It is possible to stabilize the colloids of AuNF for at least a month by post-synthesis addition of 13.5 μM of PVP. As shown in Fig. SI1 (SI), PVP reduces the absorbance at the long-wavelength side of the LSPR band, presumably due to re-dispersion of some aggregates. As expected, the effect of PVP on the LSPR band shape is more significant for the bigger AuNF at nearly neutral pH (absorption

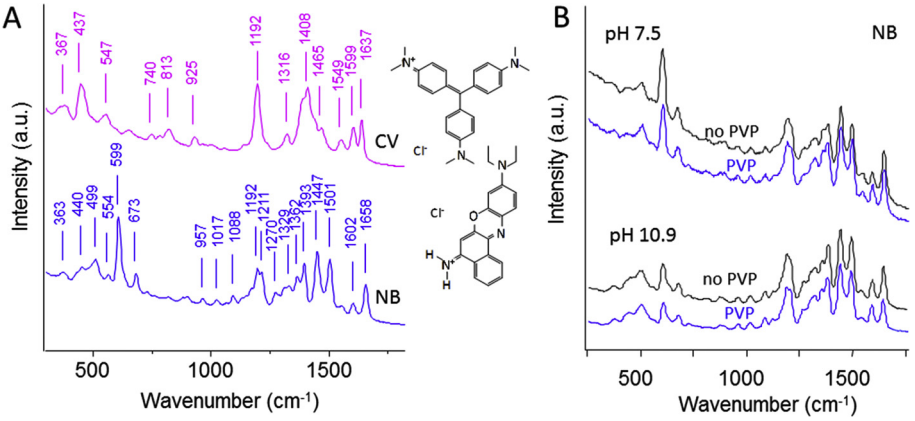

Fig. 3. A. Chemical structures of two dyes, Crystal Violet (CV) and Nile Blue (NB) and their SERS spectra obtained on AuNF with $R = 0.6$. B. Comparison of the SERS spectra of NB on AuNF in absence and in presence of PVP at basic and neutral aqueous solutions.
The dye concentration was 5 μM. Each spectrum is an average of 16 scans of 1 s.

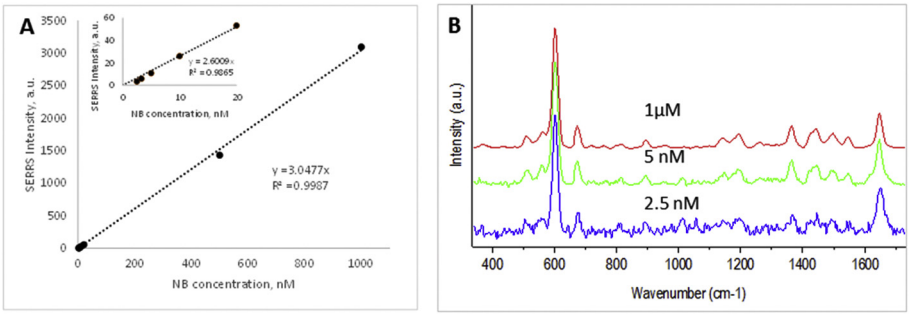

Fig. 4. A. SERS intensity (area of Raman bands in the range between 250 and 1800 cm^{-1}) vs NB concentration, from 2.5 to 100 nM (from 2.5 to 20 nM in the inset). The data presented are averages of three independent measurements. B. Typical SERS spectra of NB at micromolar and nanomolar concentrations. The intensities are normalized and offset for easier comparison.

maximum around 690 nm and above, Fig. SI1 1A) while it has almost no effect for the colloids of smaller AuNF at higher pH (absorption maximum at 620–660 nm, Fig. SI1 B). While useful to store big AuNF colloids for an extended time, the post-synthesis addition of PVP was optional, taking into account the ease and rapidity of producing a fresh batch whenever needed.

3.3. Analytical validation of the AuNF

For the SERS validation experiments with a 690 nm laser excitation, the most appropriate AuNF have the LSPR band maximum at ca. 690 nm ($R = 0.6$, pH 7.2). For this validation, we intentionally selected chromophores void of thiol groups and therefore having much lower affinity to the gold surface than rhodamine [19] and thiolated dyes [20] often used in the literature.

The sample preparation for SERS on our AuNF is very convenient: a 10-fold dilution of the analyte solution in the AuNF colloid placed into a well of a 96-multiwell plate. In this manner, we successfully obtained SERS spectra of two blue dyes, Nile Blue and Crystal Violet (absorption maxima in water at 635 and 590 nm, respectively) (Fig. 3A).

It has to be underlined that added PVP did not give its own signal and did not change the SERS signal of the NB dye (Fig. 3B). This is true under both neutral and basic conditions. As expected the pH increase from neutral to basic conditions affects the relative intensity of SERS bands of NB and contributes to a decrease of the fluorescence background. The only effect noticeable with PVP was seen as a need of about 5–10 min delay after the NB incubation to observe an optimal SERS/fluorescence ratio. This time would correspond to the diffusion of the dye through the polymeric layer to reach the gold surface.

This shows the interest of a substrate with a minimal presence of polymer or surfactant: (i) to reduce its effect on the adsorption and thus the detection of analytes [11] and (ii) to facilitate further post-functionalization with some molecules of interest.

On the AuNF coated with PVP, the SERS intensity was a linear function of the NB dye concentration from nanomolar to micromolar range (Fig. 4A). Using a rapid SERS spectra acquisition (16×1 *sec*), we observed the detection limits situated in the nanomolar range (2.5 nM for NB – Fig. 4B) while it was possible to go below using longer acquisition times. As shown in Fig. 4B, the signal stays the same (the fingerprint bands are recognizable), just noise goes up on dilution.

4. Conclusions

In conclusion, the novel protocol we propose herein presents several significant advantages compared to those previously published for synthesis of AuNF: in addition to be facile and rapid (one-step, seed-less), it avoids the presence of organic solvents or surfactants and of other metals than gold. Moreover, our method permits to tune the size of AuNF between 50 and 90 nm and the corresponding LSPR band position between 620 and 800 nm. The most critical parameter of the synthesis has been determined to be the hydroxylamine/NaOH molar ratio, which regulates both the reductant content and the pH. Obviously, for a good reproducibility of the data, the temperature has to be controlled, since it plays a role in the reaction kinetics. As noted above, AuNF were not formed without addition of citrate. Together with citrates, chloride ions binding to the surface may also be essential to the anisotropic structure of the surface. The surfactant-free colloids are stable in water for several days and addition of a low concentration of PVP improves their long-term stability without affecting their aggregation-free SERS activity for organic dyes with relatively low affinity for gold. We believe that such a user-friendly wet chemistry protocol for rapid synthesis of AuNF should have very promising perspectives for bio-analytical SERS spectroscopy as well as for other plasmonic methods in the red-deep red range.

Supplementary data to this article can be found online at https://doi.org/10.1016/j.saa.2019.117502.

Declaration of competing interest

The author declares no conflict of interest.

Acknowledgements

The authors acknowledge funding from the following grants in the framework of the MINERVA project (ERA-NET RUS PLUS program): Russian Foundation for Basic Research: RFBR 16-54-76013 (Russia), Bundesministerium für Bildung und Forschung: BMBF 01DJ16019 (Germany) and Ministère de l'Education Nationale, de L'enseignement Supérieure et de la Recherche: MENESR N°321 (France). The authors are grateful to Dr. Stéphanie David for her help with experimental design, to Julien Burlaud-Gaillard (the IBiSA Electron Microscopy Facility, University of Tours) for TEM images and to Hiba Chamekh for technical assistance.

References

[1] S.J. Norton, T. Vo-Dinh, Theoretical Models and Algorithms in Optical Diffusion Tomography, Biomedical Photonics Handbook, CRC Press LLC, 2003, https://doi.org/10.1201/9780203008997. ISBN 0-8493-1116-0.
[2] R. Weissleder, A clearer vision for *in vivo* imaging, Nature Biotechnol 19 (2001) 316–317, https://doi.org/10.1038/86684.
[3] A. Smith, M.C. Mancini, S. Nie, Bioimaging: second window for in vivo imaging, Nat. Nanotechnol. 4 (2009) 710–711, https://doi.org/10.1038/nnano.2009.326.
[4] P.R. Sajanlal, T.S. Sreeprasad, A.K. Samal, T. Pradeep, Anisotropic nanomaterials: structure, growth, assembly, and functions, Nano Reviews 2 (2011), 5883, https://doi.org/10.3402/nano.v2i0.5883.

[5] X. Gong, Y. Bao, C. Qiu, C. Jiang, Individual nanostructured materials: fabrication and surface-enhanced Raman scattering, Chem. Commun. 48 (2012) 7003–7018, https://doi.org/10.1039/C2CC31603J.
[6] L.E. Jamieson, S.M. Asiala, K. Gracie, K. Faulds, D. Graham, Bioanalytical measurements enabled by surface-enhanced Raman scattering (SERS) probes, Annu Rev Anal Chem (Palo Alto, Calif) 10 (2017) 415–437, https://doi.org/10.1146/annurev-anchem-071015-041557.
[7] I. Fratoddi, I. Venditti, C. Cametti, M.V. Russo, How toxic are gold nanoparticles? The state-of-the-art, Nano Res. 8 (2015) 1771–1799, https://doi.org/10.1007/s12274-014-0697-3.
[8] L. Rodriguez-Lorenzo, R.A. Alvarez-Puebla, F.J. Garcia de Abajo, L.M. Liz-Marzan, Surface enhanced Raman scattering using star-shaped gold colloidal nanoparticles, J. Phys. Chem. C 114 (2010) 7336–7340, https://doi.org/10.1021/jp909253w.
[9] H. Yuan, C.G. Khoury, H. Hwang, C.M. Wilson, G.A. Grant, T. Vo-Dinh, Gold nanostars: surfactant-free synthesis, 3D modelling, and two-photon photoluminescence imaging, Nanotechnology 23 (2012), https://doi.org/10.1088/0957-4484/23/7/075102. Article 075102.
[10] C. Li, T. Chen, I. Ocsoy, G. Zhu, E. Yasun, M. You, C. Wu, J. Zheng, E. Song, C.Z. Huang, W. Tan, Gold-coated Fe_3O_4 Nanoroses with five unique functions for Cancer cell targeting, imaging and therapy, Adv. Funct. Mater. 24 (2014) 1772–1780, https://doi.org/10.1002/adfm.201301659.
[11] S. He, M.W.C. Kang, F.J. Khan, E.K.M. Tan, M.A. Reyes, J.C.Y. Kah, Optimizing gold nanostars as a colloid-based surface-enhanced Raman scattering (SERS) substrate, J. Opt. 17 (2015), 114013, https://doi.org/10.1088/2040-8978/17/11/114013.
[12] A.S. De Silva Indrasekara, S.F. Johnson, R.A. Odion, T. Vo-Dinh, Manipulation of the geometry and modulation of the optical response of surfactant-free gold nanostars: a systematic bottom-up synthesis, ACS Omega 3 (2018) 2202–2210, https://doi.org/10.1021/acsomega.7b01700.
[13] B.K. Jena, C.R. Raj, Seedless, Surfactantless room temperature synthesis of single crystalline fluorescent gold nanoflowers with pronounced SERS and electrocatalytic activity, Chem. Mater. 20 (2008) 3546–3548, https://doi.org/10.1021/cm7019608.
[14] J. Turkevich, P.C. Stevenson, J. Hillier, A study of the nucleation and growth processes in the synthesis of colloidal gold, Discuss. Faraday Soc. 11 (1951) 55–75, https://doi.org/10.1039/DF9511100055.
[15] G. Frens, Controlled nucleation for the regulation of the particle size in monodisperse gold suspensions, Nat. Phys. Sci. 241 (1973) 20–22, https://doi.org/10.1038/physci241020a0.
[16] X. Ji, X. Song, J. Li, Y. Bai, W. Yang, X. Peng, Size control of gold nanocrystals in citrate reduction: the third role of citrate, J. Am. Chem. Soc. 129 (2007) 13939–13948, https://doi.org/10.1021/ja074447k.
[17] D.V. Goia, E. Matijević, Tailoring the particle size of monodispersed colloidal gold, Colloids and Surfaces, A 146 (1999) 139–152, https://doi.org/10.1016/S0927-7757(98)00790-0.
[18] V. Soni, R.N. Mehrotra, Kinetics and mechanism of oxidation of hydroxylamine by tetrachloroaurate(III) ion, Transit. Met. Chem. 28 (2003) 893–898, https://doi.org/10.1023/A:1026330125535.
[19] A. Jaworska, T. Wojcik, K. Malek, U. Kwolek, M. Kepczynski, A.A. Ansary, S. Chlopicki, M. Baranska, Rhodamine 6G conjugated to gold nanoparticles as labels for both SERS and fluorescence studies on live endothelial cells, Mikrochim. Acta 182 (2015) 119–127, https://doi.org/10.1007/s00604-014-1307-5.
[20] M. Gühlke, Z. Heiner, J. Kneipp, Surface-enhanced Raman and surface-enhanced hyper-Raman scattering of thiol-functionalized carotene, J Phys Chem C Nanomater Interfaces 120 (2016) 20702–20709, https://doi.org/10.1021/acs.jpcc.6b01895.

Supporting Information

One-step synthesis of gold nanoflowers of tunable size and absorption wavelength in the red & deep red range for SERS spectroscopy

Mathias Pacaud,[a,b] Katel Hervé-Aubert,[a] Martin Soucé,[a] Alaa Abdelrhman Makki,[a] Franck Bonnier,[a] Amir Fahmi,[b] Alexey Feofanov [c,d] and Igor Chourpa*[a]

[a] EA6295 Nanomédicaments et Nanosondes, Université de Tours, 31 Avenue Monge, F-37200, Tours, France. E-mail: igor.chourpa@univ-tours.fr

[b] Faculty Technology&Bionics, Rhein-Waal University of Applied Sciences, Kleve, Germany.

[c] Shemyakin and Ovchinnikov Institute of Bioorganic Chemistry, Russian Academy of Sciences, Moscow, Russia.

[d] Biological Faculty, Lomonosov Moscow State University, Moscow, Russia.

Results

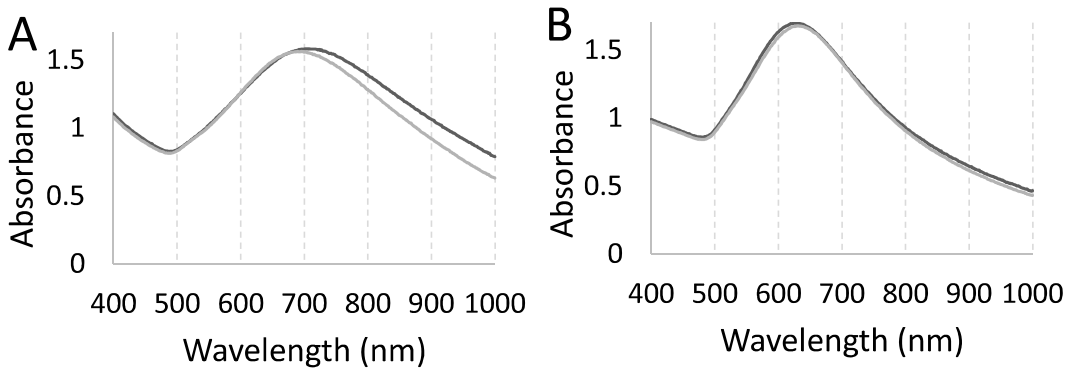

Figure SI1. UV-vis spectra of the AuNF with R = 0.6 (A, abs max at 705 nm) and R = 0.3 (B, abs max at 625 nm), as prepared (black curves) and 12 hours after being incubated with PVP (grey curves).

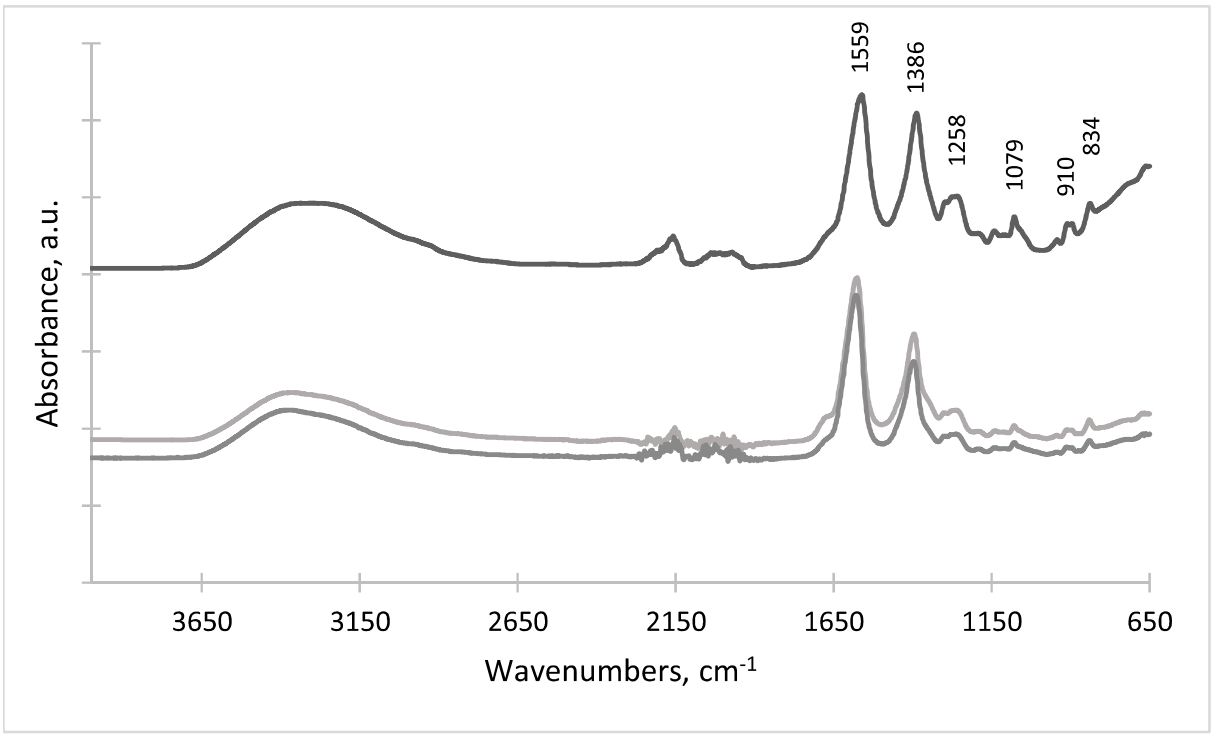

Figure SI2. IR spectra of citrate ionic solution (black) and of the AuNFs (grey) corresponding to R = 0.3 and R = 0.6 (from top to bottom). The positions of the main citrate bands are indicated.

CHAPTER IV. RESULTS. Stabilization of the gold nanoflowers using surface coating

Introduction *(French version)*

English version down below (p. 74).

Suite aux résultats décrits dans le chapitre précédent, nous disposons du protocole nous permettant de fabriquer des AuNFs avec des propriétés plasmoniques adaptées à la longueur d'onde désirée. Bien qu'il soit possible de préparer un nouveau lot chaque jour, nous nous sommes intéressés à étudier la stabilité des lots dans le temps.

La première partie de ce chapitre est consacrée à l'étude de la stabilité physique et chimique des AuNFs. La taille et la forme des AuNFs seront évaluées en MET (microscopie électronique en transmission), leur diamètre hydrodynamique moyen (D_H) par la technique de diffusion dynamique de la lumière (DLS comme *dynamic light scattering)* et leur bande LSPR au moyen de la spectrophotométrie UV-visible.

La deuxième partie de ce chapitre traite de la stabilisation des AuNFs en utilisant divers matériaux, allant des polymères à la matrice de silice. En plus des mesures TEM, DLS et UV-vis, nous avons effectué des tests de spectroscopie SERS avec un colorant fluorophore (le bleu de nil), afin d'évaluer l'efficacité analytique de nos AuNFs modifiées en surface.

Introduction *(English version)*

Following the results described in the previous chapter, we dispose of the protocol allowing us to make the AuNFs having plasmonic properties tuned to the desired wavelength. Although it was possible to prepare a new batch each day, we were interested to study the batches stability with time.

The first part of this chapter is devoted to the study of the physical and chemical stability of the AuNFs. The size and shape of the AuNFs will be assessed in TEM (transmission electron microscopy), their average hydrodynamic diameter (D_H) with DLS (dynamic light scattering) and their LSPR band with UV-vis spectrophotometry.

The second part of this chapter deals with the stabilization of the AuNFs using various materials, from polymers to silica matrix. In addition to TEM, DLS and UV-vis measurements, we performed SERS spectroscopy assays with a fluorophore dye (Nile blue), in order to evaluate the analytical efficiency of our surface-modified AuNF.

1. Time-dependant evolution of the AuNF colloids

We noticed that the visual aspect of the suspension of surfactant-free AuNFs (produced at NH_2OH/NaOH molar ratio R = 0.3) stored in darkness at 20°C and normal pressure was changed with time – its color shifted from dark blue to violet then to reddish. The LSPR band of these samples observed by UV-vis spectroscopy was progressively narrowed and blue-shifted, from 620 to 605 nm within 15 min to ca. 545 nm within 2 hours and to 535 nm within 24 hours (Figure 19.A and B). From 24 to 48 hours, a plateau is observed for the LSPR band position. As discussed in chapter I, such changes in the LSPR band position and shape should indicate the decrease of the number and/or of the length of petals of the AuNFs. This hypothesis has been confirmed with the TEM data recorded 24 hours after the synthesis and shown in Figure 19.D. It has to be noted that the synthesis of the AuNF suspensions was repeated many times, in different cleaned vials (glass or plastic), but the degradation of the petals happened in any case. New reagents were purchased but the same kinetic of the petal degradation was observed. The suspensions were wrapped in aluminum foil and stored in darkness. So, if light might play a role, it is not the main parameter involved in the process. One may suppose that this degradation of the petals over time happens via an oxidation mechanism which involves the oxygen dissolved in the aqueous medium. As expected for a chemical reaction, the petals degradation was slower at 4°C than at 25°C (Figure 20). Thus, the temperature has an effect on petal stability.

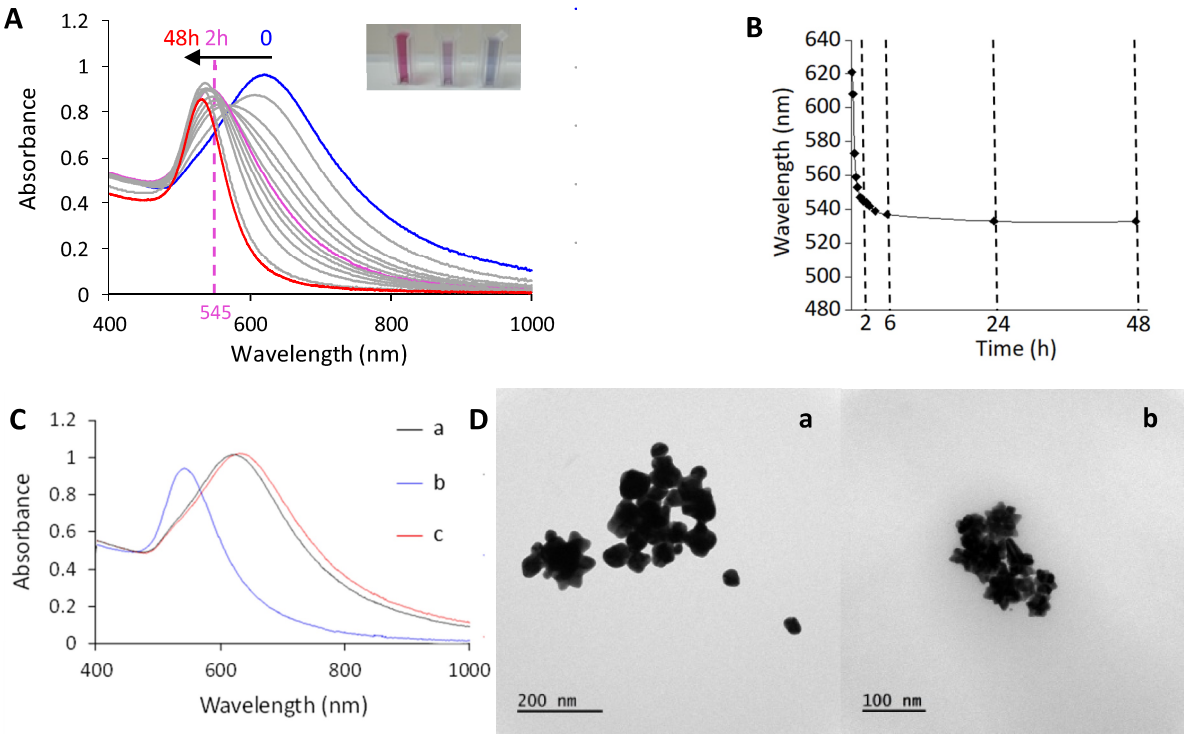

Figure 19. A: Evolution over the time of the absorbance spectra of the surfactant-free AuNFs (from the right to the left). The inset represents the evolution of the colour of the oxidising suspension over the time (from the right to the left). **B: Diagram showing the evolution of the LSPR band position of the surfactant-free AuNFs** over 48 hours. **C: Comparison of the absorbance spectra** of: surfactant-free AuNF freshly synthesized (a), after 24h hours at 20°C in darkness, either in water (b) or in an aqueous solution of PVP (c). **D: TEM micrographs** of surfactant-free (a) and PVP-coated AuNFs (b), both after 24 hours in darkness at 20°C and normal pressure.

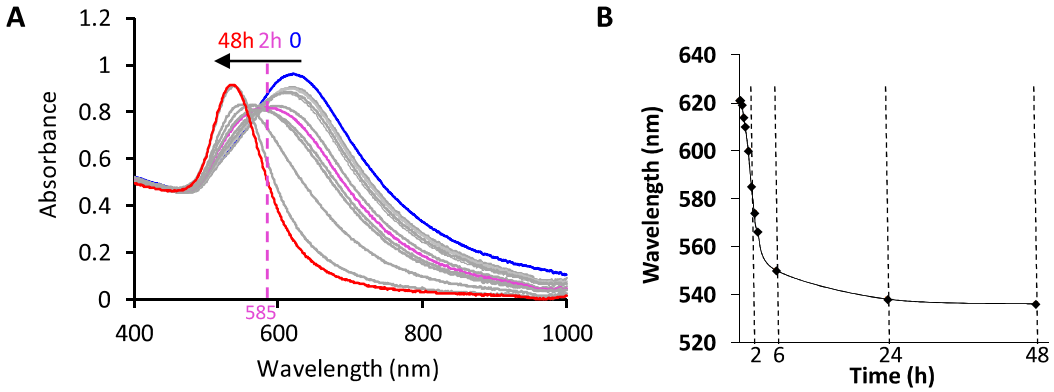

Figure 20. A: Evolution over the time of the absorbance spectra of the surfactant-free AuNFs LSPR band stored at 4°C (from the right to the left). **B: Diagram showing the evolution of the position of the maximum absorption peak** over 48 hours.

In contrast to the LSPR band of surfactant-free AuNFs (blue-shifted of 87 nm and significantly narrower in 24 hours), the AuNFs incubated with 0.5 mg/mL of PVP just after their synthesis, preserved their color and their UV-visible absorption spectra for a long time. Except for an immediately occurred slight red-shift (+10 nm), certainly induced by the polymer-related change of the local polarity of the AuNF surface, no other changes were observed upon the PVP addition. The LSPR band kept a very close shape to the original signal of the freshly prepared surfactant-free AuNFs, even 24 hours and more after their synthesis (Figure 19.C and Figure 21). The TEM pictures (Figure 19.D) confirm that the AuNFs coated with PVP preserved their characteristic petal-like structures over 24 hours post-synthesis: the estimated average dimensions of the petals were 13.2 ± 2.9 nm long (54 % of the total diameter of the AuNF) and 8.1 ± 0.9 nm large (Figure 23).

Therefore, in the presence of PVP, the gold nanoflower structure is preserved in the aqueous medium. According to our data, for at least 8 days, the maximum absorption peak of the coated AuNFs (Figure 21.A) remained at 630 nm with no significant change of its intensity or shape. Even after two centrifugation cycles (3000 rcf, 30 min at 20°C), the PVP-coated AuNF (AuNF@PVP) remained stable for a long time, until 14 additional days at least (Figure 21.B).

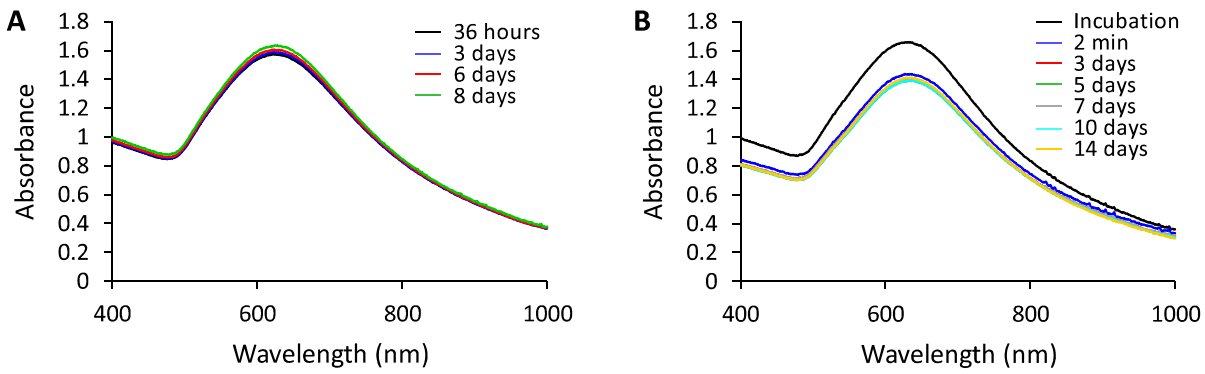

Figure 21. A: Stability over the time of the LSPR band of the AuNF@PVP. B: Comparison of the absorbance spectra of the AuNF@PVP batch before (black curve) and once centrifugated twice then aged of 2 min, 24 h, 3, 7, 10 and 14 days.

These results (no blue-shift due to oxidation and no enlargement to the red due to aggregation) indicate that PVP protects both morphology and plasmonic properties as the colloidal stability of the AuNFs.

2. Effect of the temperature on the synthesis of the AuNFs

The data presented in this section correspond to a study that is the subject of a paper under preparation.

Since the petal growth is intended to be favored by slow reaction kinetics, we studied the effect of low temperature (0°C) on it. For this, ice-cooled solutions were mixed using a magnetic stirrer, in glassware inserted in ice. For comparison, control reactions were made similarly but using solutions heated to 25°C. We studied here the temperature effect on two kinds of batches prepared at R = 0.3 and R = 0.6. In order to avoid the petal degradation, the batches were stabilized by the addition of PVP immediately after their synthesis.

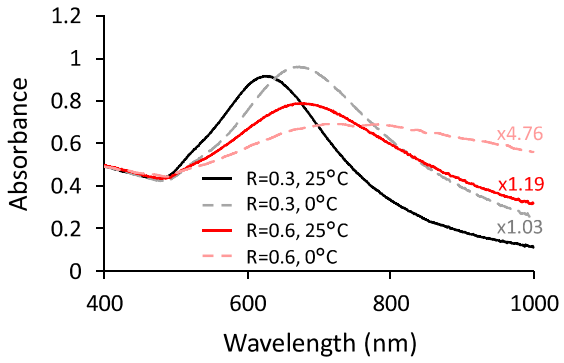

Figure 22. LSPR bands of AuNF synthesized at two different temperatures, 0°C and 25°C, at NH_2OH/NaOH molar ratio R = 0.3 (dashed grey and solid black curves, respectively) and R = 0.6 (dashed pink and solid red curves respectively). The spectra were normalized on the intensity of the black curve at 400 nm, for easier comparison.

For both R values (Figure 22), the lowering of the synthesis temperature to 0°C, compared to 25°C, leads to the LSPR band enlargement and shift to higher wavelengths: from 625 to 670 nm (+45 nm) at a R = 0.3 and from 680 to 780 nm (+100 nm) at a R = 0.6. The TEM images (Figure 23) show that, at a given R value, for the AuNFs which grown at 0°C the petals formed are more numerous and longer than when the reaction is made at 25°C. The overall size (diameter) of the AuNF is increased. This effect was much stronger with R = 0.3 than with R = 0.6. The possible explanation of this effect is that, when the gold reduction reaction is slowed down at low temperature, instead of generating new gold nuclei, it is favored to take place on the existing NPs, in particular, to grow up their petals. Interestingly, the nanoflower size and

petals grown up more at R = 0.3 and 0°C than at R = 0.6 and 25°C. In addition, at R = 0.3, the petals seem to be larger (with a pyramid-like shape) while at R = 0.6 they are narrower (with a rod-like shape) (Figure 23).

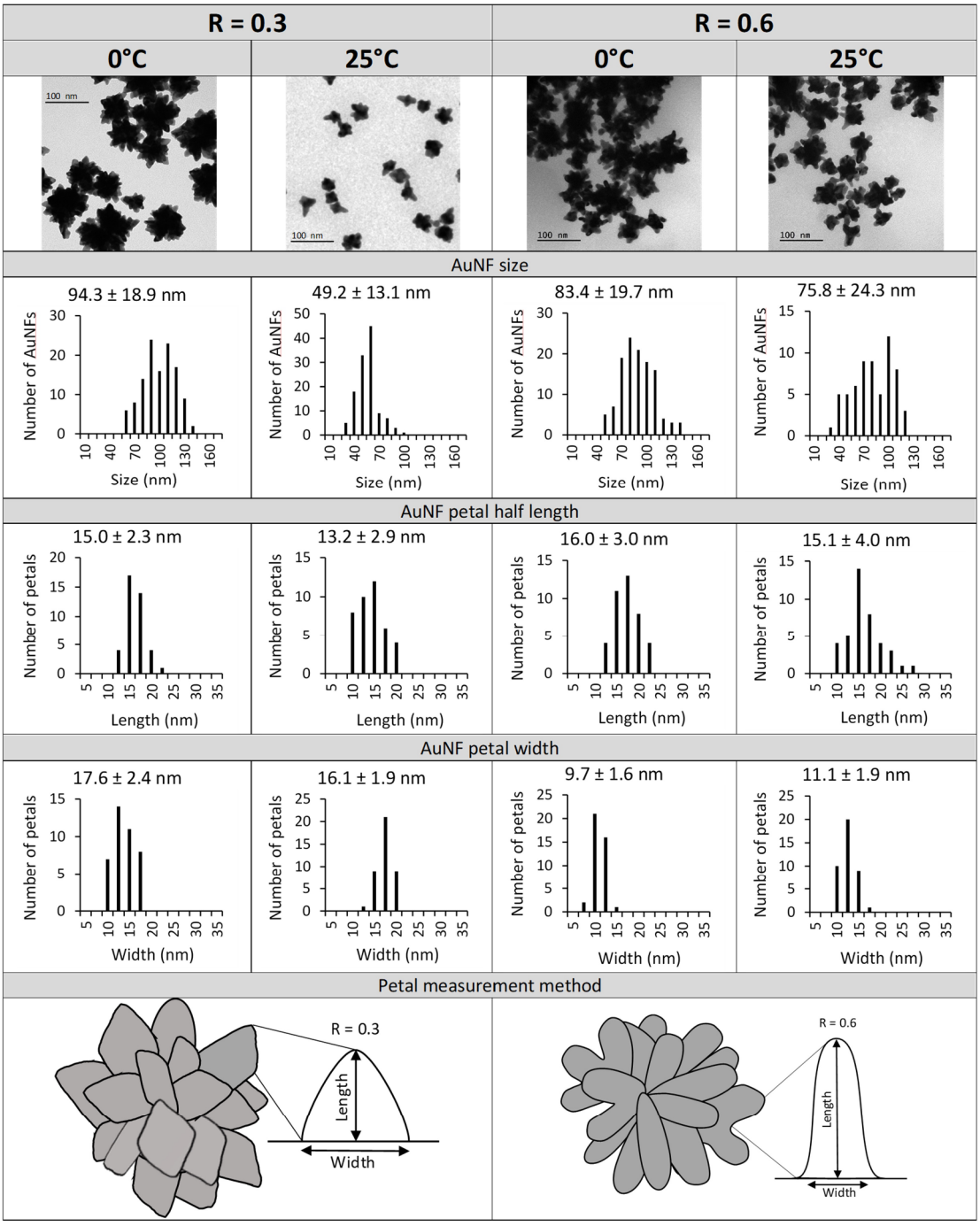

Figure 23. TEM analysis of the AuNFs synthesized at 0°C and 25°C at R = 0.3 and 0.6. All the pictures are on the same scale. The histograms below show the distribution of the AuNF size, petal length, and width as seen in the TEM images. For the size, two orthogonal diameters were

measured on each of 60 nanoflowers randomly selected for each batch. The petals' length and width were measured as shown in the schemes at the bottom.

Thus, the temperature has an important influence on the kinetics of the formation of the AuNFs leading to structural and morphological changes. The characteristics of the petal layer at the surface of the AuNFs can be tuned only by playing on the synthesis temperature, without changing the R ratio. Therefore, it is then possible to generate AuNF suspensions with an LSPR band close to 700 nm, setting the temperature of the synthesis medium at 0°C and the R ratio at 0.3 or setting the medium temperature to 25°C and the R ratio at 0.6. However, despite the same LSPR band position the TEM pictures show different structures between the two batches of AuNFs.

3. Effect of the AuNF coating with polymers other than PVP (PEG, Pluronics F68 and F127, alginates and chitosan)

In addition to PVP, structure shown in Figure 24, which is a neutral polymer possessing a polar carbonyl group, other polymers are known to be useful for NP coating to improve their colloidal stability and biocompatibility. Therefore, we decided to explore the effect of other well-known hydrophilic biocompatible polymers, such as polyethylene glycol (PEG, neutral in charge), Pluronics (copolymer combining hydrophilic poly(ethylene oxide) (PEO) and hydrophobic poly(propylene oxide) (PPO) blocks), alginates (copolymer of mannuronates and guluronates, both carrying negatively charged COO^- groups) and chitosan (positively charged due to its NH_3^+ groups). In this manner, one can monitor the polymer-gold interaction as a function of the polymeric chain polarity and presence of positive or negative charges.

For each polymer, we studied their effects on the LSPR band of the AuNFs (seen in UV-vis spectroscopy) and on their SERS activity (seen with a Raman microspectrometer equipped with a 690 nm laser source) of a 1 µmol/L aqueous solution of Nile blue (NB) - a fluorescent dye absorbing in red and emitting in deep red. These effects were studied at two values of the Polymer/Au w/w ratio defined as R2 = 10 and 0.01 (except for the PEG which was studied only at R2 = 10).

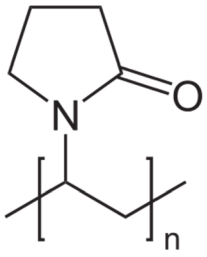

PVP

Figure 24. Chemical structure of Polyvinylpyrrolidone (PVP).

3.1. Coating the AuNFs with polyethylene glycol (PEG)

Polyethylene glycol (PEG) (Figure 25) is a neutral but hydrosoluble polymer which is food and drug administration (FDA) approved because of its low toxicity and immunogenicity. The PEG chains can be of variable lengths [116]. By the mean of PEGylation (linking molecules of NPs to one or more PEG chains), PEG-NP and PEG-drug conjugates have been generated and have shown several advantages: a prolonged residence in the body, a decreased degradation by metabolic enzymes and a reduction or elimination of protein immunogenicity. Thanks to these favorable properties, PEGylation now plays an important role in drug delivery, enhancing the potentials of peptides and proteins as therapeutic agents. That is why PEG polymers are very interesting as coating agents for biocompatible and pharmaceutical applications. PEGylation can bring to the NPs an immune "stealthiness" and thus prolong their circulation in blood by covering up their charges, increasing their hydrophilicity, and providing the required flexibility to cross the glomerular membrane [117]. The PEG_{5000} (average molar weight of 5000 g/mol) chains used in this study were methoxy- and thiol- terminated on the opposite sides (CH_3O-PEG-SH). The -SH group was intended to favor the PEG binding to the AuNF surface [88, 118]. The high molar weight of PEG is known to be favorable for the colloid stabilization via the steric hindrance mechanism [88] independently from the pH of the medium.

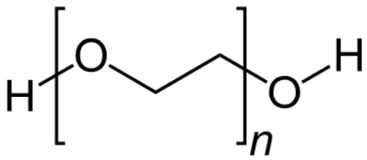

PEG

Figure 25. Chemical structure of PEG.

3.1.1. Effect of PEG on the chemical and colloidal stability of the AuNFs

The addition of the PEG just after the AuNF synthesis protects their color and LSPR band, until at least 27 days (see the UV-vis spectra in Figure 26.A). After 24 hours of incubation with the PEG, only a slight red-shift from 630 to 640 nm (+10 nm) (Figure 26.A) was induced by the adsorption of the PEG onto the AuNF surface and the intensity of the LSPR band decreased a little, from 1.5 to 1.4. Except for the range between 580 and 700 nm, the LSPR band shape of the PEGylated AuNFs follows that of the freshly generated surfactant-free AuNFs. Thus, neither degradation nor aggregation features were observed in the UV-vis spectra. Indeed, as explained above, the petal degradation leads to a blue-shift of the LSPR band which becomes narrower, while the particles aggregation leads to its spreading to the high wavelength region and a lowering of its intensity. Thus, the PEG was adsorbed at the AuNF surface and stabilized them both colloidally and chemically.

Table II. Table presenting the position of the main studied peaks on the SERS spectra in all the sections below within this chapter.

Peak	A	B	C	D	E
Raman shift ***(cm^{-1})***	600	1445	1500	1600	1660

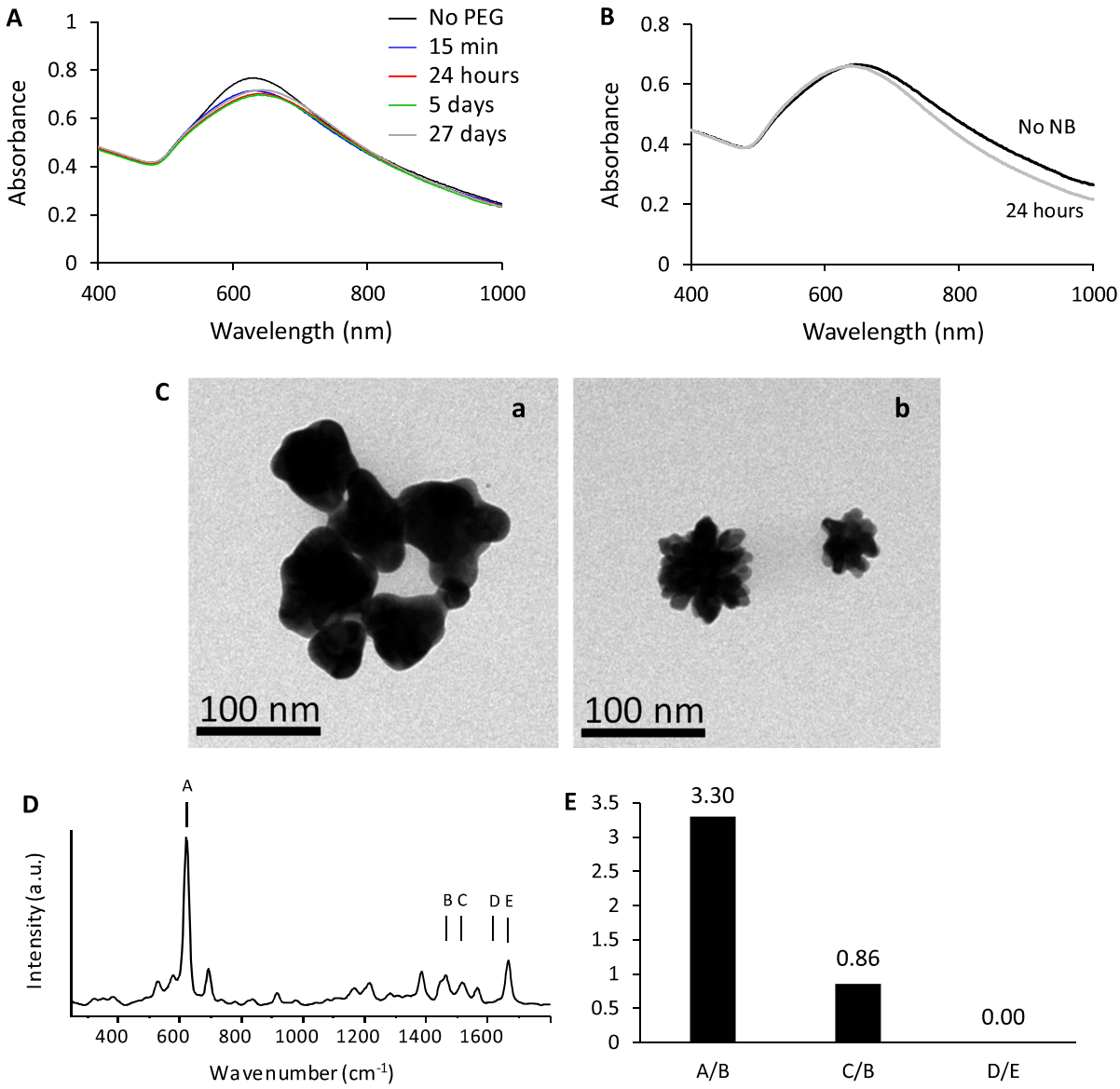

Figure 26. A: Effect of PEG on the LSPR band of the AuNFs. UV-visible spectra of AuNFs freshly synthesized (no PEG) or incubated for various time in presence of PEG at R2 = 10. The LSPR band position started from 630 nm (black and blue curves) then remained at 640 ± 2 nm from 24 hours of incubation. **B: Effect of the Nile blue (NB) on the LSPR band of the PEG-coated AuNFs.** UV-visible spectra of the PEG-coated AuNFs without NB (black) and incubated for 24 hours with 1 µmol/L of NB (grey). The spectra were normalized to the same absorbance at 400 nm, for easier comparison. **C: Effect of PEG on the AuNF morphology.** TEM images of the AuNFs 24 hours after synthesis, surfactant-free (a) and PEGylated (b). **D: Effect of PEG on the SERS spectra of NB,** at R2 = 10 (black spectrum) **E: Histogram representing the intensity ratio of the main SERS bands of NB** recorded with R2 = 10 (black bars). *NB: The ratio D/E was set to 0 since it was impossible to demarcate the base of a peak at the position D.*

The chemical stability of PEGylated AuNFs was confirmed with the TEM images (Figure 26.C) which shown that, similarly to PVP, PEG coating preserved the gold petals. After a

further 24 hours incubation of the AuNF@PEG suspension with 1 µmol/L NB, the LSPR band was slightly blue-shifted (-9 nm) and the higher wavelength part of the spectrum was slightly reduced (Figure 26.B). This observation is most probably due to the loss of a fraction of heaviest particles/aggregates which may settle down to the bottom of the vial, in spite of the presence of PEG.

3.1.2. Effect of PEG on the SERS activity of the AuNFs

A strong SERS signal of 1 µmol/L of NB was obtained on the PEGylated AuNFs (Figure 26.D and E). Surprisingly, the spectral shape (relative intensity of the peaks A, B, C, D, and E) corresponded to the "acid configuration" of NB (see the paper Pacaud et al. in the previous Chapter), while the pH of the suspension was measured to be 7.8. One could explain such an effect by the PEG shell - induced changes in the orientation of the NB molecules on the AuNF surface.

3.2. Coating the AuNFs with the Pluronics F68 & F127

Poloxamers are non-toxic blockcopolymers of ethylene oxide (EO) and propylene oxide (PO) blocks arranged in a triblock structure EO_x-PO_y-EO_z (Figure 27), soluble in aqueous media. The commercial purchased Pluronics F127 and F68 used in this study have a PO fraction of 70% and 80% and an average molar weight of 12,600 g/mol and 8,400 g/mol, respectively. Pluronics show thermoreversible properties which are of the utmost interest in optimizing drug formulation (fluid state at room temperature facilitating administration and gel state above sol-gel transition temperature at body temperature promoting prolonged release of pharmacological agents). Poloxamer 407 (Commercially named Pluronic F127) formulations lead to enhanced solubilisation of poorly water-soluble drugs and extend the release profile for many galenic applications [119, 120] (e.g., oral, rectal, topical, ophthalmic, nasal and injectable preparations) but do not clearly show any relevant advantages when used alone. Their combination with other excipients like Poloxamer 188 (Pluronic F68) promotes Poloxamer 407 action by optimizing its sol-gel transition temperature [121] or increasing its bioadhesive properties. New findings have also demonstrated immuno-modulation and cytotoxicity-promoting properties of Poloxamer 407 revealing significant pharmacological interests [122]. Their biocompatibility and thermosensitive behavior make the poloxamers interesting polymers for biocompatible nanoparticles coating.

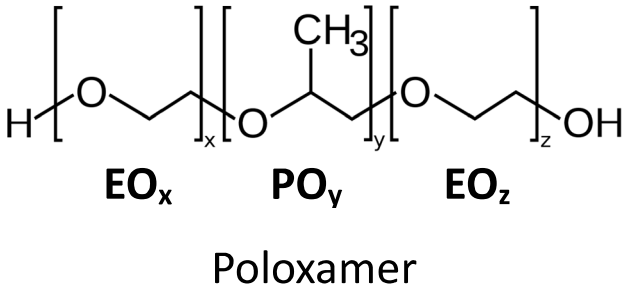

Figure 27. Chemical structure of a poloxamer composed of EO and PO arranged in a triblock structure.

3.2.1. Effect of Pluronics F68 and F127 on the chemical and colloidal stability of the AuNFs.

Compared to the freshly prepared surfactant-free AuNFs, those incubated for 24 hours in presence of Pluronics F68 have their LSPR band blue-shifted: -17 nm at R2 = 10 and -28 nm for R2 = 0.01 (Figure 28.A, left window). With Pluronics F127, the LSPR band remained nearly its previous position (-5 nm) at R2 = 10 and shifted of -19 nm at R2 = 0.1 (Figure 28.A, right window). Thus, the full protection against chemical degradation of the AuNFs (presumably via the oxidation of the petals) was only possible with Pluronics F127 at a higher concentration of the polymer. The protective role was only partial at lower R2 for the Pluronics F127 and even weaker at both R2 for the Pluronics F68. The spectra of the poloxamer-coated AuNFs remained narrow and did not increase in intensity at higher wavelengths and thus did not indicate any aggregation.

Both Pluronics F68 and F127 were able to ensure the protection of the AuNF colloids against aggregation upon the addition of the NB (1 µmol/L, 24h) at R2 = 10 (high concentration) but not at R2 = 0.01 (see the dashed lined in Figure 28.B). Here again, the effect was stronger with Pluronics F127 than with F68. It is worthy to note that at the same Polymer/Au w/w ratio, the molar concentration was lower for F127 (M_W = 12.6 kDa) than for F68 (M_W = 8.4 kDa). Thus, that is the composition and/or chain length of the poloxamers which plays a significant role in their ability to protect both the chemical and colloidal stability of the AuNFs. It is possible that it plays on the density of the polymeric layer at the surface of the AuNFs.

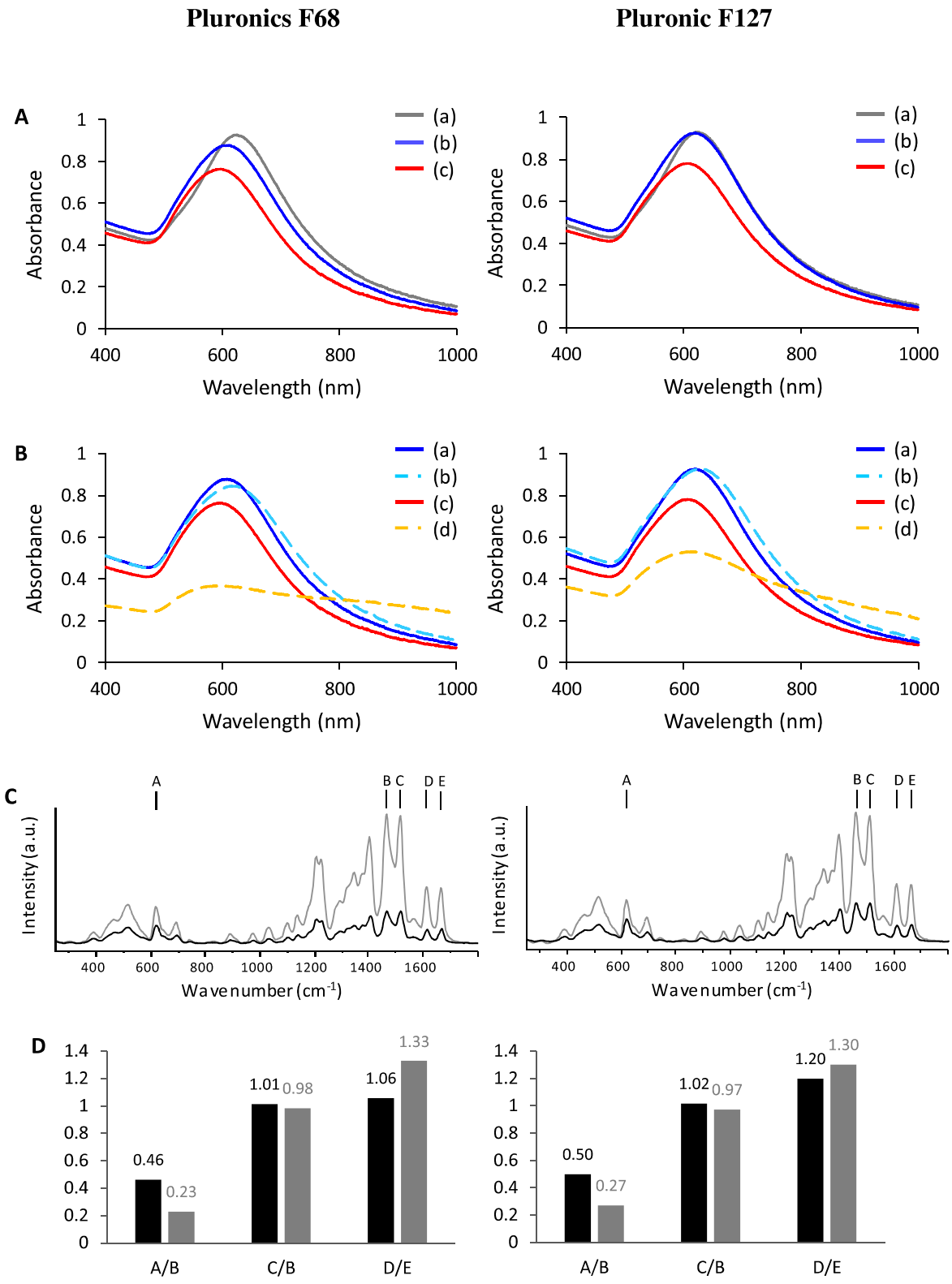

Figure 28. A: Effect of poloxamers on the LSPR band of the AuNFs. UV-visible spectra of AuNFs freshly synthesized (a) or incubated 24 hours in presence of poloxamers at a R2 = 10 (b) and R2 = 0.01 (c). The LSPR band positions represented by the grey (a), blue (b) and red (c) curves are respectively at 625, 608 and 597 nm for the Pluronics F68 and 625, 620 and 606 nm for the Pluronics F127. **B: Effect of the Nile blue (NB) on the LSPR band of the poloxamer-**

coated AuNFs. UV-visible spectra of the poloxamer-coated AuNFs R2 = 10 (a, b) and R2 = 0.01 (c, d), alone (solid lines a, c) or incubated with 1 µmol/L of NB (dashed lines b, d). **C: Effect of poloxamers on the SERS spectra of NB**, at R2 = 10 (black spectrum) or R2 = 0.01 (grey spectrum). **D: Histogram representing the intensity ratios of the main SERS bands of NB** recorded with R2 = 10 (black bars) or R2 = 0.01 (grey bars).

3.2.2. Effect of poloxamers on the SERS activity of the AuNFs

With both poloxamers, the increase of their concentration, i.e. of the R2 value from 0.01 to 10, led to about a 3.5-fold decrease of the total intensity of the NB SERS signal (Figure 28.C). At the same R2 = 10, the AuNFs coated with the pluronics F68 gave a stronger SERS signal of about 1.15-fold while at R2 = 0.01 it was about 1.30-fold than those coated with pluronics F127. However, these small intensity differences are not significative and we can conclude that in both cases the SERS signal delivered by both poloxamers are very close to each other in terms of total intensity. The intensity ratio of the main SERS bands has also shown some changes with the increase of the polymer concentration (Figure 28.D). At the same R2 value, F127 and F68 gave nearly the same spectral shape. Thus, the higher poloxamer concentration affected the NB molecules adsorption on the Au surface, both qualitatively and quantitatively. This slightly affects the SERS spectra of NB, while they remain very similar in shape and thus easily recognizable. At low polymer concentration, both the NB adsorption modality and the partial AuNF aggregation may participate to the increase of the intensity of the signal.

3.3. Coating the AuNFs with the alginates

Hydrosoluble polymers of alginates (Figure 29) are non-toxic natural polysaccharides of various molecular weight extracted from brown algae. They are composed of two monomers: mannuronates (M) and guluronates (G) which are combined sequences of M-M, G-G, and M-G [123]. The sequence presence, the overall M/G ratio and the chain length are defined by the natural factors affecting the algal growth (region and season of harvesting). Due to their flexible conformation and to their carboxyl groups (able to chelate divalent metal ions like calcium and to provide negative charges at neutral pH) alginates are interesting polymers for biocompatible nanoparticle coating [124], usually used in a form of sodium salts. The commercially purchased sodium alginates used in this study don't have a defined average molar weight.

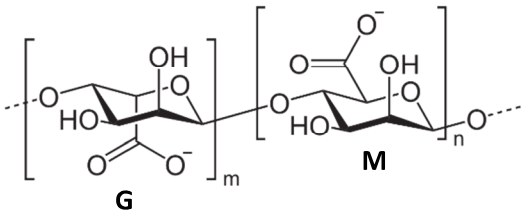

Figure 29. Chemical structure of alginate polymer composed of M and G monomers.

3.3.1. Effect of alginate on the chemical and colloidal stability of the AuNFs

After 24 hours of incubation of the surfactant-free AuNFs with the alginates at R2 = 10 the LSPR band underwent a red-shift of +7 nm (from 632 to 639 nm) (Figure 30.A), while at R2 = 0.01, it blue-shifted (-12 nm) (Figure 30.A). Thus, the AuNF chemical stabilization was complete at higher concentration of alginates while at lower R2 it was rather partial but still noticeable.

In presence of 1 µmol/L NB (for 24 hours), a partial AuNF aggregation (increased absorbance at the higher wavelengths) was observed at R2 = 0.01 while at R2 = 10 they were colloidally stable (Figure 30.B).

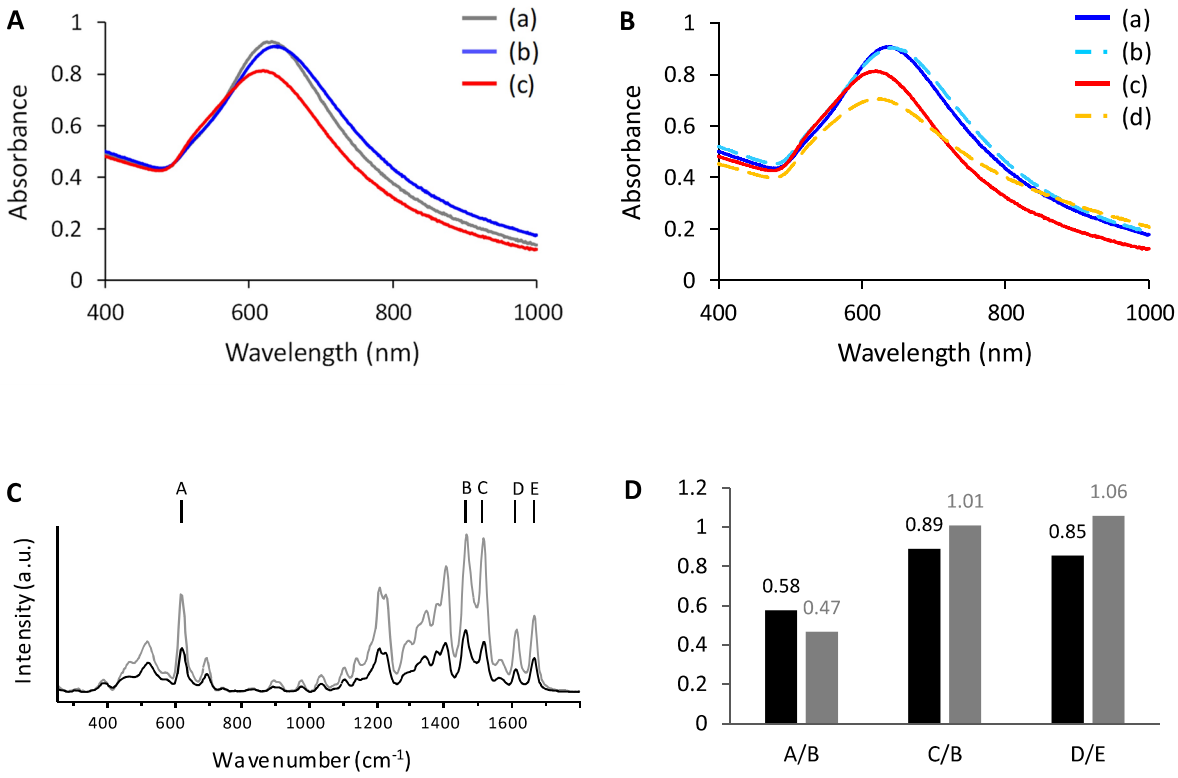

Figure 30. A: Effect of alginate on the LSPR band of the AuNFs. UV-visible spectra of AuNFs freshly synthesized (a) or incubated 24 hours in presence of alginate at a R2 = 10 (b) and R2 = 0.01 (c). The LSPR band positions represented by the grey (a), blue (b) and red (c) curves are respectively at 632, 639 and 620 nm. **B: Effect of the Nile blue on the LSPR band of the alginate-coated AuNFs**. UV-visible spectra of the alginate-coated AuNFs R2 = 10 (a, c) and R2 = 0.01 (b, d), alone (a, b) and incubated with 1 µmol/L of NB (c, d). **C: Effect of alginate on the SERS spectra of NB**, at R2 = 10 (black spectrum) or R2 = 0.01 (grey spectrum). **D: Histogram representing the intensity ratios of the main SERS bands of NB** recorded with R2 = 10 (black bars) or R2 = 0.01 (grey bars).

3.3.2. Effect of alginates on the SERS activity of the AuNFs

The SERS spectrum was nearly twice more intense at R2 = 0.01 than at R2 = 10 (Figure 30.C). This is similar to the effect of the other polymers described in this study. Ongoing from R2 = 0.01 to R2 = 10, the ratio of the intensity of the main SERS bands of NB has been slightly changed (Figure 30.D). They decreased from 1.01 to 0.89 for the C/B ratio, and from 1.06 to 0.85 for the D/E ratio; increased from 0.47 to 0.58 for the A/B ratio. These slight changes may indicate that the alginate shell is able to moderately modify the geometry of the NB adsorption on the gold surface of the AuNFs. This geometry may also affect the total intensity of the SERS spectrum at high R2.

3.4. Coating the AuNFs with the chitosan

Chitosan is an amino polysaccharide, derived as a deacetylated form of chitin which is produced by mollusks, crustaceans, insects, fungus, algae, and related organisms making it as the second prevalent form of polymerized carbon in nature [125]. Chitosan is made of a random distribution of D-glucosamine (deacetylated monomer) and residue of N-acetyl-D-glucosamine (acetylated monomer) [126]. Its non-toxic, biocompatible, antibacterial and biodegradable properties have led to significant research towards biomedical and pharmaceutical applications, such as drug delivery. The numerous primary amine groups in chitosan are mostly responsible for its various properties such as cationic nature, controlled drug release, antimicrobial, permeation enhancement or chelation properties making the chitosan an interesting functionalizing polymer for biocompatible nanoparticle coating [127]. The chitosan used within this study is 110,000 to 150,000 g/mol and was previously dissolved into a nitric acid (HNO_3) solution set to a pH of 5 to make a 1.0 g/L chitosan solution.

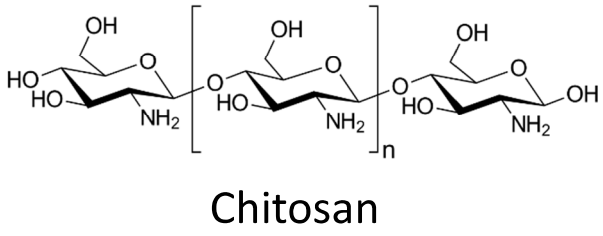

Chitosan

Figure 31. Chemical structure of chitosan.

3.4.1. Effect of chitosan on the chemical and colloidal stability of the AuNFs

After 24 hours of incubation of the AuNFs with the chitosan, the LSPR band was found red-shifted of +14 nm at R2 = 10 and of +6 nm at R2 = 0.01 (Figure 32.A). Thus, similarly to the other polymers studied here, chitosan also seems to protect the petals of the AuNFs from their degradation. However, at R2 = 10, but not at R2 = 0.01, the UV-vis spectra were enlarged to the higher wavelengths, indicating a partial aggregation of the AuNFs. Therefore, in contrast to the polymers described above, higher concentrations of chitosan led to a partial aggregation and not to the colloidal stability of the AuNFs.

Accordingly, it better protected the colloids from an NB-induced aggregation at a low concentration than at high R2 (Figure 32.B).

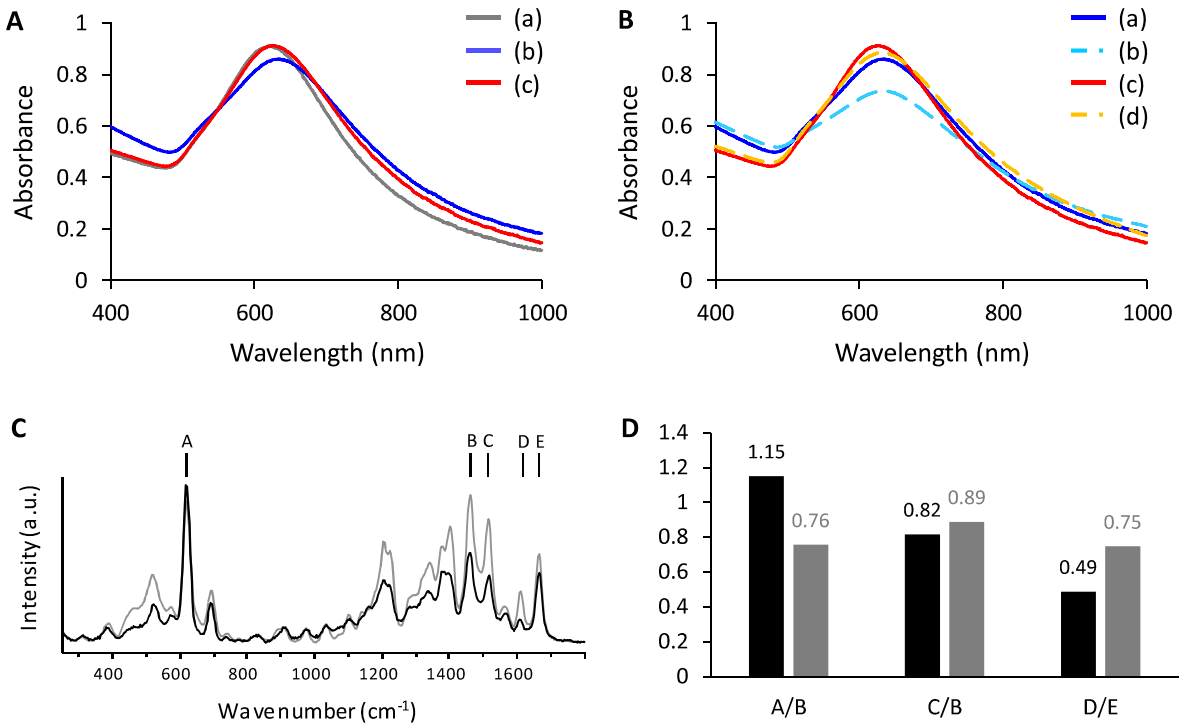

Figure 32. A: Effect of chitosan on the LSPR band of the AuNFs. UV-visible spectra of AuNFs freshly synthesized (a) or incubated 24 hours in presence of chitosan at a R2 = 10 (b) and R2 = 0.01 (c). The LSPR band positions represented by the grey (a), blue (b) and red (c) curves are respectively at 622, 636 and 628 nm. **B: Effect of the Nile blue on the LSPR band of the chitosan-coated AuNFs**. UV-visible spectra of the chitosan-coated AuNFs R2 = 10 (a, c) and R2 = 0.01 (b, d), alone (a, b) and incubated with 1 µmol/L of NB (c, d). **C: Effect of chitosan on the SERS spectra of NB**, at R2 = 10 (black spectrum) or R2 = 0.01 (grey spectrum). **D: Histogram representing intensity ratio of the main SERS bands of NB** recorded with R2 = 10 (black bars) or R2 = 0.01 (grey bars).

3.4.2. Effect of chitosan on the SERS activity of the AuNFs

Similarly to other polymers, the increase of the concentration of chitosan (from R2 = 10 to R2 = 0.01) leads to about a 29 % decrease of the total SERS intensity (Figure 32.C) and to changes of the relative intensity of the NB main SERS bands (Figure 32.C and D). This is in the agreement of the above-discussed role of the polymers in the NB adsorption and the AuNF aggregation state.

3.4.3. Effect of the pH (pH = 7 and pH = 5)

Since the pH affects both NB and chitosan properties, we studied the effect of the pH change between 5 and 7.

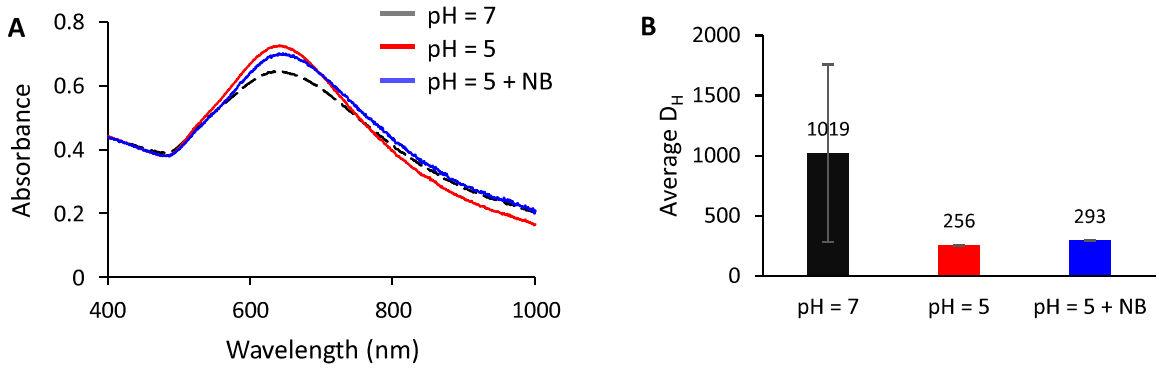

Figure 33. Effect of pH on the chitosan-coated AuNFs. A: UV-visible spectra of an aqueous suspension of AuNFs in presence of chitosan at R2 = 10 and at pH = 7 (dashed black curve), then readjusted to pH = 5 and sonicated for 1 hour (red curve), then incubated with 1 µmol/L of NB for 24 hours (blue curve). The spectra were normalized on the intensity of the black dashed curve at 400 nm, for easier comparison. B: DLS data on the z-average hydrodynamic diameter (D_H) of the respective colloids.

The chitosan being more stable in an acidic medium (pKa = 6.5 [127]), it has been tried to better disperse the NPs formed at pH = 7 by lowering the pH to 5 and sonicating them in an ultrasound bath. At the UV-visible absorption, the maximum absorption peak remained at the same position while the intensity at the higher wavelengths (light scattering contribution from bigger particles/aggregates) slightly diminished (Figure 33.A). Although this effect was weak in the UV-vis spectra, the DLS data showed that the presence of aggregates has diminished at pH = 5 (Figure 33.B). However, the addition of NB seems to slightly aggregates the AuNFs back (Figure 33.A).

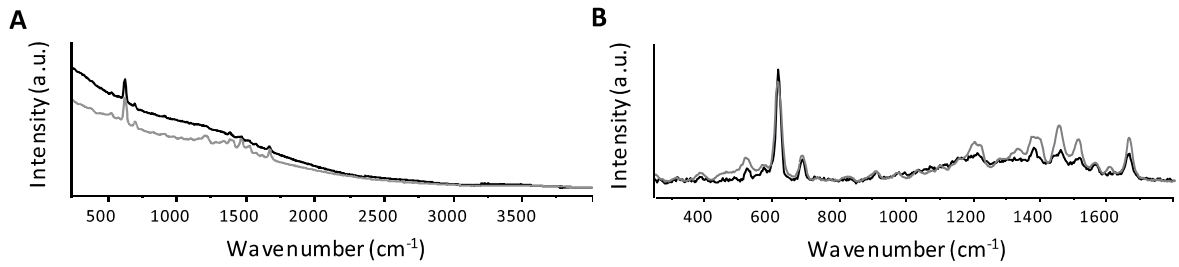

Figure 34. Effect of the pH on the SERS activity of NB at 1 µmol/L on the chitosan-coated AuNFs. A: SERS bands and fluorescence background of NB at pH = 7.0 (grey spectrum) and pH = 5.0 (black spectra). B: Zoom on the SERS bands after the fluorescence background subtraction. The spectra were normalized at the Raman band of water at 3400 cm^{-1}.

The chitosan-coated AuNFs gave less SERS signal and more fluorescence background at pH = 5 than at pH = 7 (Figure 34.A). Thus, the NB adsorption on the chitosan-coated gold surface was unfavored at acidic conditions, probably due to electrostatic repulsion of the positively charged aminated polymer and dye. As expected, (Pacaud et al. 2019, see the article in chapter III), the relative intensities between the SERS bands of NB were changed (Figure 34.B). On the other hand, these results demonstrate that aggregated AuNFs did not provide a stronger SERS intensity than when they are well dispersed.

3.5. Comparison of the effect between the different polymers on the SERS activity of the AuNFs

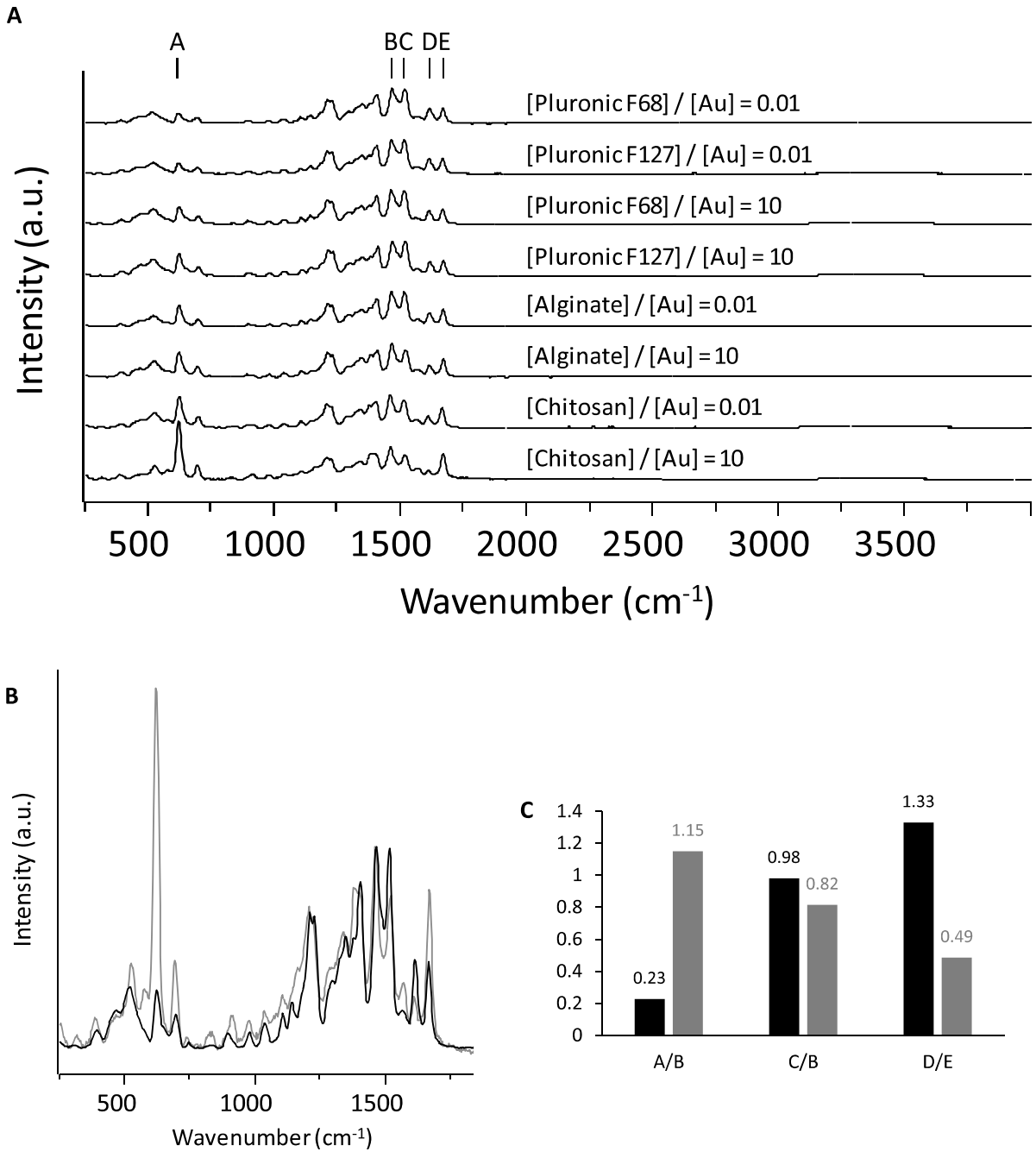

Figure 35. A: Comparison of the NB SERS spectral shape on the AuNFs coated with the different polymers. The spectra were normalized on the band B and above each curve its mass ratio is displayed. **B: The NB SERS spectra representing the two most distinct shapes observed in this study**, using respectively Pluronics F68 at R2 = 0.01 (black curve) and chitosan

at R2 = 10 (grey curve). **C: Histogram of the SERS bands intensity ratio from the spectra** shown in B with the corresponding colors.

The comparison of the SERS spectra given by the NB on the AuNF coated with the different polymers studied above (Figure 35.A) allows to notice that Pluronics and alginates favor more the typical SERS spectral shape given by NB in basic environments, while chitosan favors more the shape given in acidic environments. The most distinct spectral shape was observed between the chitosan at R2 = 10 and the Pluronics F68 at R2 = 0.01 (Figure 35.B).

4. Silica coating of the AuNFs

In contrast to the permeable shells of the polymers described above, there is also an interest to coat the AuNFs with a solid shell made of silica. In the case of a solid shell, the dye molecules (Raman reporters and/or fluorophores) may be encapsulated in the matrix of the shell, more or less far from the plasmonic surface. This provides two advantages: (i) the stability of their optical response and (ii) the possibility to combine the SERS and fluorescence responses from each nanoparticle.

In this section, the AuNFs were silica-coated in an aqueous medium, using a (3-Mercaptopropyl)trimethoxysilane (MPTES), a mercapto-organosilane, as the precursor. The effect of different parameters, such as the MPTES/Au molar ratio hereafter called R3, the presence of PVP and/or of NB have been studied on the silica shell formation. The shell thickness and its effect on the stability and SERS activity of the AuNFs (synthesized at R = 0.3, 20°C) have been studied using TEM, DLS, UV-vis and SERS spectroscopy.

4.1. Effect of silica shell on chemical and colloidal stability of the AuNFs

According to the TEM data shown in (Figure 36.A), the increased MPTES concentration from R3 = 0.1 to 10 led to the increase of the silica layer thickness. However, at R3 = 0.02 and 0.1, the silica layer is observable, but its thickness is difficult to measure with accuracy because it is too thin and of low electron density. It also worth to note that a TEM image is a 2D projection of the 3D shape of an AuNF. Thus, the measured silica layer thickness is dependent on the angle at which the petal is observed.

At R3 = 1 and 10, the average thickness of the silica layer was 6.38 ± 1.84 nm and 17.93 ± 2.59 nm, respectively. From the lowest R3, the silica shell was able to protect the AuNFs from the degradation of their petals. Accordingly, no blue-shift of the LSPR band has been observed (Figure 36.B). In contrast, the R3 increase led to a more important red-shift of the LSPR band position and of its width, while the shape remains symmetric, indicating that none uncontrolled aggregation occurred during the silica shell synthesis. As confirmation, no big aggregates were observed in the TEMs images. We think that the band enlargement is a consequence of the increased particle size and its wider distribution.

Interestingly, the LSPR band position increased linearly as a function of R3 (Figure 36.C). According to the literature, such shifts are expected since the silica shell leads to a local increase of the refractive index [64].

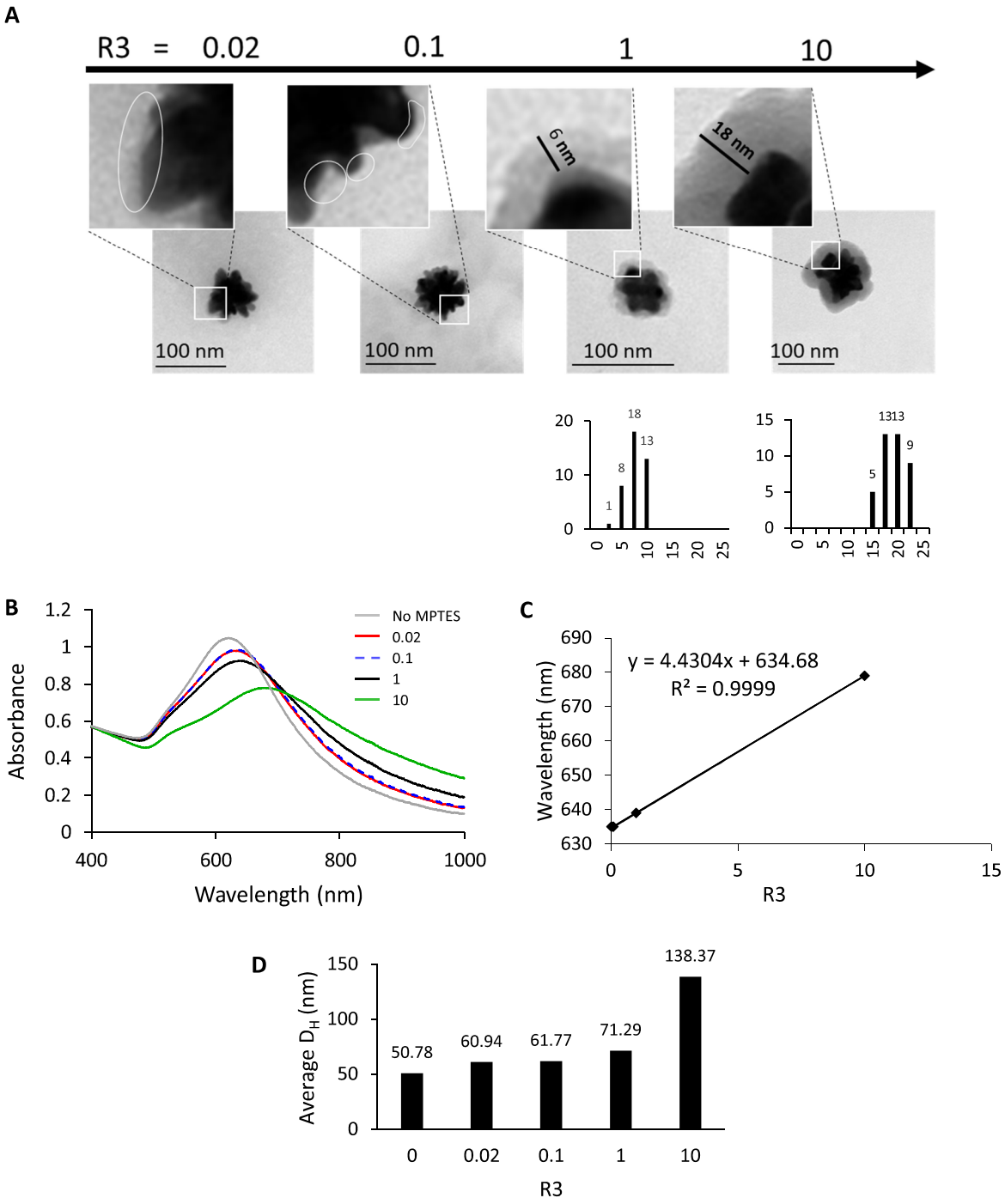

Figure 36. A: Typical TEM images of silica shell thickness on the AuNFs, as a function of R3 = 0.02, 0.1, 1, and 10. The insets show the shell thickness when it was measurable in the TEM images (10 NFs per batch, 4 measurements per NF). **B: LSPR band of the AuNFs freshly synthesized (grey) and silica-coated** at R3 = 0.02 (red), 0.1 (dashed blue), 1 (black) and 10 (green). For easier comparison, the spectra have been normalized to the same absorbance at 400

nm. **C and D: Diagrams representing respectively the evolution of the LSPR band maximum** (UV-vis data) and of the average hydrodynamic diameter (DLS data) as a function of R3.

4.2. Effect of the AuNF pre-coating with PVP on the silica shell

It has been proven previously [128] that PVP increases the affinity of TEOS over the gold spherical NPs. Thus, we also studied the silica shell formation on the AuNFs pre-incubated upon 24 hours with PVP. According to TEM images, at R3 = 1 and 10, the average thickness of the silica layer was nearly the same as without PVP and reached, respectively 4.02 ± 1.06 nm and 19.27 ± 2.72 nm (Figure 37.A). Indeed, the small difference observed in the presence or not of PVP is not significant, because the accuracy of the measurement of the silica layers thickness is limited, due to the 3D configuration of the petals of the AuNFs. Therefore, the PVP pre-coating was not able to affect the silica shell thickness.

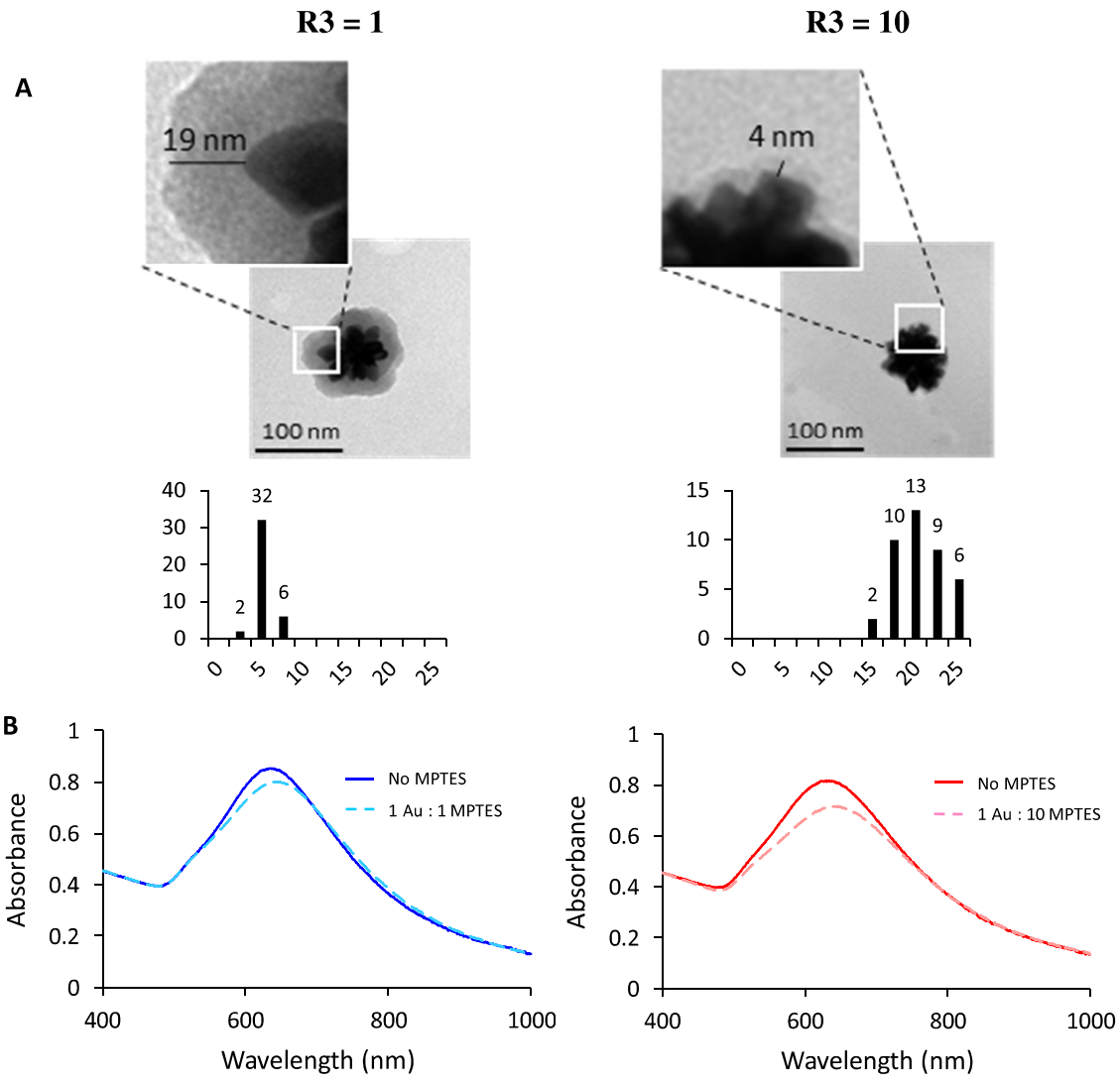

Figure 37. A: Typical TEM images of silica shell thickness on the AuNFs (pre-coated with PVP), as a function of R3 = 1 and 10. The insets show the shell thickness when it was measurable in the TEM images (10 NFs per batch, 4 measurements per NF). **B: LSPR band of the AuNFs freshly synthesized (solid curve) and silica-coated** (pre-coated with PVP) (dashed curve) at R3 = 1 (left) and R3 = 10 (right). For easier comparison, the spectra have been normalized to the same absorbance at 400 nm.

The LSPR band position and shape analysis in UV-vis spectroscopy (Figure 37.B) has shown that the AuNF pre-coated with PVP affects the colloidal characteristics only at R3 = 10: the band is less red-shifted (+17 instead of +58 nm) and is narrower with PVP than in absence of PVP. Thus, PVP prevents the AuNFs aggregation that could take place upon the silica shell formation at higher MPTES concentrations.

4.3. Encoding the silica-coated AuNFs with Nile blue

For SERS sensing applications, the encoding dye molecules have to be in the direct contact with or at few nanometers (< 2 nm) of distance from the gold surface. If the dye is fluorescent, the direct contact will favor the SERS while quenching the fluorescence. In contrast, if the dye molecules are at a few nanometers from the gold surface, the fluorescence is not quenched but can be enhanced together with the Raman scattering. Although the surface-enhanced fluorescence (SEF) corresponds to much lower enhancement factors (one order of magnitude) than those usually observed with SERS (5 to 9 orders of magnitude), it also has an analytical interest. If resonant excitation is used, the non-enhanced and enhanced fluorescence is observable as a background over which the SERS bands emerge more or less significantly. The ratio of SERS/fluorescence decreases with the increase of the NB molecules distance from the gold surface.

There are two ways to encode the AuNFs with the dye, either by including the dye before (*method 1*) or during (*method 2*) the shell formation or by incubating it with silica-coated AuNFs (*method 3*). The first way logically favors the direct contact with the gold surface (high SERS). The second way favors high fluorescence and allows SERS only at a short distance, either if the silica shell is thick enough or if it is permeable (porous).

4.3.1. Effect of the NB on the silica shell formation and on the LSPR bands

According to the TEM data (Figure 38.A), at R3 = 1, when the NB was introduced before (*method 1*) or simultaneously (*method 2*) with the silica precursor (MPTES), the silica shell was slightly thinner than for the NB-free AuNFs: the average thickness was ca. 4 nm instead of 6 nm. Compared to the freshly prepared AuNFs, those coated with silica have the LSPR band red-shifted, +10 or +18 nm in the presence (Figure 38.B) or absence of NB (Figure 36.B), respectively. At R3 = 10, the NB did not affect either the silica shell thickness or the LSPR band position. Thus, only at low R3, the presence of NB might slightly reduce the adsorption of the silica precursors on the gold surface. With both methods (*1* and *2*), three respective batches were generated and gave very similar UV-vis spectra (Figure 38.B). In terms of reproducibility, ease of processing and time saving, these methods seem relevant. It has to be noticed that the NB presence did not affect the LSPR band of the silica-coated AuNFs which were pre-treated with PVP before the MPTES addition (Figure 38.C). As expected, the NB addition to the silica-coated AuNFs (*method 3*) did not affect their LSPR bands (data not shown).

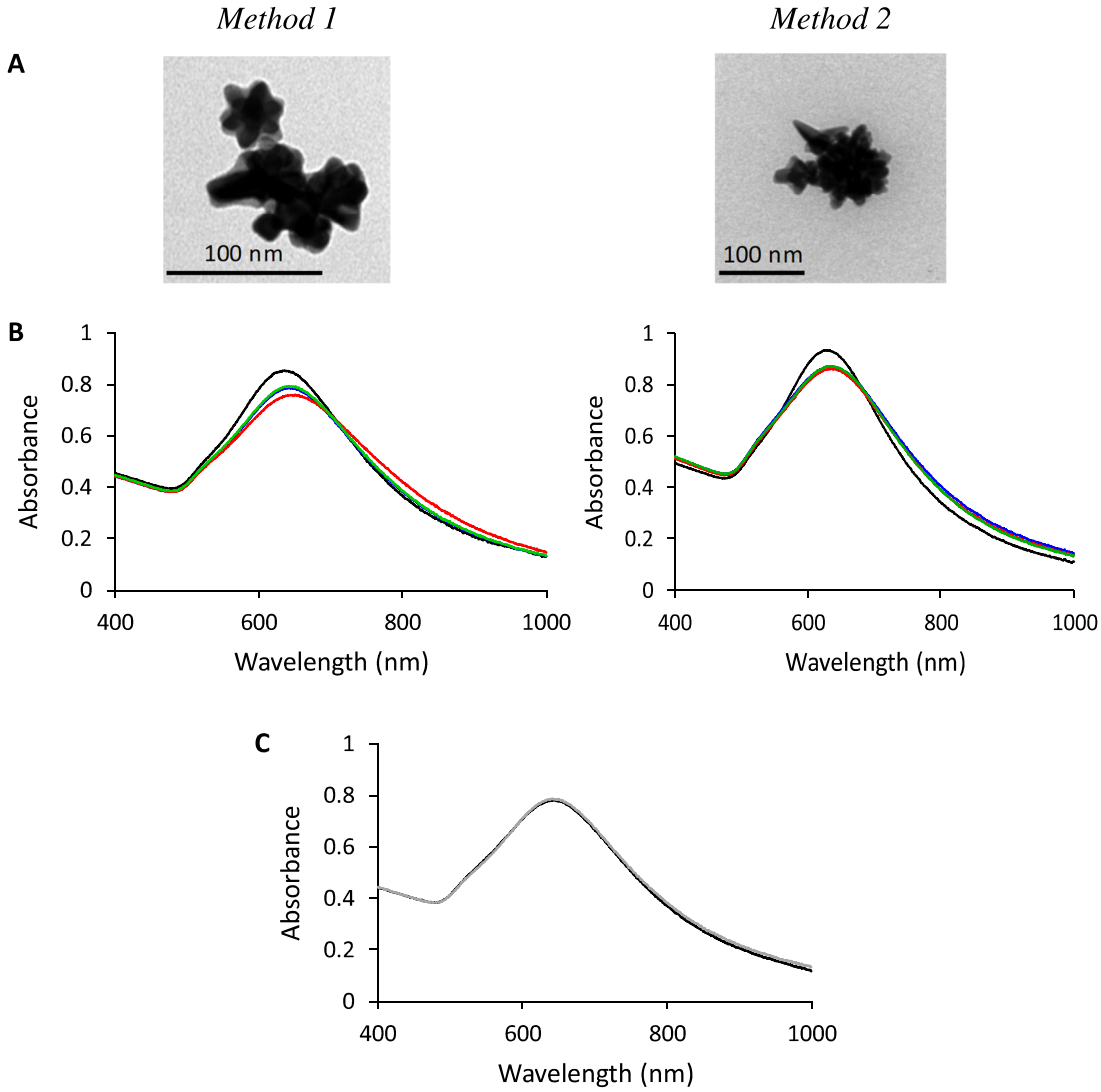

Figure 38. Influence of the NB addition modalities on the structure of the silica shell of the AuNFs (R3 = 1). A: TEM pictures of AuNFs coated with silica where: NB were incubated with PVP coated AuNFs for 24h, before the addition of MPTES (two-step *method 1*, left) or the 1 µmol/L NB was added simultaneously with MPTES to the surfactant-free AuNFs (one-step *method 2*, right). **B: LSPR bands of 3 reproduced batches** (red, green and blue curves) generated by *method 1* (left) or *method 2* (right) compared to those of freshly prepared AuNFs (black curves). **C: Comparison of silica-coated AuNFs prepared with and without NB** (grey and black curves respectively, in both cases the particles were pre-coated with PVP).

4.3.2. Effect of the NB inclusion method on the SERS activity of the silica-coated AuNFs

From the point of view of the SERS activity, the strongest signal was obtained with *method 2* (Figure 39.A) which confirms that including simultaneously the dye and the MPTES remains the best method of introducing the NB within the silica shell for a SERS effect purpose.

It seems that this protocol corresponds to less competition for the NB to reach the gold surface. On the other hand, *method 1* gave also a good intensity of the SERS bands, but a bit lower. Therefore, the PVP presence may result in lower NB adsorption on the gold with this method. With *method 3*, the thin silica shell did not prevent to observe the NB SERS bands, however, they were smaller than the one observed through *methods 1* and *2* and were put on a strong fluorescence background (Figure 39.C). It is important to notice that almost no fluorescence has been observed with *methods 1* and *2*. The shape of the NB SERS spectra on the silica-coated AuNFs was very similar to the one usually observed in acidic media and changes very little between the protocols: the A/B ratio for *method 1* and D/E ratio for *method 3* (Figure 39.B).

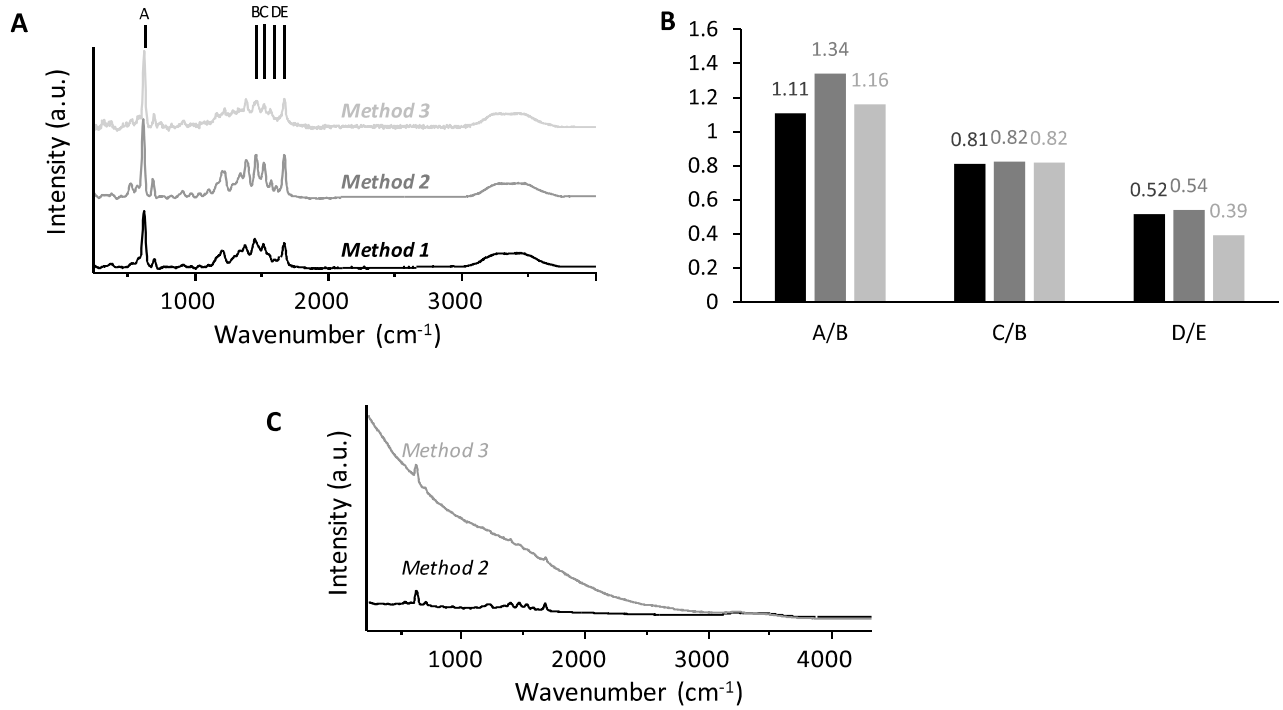

Figure 39. Influence of the NB addition modalities on the SERS/fluorescence activity of silica-coated AuNFs (R3 = 1)**. A: SERS spectra** when 1 µmol/L NB was added before (*method 2*, black curve), during (*method 1* dark grey curve) and after (*method 3*, light grey curve) the MPTES. The spectra were normalized on the water band and offset for comparison. **B: Intensity ratio of main SERS bands of NB**. The colors are the same as for A. **C: SERS and fluorescence signal**s of the NB added during (*method 1*, low fluorescence) or after (*method 3*, high fluorescence) the silica shell formation.

DISCUSSION GÉNÉRALE *(French version)*

English version of the discussion, conclusion, and perspectives are down below after the french version of the perspectives (p. 112).

L'effet SERS permet d'amener la spectroscopie Raman à l'échelle nanométrique et même moléculaire, jusqu'à la détection d'une molécule unique. La spectroscopie SERS est ainsi très intéressante pour la bioanalyse. Étant donné que l'effet SERS dépend directement des propriétés et des limites du substrat SERS, il est crucial, pour développer la spectroscopie SERS, d'améliorer et d'optimiser des substrats SERS en priorité. Le développement de substrats actifs en SERS fiables et efficaces passe par l'amélioration de leurs protocoles de synthèse (pour pouvoir adapter leurs propriétés en fonction des applications visées) et de leur mise en œuvre (pour pouvoir bénéficier pleinement de leurs propriétés).

On trouve déjà dans la littérature de nombreux types de nanoobjets actifs dans le SERS, avec plusieurs protocoles de synthèse différents pour chacun d'entre eux [18, 20, 26, 32, 72, 112, 129–133]. Toutefois, il reste nécessaire d'optimiser ces protocoles de synthèse, notamment pour améliorer leur biocompatibilité et leur stabilité dans un environnement approprié d'une part et d'autre part, pour les produire à une échelle plus large, voir industrielle. Cette thèse de doctorat est donc consacrée à l'étude de nouveaux substrats SERS sous forme de nanofleurs d'or.

1. Un nouveau protocole de synthèse de substrats SERS respectant les contraintes bionanalytiques

Parmi tous les substrats SERS potentiels existant dans la littérature, notre choix s'est porté sur le design des AuNFs car : (i) ils présentent des propriétés biocompatibles intéressantes, grâce à l'or qui possède une inertie chimique importante ; (ii) la position de leur bande plasmonique peut être ajustée dans la région du rouge - rouge lointain au proche IR et couvre ainsi une partie de la fenêtre optique des tissus biologiques. De plus, la forme anisotrope

particulière des AuNFs induit une forte augmentation du champ électromagnétique, aux jonctions entre leurs pétales (appelés « points chauds ») et aussi à leurs extrémités, par l'effet de pointe [31]. De plus, la forme anisotrope des AuNFs offre une grande surface qui permet une grande capacité de charge des molécules par particule [67].

Malheureusement, à ce jour, nous n'avons pas trouvé dans la littérature de protocoles vraiment adaptés aux besoins décrits ci-dessus. Un nouveau protocole a donc été développé au laboratoire, afin de respecter les contraintes bioanalytiques, à savoir réaliser les synthèses en milieu aqueux en utilisant uniquement des réactifs connus et peu ou pas toxiques. Le protocole souhaité devait être simple et rapide à mettre en place et éviter l'utilisation de solvants organiques, de polymères, de surfactants, ou d'autres métaux que l'or, pour générer des substrats SERS biocompatibles non toxiques, utilisables dans un environnement physiologique. Le réglage précis de la position de la bande LSPR sur une source laser commune, émettant dans la région spectrale du rouge - proche IR, était un critère important. La surface sans tensioactif est destinée à permettre l'adsorption sans encombre d'une large gamme de molécules. Néanmoins, nous avons aussi étudié les AuNFs habillées soit de polymères biocompatibles bien connus, soit d'une couche de silice, plus rigide.

Le protocole décrit dans **l'article du 1er chapitre** permet de synthétiser les AuNFs malgré l'absence de surfactant ou d'ions métalliques comme l'argent parmi les réactifs. Bien que des ingrédients « classiques » aient été utilisés, à notre connaissance, personne n'a fait état d'une synthèse similaire produisant des AuNFs. Malgré des températures de synthèse basses (température ambiante, comme dans l'article du chapitre III, ou entre 0°C et 1°C comme dans le chapitre IV de cette thèse), elles sont générées en quelques secondes seulement.

2. Capacité de ce protocole à ajuster la position de la bande plasmonique à la longueur d'onde souhaitée

La position de la bande LSPR fournie par les AuNFs est bien contrôlée et reproductible d'un lot à l'autre, ce qui signifie que la taille et la forme de nos nanoobjets sont également bien reproduites. Il est possible d'ajuster facilement la position de la bande LSPR des AuNFs, soit en modifiant le rapport molaire de seulement deux des réactifs utilisé NH_2OH/NaOH (entraînant des modifications du pH), soit, sans modifier le pH, simplement en ajustant la température de synthèse. Ces deux paramètres jouent un rôle critique dans la cinétique de la réaction et affectent donc la structure et les propriétés de la nanofleur produite. De plus, deux

lots différents avec leurs bandes LSPR à la même position ne présenteront pas forcément la même taille de nanofleur ou une morphologie similaire de leurs pétales selon le paramètre modifié (température ou pH). A plus basse température de synthèse, les AuNFs ont une forme de pétales plutôt rhombique alors qu'à plus haute température, leur forme s'apparente davantage à des tiges plus fines. Néanmoins, les nanofleurs d'or présentent également quelques faiblesses.

3. Les faiblesses et limites des nanofleurs d'or

Les nanopétales d'or sont si minces qu'elles se dégradent facilement sans protection. L'or massif est connu pour sa forte inertie chimique. Cependant, à l'échelle nanométrique, le nombre d'atomes de surface des NPs est plus élevé que le nombre d'atomes de volume. Ainsi, les atomes de surface qui manquent de liaisons de coordination avec leurs voisins, sont moins stabilisés par les charges libres présentes à la surface de la NP métallique. A l'échelle nanométrique, cette augmentation de la réactivité des atomes de surface peut déclencher l'oxydation des fines pétales par l'oxygène présent dans le milieu. Nous avons essayé de ralentir la dégradation des pétales en augmentant le pH après synthèse mais malgré l'influence du pH sur la cinétique de réduction, aucun changement significatif n'a eu lieu sur la vitesse de dégradation des pétales.

Une autre faiblesse vient aussi de leur structure anisotrope complexe. Par rapport aux nanosphères d'or conventionnelles (de diamètre d'environ 20 nm), les AuNFs sont plusieurs fois plus grandes et plus lourdes. Elles sont donc davantage sujettes à la sédimentation et leur structure anisotrope favorise leur imbrication avec leurs voisines en diminuant leur capacité de redispersion. Ainsi, les suspensions colloïdales de nanofleurs d'or sont intrinsèquement moins stables dans le temps que celles de nanopaticules d'or sphériques. Malgré cela, la stabilité colloïdale ainsi que la stabilité des pétales des NPs, dépend principalement de leurs propriétés de surface et de leur interaction avec leur environnement. Il est donc possible de protéger leur structure en modifiant leurs propriétés de surface par leur habillage.

4. Amélioration de la stabilité et fonctionnalisation des AuNFs par habillage

Les AuNFs peuvent être recouvertes d'une enveloppe de polymères, souple et perméable aux ions et aux molécules d'eau, de colorants ou de médicaments. Synthétisées par le protocole développé au laboratoire, nos nanofleurs d'or ont montré une bonne affinité avec tous les

polymères que nous avons essayé d'adsorber sur elles, malgré les différents types d'interactions que chacun de ces polymères peut avoir avec la surface des AuNFs. Le PEG-SH se coordonne certainement sur la surface par l'intermédiaire de son groupe thiol puis sa chaîne polyéther renforce probablement son adsorption par des interactions de type van der Waals avec la surface de la NP [88, 118]. La PVP et les poloxamères n'ayant pas de charge ni de groupes fonctionnels à forte affinité avec l'or comme le thiol, doivent principalement leur adsorption à des interactions de van der Waals induites par les nombreux atomes d'oxygènes (et aussi d'azote dans le cas de la PVP), de leur longues chaînes, plus électronégatifs et électrophiles [128, 134]. Les alginates pourraient se chélater sur la surface nucléophile des AuNFs par leurs groupes carboxyles (en compétition avec les citrates) alors que le reste de leurs chaînes montrent certainement aussi des interactions de van der Waals avec la surface. Le chitosane s'adsorbe probablement par les interactions de van der Waals, mais ses groupes amines cationiques interagissant avec les citrates sont capables de perturber le revêtement protecteur du citrate et d'induire une agrégation des NPs à des concentrations plus élevées (rapport massique polymère:or de 10:1). Par conséquent, le chitosane est le seul polymère étudié ici pour lequel la concentration élevée a diminué et non pas augmenté la stabilité colloïdale des AuNFs. A noter qu'à pH acide les NPs habillées de chitosane demeurent stables en suspension plus longtemps certainement dû à davantage de charges positives présentes grâce aux groupes amines protonées du polymère. En revanche, pour les polymères étudiés aux concentrations les plus faibles (rapport massique de polymère:or de 1:100), la protection de la stabilité colloïdale était insuffisante, notamment devant la capacité du NB à agréger les AuNFs. Il est intéressant de noter que dans notre étude, les AuNFs enrobées n'ont pas été lavées après incubation avec les polymères, sauf pour le PEG-SH et la PVP. Ainsi, des polymères libres présents dans la solution, surtout au rapport massique polymère : or le plus élevé, pouvaient participer au maintien ou à la perturbation de la stabilité colloïdale par des échanges (adsorption/désorption) avec la surface des NPs.

Pour les AuNFs habillées de PEG-SH et de PVP, les bandes LSPR n'ont pas été modifiées après avoir été lavées deux fois par centrifugation et remises en suspension dans de l'eau ultra pure, ce qui indique qu'une quantité significative de ces polymères est restée adsorbée sur la surface des NPs. Dans les deux cas, la stabilisation des colloïdes était très probablement due à l'entrave stérique des chaînes de polymères des NP voisines qui se déplaçaient et glissaient les unes sur les autres, empêchant ainsi leur agrégation. Dans le cas des AuNFs habillées de chitosane et d'alginate, on peut penser que la stabilité colloïdale a également été apportée par la

présence de charges positives ou négatives, respectivement. Ceci a été confirmé par le fait que les AuNFs incubées dans le chitosane étaient plus stables à pH = 5 qu'à pH = 7.

Contrairement à l'amélioration de la stabilité colloïdale des AuNFs, l'habillage par des polymères a pu affecter l'adsorption de la molécule d'analyte/marqueur sur la surface de l'or, tant sur le plan qualitatif (géométrie d'adsorption : orientation favorisée de la molécule adsorbée par rapport à la surface) que quantitatif (efficacité d'adsorption). Comme le SERS est un effet à courte portée (le signal est le meilleur lorsque l'analyte/marqueur se trouve à moins de 2 nm de la surface de l'or), la modalité d'adsorption affecte le signal SERS, tant sur le plan qualitatif (intensité relative des bandes principales) que quantitatif (intensité globale du signal SERS). Il est donc important de bien choisir le bon polymère, capable d'assurer la stabilité colloïdale et la biocompatibilité tout en préservant l'activité SERS.

Il a également été possible d'habiller nos AuNFs d'une couche de silice, plus rigide et moins poreuse que dans le cas de la couche de polymères décrite ci-dessus, mais permettant un bon contrôle de son épaisseur. La particularité du protocole que nous avons utilisé est que, contrairement au protocole sol-gel standard [135, 136], les synthèses sont réalisées dans un milieu sans alcool 100% aqueux (adapté de [137]). C'est un grand avantage de pouvoir synthétiser la couche de silice directement dans la même suspension que les AuNFs fraîchement synthétisées sans avoir besoin d'étapes intermédiaires de lavage ou de transfert de phase qui souvent induisent au moins l'agrégation partielle des colloïdes. Ainsi, l'utilisation du MPTES préalablement hydrolysé a donné de très bons résultats. La coquille de silice s'est développée de façon plutôt homogène autour des AuNFs. Même à la plus faible concentration essayée (MPTES/Au = 0.02), lorsque la couche de silice était difficile à identifier sur les images TEM, son effet protecteur, contre la dégradation et l'agrégation des AuNFs, indique bel et bien sa présence. Les protocoles ont donné une très bonne reproductibilité entre les lots (trois lots pour chaque concentration de MPTES) et pour tous les lots, nous n'avons pas observé de NP de silice blanche, sans nanoparticule d'or à l'intérieur. En revanche, l'habillage des AuNFs avec de la PVP (nécessaire dans les protocoles sol-gel standard [135]) n'a pas amélioré la formation de la couche de silice, mais au contraire a conduit à l'apparition d'un grand nombre de nanoparticules de silice indépendantes observées sur les images de MET. En comparaison avec la méthode sol-gel standard, qui fonctionne bien avec les nanosphères d'or et que nous avons d'abord essayé d'appliquer à nos AuNFs, à un rapport molaire MPTES/Au = 1, seules quelques AuNFs étaient complétement encapsulées dans une épaisse couche de silice, donnant des objets de 2 à 3 fois

plus large que les AuNFs, ou partiellement enrobées, préférentiellement à l'extrémité de leurs pétales - l'habillage était donc inhomogène - et un grand nombre de grosses NPs de silice indépendantes étaient produites (de 100 à 300 nm).

Shah et coll. [137] ont montré que la variation du temps d'incubation permet d'ajuster l'épaisseur de la couche de silice sur leurs nanosphères d'or mais, pour nos AuNFs, nous l'avons ajustée en variant leur concentration initiale en MPTES sans modifier le temps d'incubation entre les lots (12 heures). Nous avons ainsi produit des AuNFs revêtus d'une couche de silice allant jusqu'à 19 nm d'épaisseur, avec un potentiel zêta négatif de -50 mV et colloïdalement stables en solution aqueuse. Par conséquent, en plus des avantages décrits précédemment, ce protocole semble être plutôt flexible.

Le réglage de l'épaisseur de la couche de silice des AuNFs permet de combiner SERS, SEF (comme *surface-enhanced fluorescence* ou fluorescence exaltée de surface en français) et fluorescence classique (non-exaltée) au sein d'une même nanosonde, ce qui en fait une sonde multimodale. En effet, les molécules de colorant qui sont les plus proches (< 2 nm) de la surface de la nanoparticule d'or fournissent le signal SERS, tandis que les molécules plus éloignées de la surface de l'or seront plus actives en fluorescence. L'effet SEF est dominant jusqu'à environ 10 nm et la fluorescence classique à partir de 10 nm et au-delà. La réponse multimodale des AuNFs enrobées d'une coquille de silice est très prometteuse pour leurs applications en biodétection et en imagerie [57].

CONCLUSION GÉNÉRALE *(French version)*

Pour exploiter pleinement le potentiel de l'effet SERS, des difficultés pratiques et techniques doivent être surmontées, principalement en ce qui concerne la synthèse et la mise en œuvre des substrats plasmoniques. Dans le cadre de cette thèse, un protocole simple, fiable, en une seule étape et répondant aux contraintes bioanalytiques a été développé pour synthétiser des suspensions aqueuses de nanofleurs d'or présentant une surface libre d'interagir avec son environnement et à priori capable d'adsorber une grande variété de produits (analytes). Ainsi, ces AuNFs ont été stabilisés en les habillant de silice ou de polymères biocompatibles. Un signal SERS puissant (exc. laser 690 nm) a été obtenu avec des suspensions de AuNFs en présence de fluorophores le Bleu de nil ou le Cristal violet, à des concentrations de colorant micromolaires et sub-micromolaires, sans qu'il ne soit nécessaire d'agréger les AuNFs entre elles. De plus, leur enrobage dans une coquille de silice a permis de générer simultanément du SERS et de la fluorescence, leur conférant une modalité supplémentaire. Compte tenu des propriétés observées, ces nanosystèmes semblent très prometteurs comme substrats pour la spectroscopie, la détection, et l'imagerie SERS, ainsi que pour un large éventail d'autres applications bioanalytiques.

PERSPECTIVES *(French version)*

La polyvalence et l'affinité apparente qu'ont nos AuNFs avec une large gamme de composés différents, leur permet d'être utilisées dans de nombreux domaines d'application.

1. Imagerie bioanalytique et nanovectorisation de médicaments

Bien que nous ayons développé ces NPs afin de concevoir des nanosondes SERS polyvalentes et stables, elles peuvent également être utilisées en dehors de ce cadre. L'article de S. Ben Djemaa et coll. (Annexe 1) montre un autre aspect de l'utilisation possible de nos AuNFs comme nanovecteurs (de médicaments par exemple) et nanosondes multimodales. Grâce à l'ajustement d'un microscope confocal à balayage laser non spectral (LSCM) pour co-détecter la double réponse optique des AuNFs : diffusion élastique de la lumière (renforcée par les plasmons) et fluorescence (du Bleu du nil porté à la surface des AuNFs), on a pu observer que les molécules du Bleu du nil étaient désorbées des AuNFs et diffusaient à travers la membrane cellulaire dans les cellules, tandis que les AuNFs étaient fixés sur cette membrane. Ainsi, associés à des approches analytiques innovantes basées sur le LSCM, nos AuNFs peuvent contribuer à une compréhension des interactions intracellulaire des nanovecteurs et de leur cargo. Par conséquent, leurs diverses propriétés intrinsèques augmentent leurs domaines d'application même en dehors du champ d'application pour lequel elles ont été conçus à l'origine.

2. Les AuNFs comme base de nanosondes multimodales magneto-plasmoniques

Les avantages de nos AuNFs évoqués ci-dessus en font de bons candidats pour la conception de nanosystèmes multimodaux plus complexes associant plusieurs matériaux de propriétés différentes. Par exemple, afin d'enrichir le potentiel des AuNFs en tant que nanosondes multimodales, elles peuvent être associées à des nanoparticules superparamagnétiques d'oxyde de fer (SPIONs comme *Superparamagnetic iron oxide nanoparticles*). Les SPIONs sont utiles comme agents d'imagerie IRM (imagerie par résonance

magnétique) et comme substrat magnétique permettant de diriger les nanosondes magneto-plasmoniques vers la zone à analyser. De nombreuses publications ont fait état de l'association de l'or et des oxydes de fer à l'échelle nanométrique, à la recherche d'une nanosonde multimodale fiable [32, 65, 66, 138–144].

Cependant, les difficultés rencontrées pour reproduire leurs protocoles, la faible recherche sur la stabilité colloïdale des suspensions synthétisées et la complexité ou la toxicité potentielle finale des suspensions générées par ces protocoles montrent que du travail d'optimisation reste à faire dans ce domaine. Dans le cadre de cette thèse de doctorat, une telle combinaison a également été tentée, dans différentes configurations (cœur-coquille, nano-verbe hybride, etc…) et selon différents protocoles, basés sur la synthèse in situ ou l'assemblage post-synthèse [19, 20, 32, 57, 59, 65, 66, 136, 143, 145–147].

Par exemple, des AuNFs multimétalliques ont été synthétisées à partir de suspensions aqueuses de SPIONs (données non montrées). Les AuNFs résultantes semblaient entourées de SPIONs, comme on l'a vu dans nos images de MET. Elles ont leur bande LSPR décalée dans le rouge et élargie, mais elles sont restées stables pendant des jours. Cela signifie que les SPIONs stabilisent les pétales en surface des AuNFs mais permettent tout de même une agrégation limitée des AuNFs. Ainsi, après une optimisation de l'épaisseur de la couche de SPIONs, l'assemblage AuNF@SPION pourrait être encapsulé à l'intérieur d'une couche de silice conduisant à des nanosondes magnéto-plasmoniques et élargissant ainsi encore davantage leur champ d'application [142].

GENERAL DISCUSSION *(English version)*

The SERS effect allows to bring the Raman spectroscopy at the nanometric and even at the single molecular scale. This makes SERS spectroscopy very attractive for bioanalysis. Since the SERS effect directly relies on the SERS substrate properties and limitations, in order to develop the SERS spectroscopy, it is crucial to focus on the improvement and the optimization of SERS substrates. The development of reliable and effective SERS active substrates includes the improvement of their protocols of synthesis (to be able to tune their properties according to the applications aimed) and their methods of application (to be able to take a full benefit of their properties).

Numerous types of SERS-active nano-objects can already be found in literature, with several different protocols of synthesis for each of them [18, 20, 26, 32, 72, 112, 129–132]. However, there is still a need to improve the efficiency of their protocols of synthesis, in particular, to improve their biocompatibility and stability in an appropriate environment on the one hand and on the other hand to produce them at a larger scale, maybe industrial. This Ph.D. thesis is thus devoted to a study of the new SERS substrates in the form of AuNFs.

1. A new synthesis protocol of SERS substrate respecting bioanalytical constraints

Among all the potential SERS substrates existing in the literature our choice was made on the AuNF design because: (i) they show interesting biocompatible properties since gold has an important chemical inertness; (ii) their LSPR band can be tuned within the red - deep red to VNIR region and thus covers a part of the biological tissue optical window. In addition, the particular anisotropic shape of the AuNFs induces strong enhancement of the electromagnetic field between their petals (hot spots) and also at their tips (lightning rod effect) [31]. Furthermore, the anisotropic shape of the AuNFs provides a large surface area which allows a higher drug loading capacity for each NP. [67].

Unfortunately, to date, we didn't find in the literature protocols fully adapted to the needs described above. Therefore, a new protocol was developed in the lab, in order to respect a list of bioanalytical constraints namely, making the synthesis in an aqueous medium using only

well-known reagents of low/none toxicity. This protocol should be facile and rapid to set up and avoid the use of organic solvents, polymers, surfactants, or other metal than gold, to generate non-toxic biocompatible SERS substrates, useable within a physiological environment. The accurate tuning of the position of the LSPR band to one of the common red-NIR laser sources was an important criterion. The surfactant-free surface is intended to allow the seamless adsorption of a wide range of molecules. Nonetheless, we studied also the AuNFs coated with either a list of well-known biocompatible polymers or with a more rigid silica shell.

The protocol described in the **article of the 1st chapter** allows synthesizing AuNFs despite the absence of surfactant or metal ions such as silver among the reagents. Although non-exotic ingredients were used, to the best of our knowledge, no-one reported a similar AuNFs synthesis. Despite low synthesis temperatures (ambient temperature, as in chapter III, or between 0°C and 1°C, as in chapter IV) they are made within a couple of seconds only.

2. Tunability of the LSPR band characteristics brought by this protocol

The position of the LSPR band provided by the AuNFs is well controlled and well reproducible from a batch to another, meaning that the size and shapes of our nano-objects are also well reproduced. It is possible to tune the position of the LSPR band of the AuNFs easily, by either changing the molar ratio of only two of the reagents NH_2OH/NaOH (leading to some changes in the pH) or, within the same pH, by adjusting the synthesis temperature. These two parameters play a critical role in the kinetics of the reaction and thus affect the structure and the properties of the final AuNF produced. Furthermore, two different batches showing the same LSPR band position won't have necessarily the same AuNF size or petal shape depending on which parameter is changed (temperature or pH) to shift the plasmonic band. At a lower temperature of synthesis, the AuNFs have rather rhombus petal shapes while at higher temperature their shape is more rod-like. Nevertheless, AuNFs also present some weaknesses.

3. Weaknesses and limitations of the AuNFs

The gold nanopetals are so thin that they are easily degraded without protection. Solid gold is well known for its strong chemical inertness. However, at the nanoscale, the number of surface atoms of the NPs is higher than the number of volume atoms. Thus, the surface atoms

which lack coordinative bonds with their neighbors, are less stabilized by the free-charges present at the surface of the metal NP. At the nanometric scale, this increase of the reactivity of the surface atoms may trigger the oxidation of the thin petals by the oxygen present in the medium. We tried to slow the degradation of the petals down by increasing the pH post-synthesis but despite the pH influence on the kinetics of reduction, it did not show any significant change within the degradation speed of the petals.

Another weakness also comes from their complex anisotropic structure. Compared to conventional gold nanospheres (diameters of ca. 20 nm), AuNFs are several times bigger and heavier. They are then more subject to sedimentation and their anisotropic structure favors their interweaving with their neighbors lowering their re-dispersion ability. Thus, the colloidal suspensions of AuNFs are intrinsically less stable than the colloidal suspensions of spherical AuNPs, over time. Despite that, the colloidal as the petal stability of NPs, mainly depends on their surface properties and their interaction with their environment. Therefore, it is possible to protect their structure via changing their surface properties by their coating.

4. Improvement of the stability and functionalization of the AuNFs by coating

The AuNFs can be covered by a shell made of polymers, soft and porous to ions and to molecules of water, dyes or drugs. The gold nanoflowers synthesized by the mean of the protocol that we developed, showed a good affinity with all the polymers that we tried to adsorb onto them, despite the different kinds of interactions they may have with the AuNFs surface. PEG-SH certainly coordinates onto the surface by the intermediate of its thiol group then its polyether chain certainly reinforced its adsorption through van der Waals interactions with the AuNF surface [88, 118]. PVP and poloxamers having no charge or functional group with high affinity for gold, such as thiol, certainly owe their adsorption mainly to van der Waals interactions induced by the numerous oxygen atoms (and also nitrogen in the case of PVP), of their long polymer chains, more electronegative and electrophilic [128, 134]. Alginates might chelate onto the nucleophile surface of the AuNFs by their carboxyl groups while the rest of their chains certainly also show van der Waals interactions with the surface. Chitosan probably adsorbs through van der Waals interactions, but its cationic amine groups interacting with the citrates are able to perturb the citrate protective coating and to induce NP aggregation at higher concentrations (R2 = 10). Therefore, chitosan was the only polymer studied here for which the

high concentration decreased and not increased the colloidal stability of the AuNFs. Note that at acidic pH, NPs coated with chitosan remain stable in suspension longer certainly thanks to more positive charges present on their surface due to the protonated amine groups of the polymer. On the other hand, for the studied polymers at the lowest concentrations (R2 = 0.01), the colloidal stability protection was insufficient, namely in front of the NB ability to aggregate the AuNFs. It is interesting to notice that in our study, the coated AuNFs were not washed after being incubated with the polymers, except for the PEG-SH and PVP. Thus, free polymers were also present in the solution, mainly at the highest polymer : gold ratio and could also participate in maintaining or disturbing the colloidal stability through exchanges (adsorption/desorption) with the surface of NPs.

For the PEG-SH- and PVP- coated AuNFs, the LSPR bands were not changed after they were washed twice by centrifugation and re-suspended in fresh DIW, indicating that a significant part of these polymers remained adsorbed on the gold surface. In both cases, the colloids stabilization was most probably due to the steric hindrance of the polymer chains of the neighbor NPs which were moving and sliding one on top of the other, preventing then their aggregation. In the case of the AuNFs coated with chitosan and alginate, we can think that the colloidal stability was also brought by the presence of positive or negative charges, respectively. This was confirmed by the fact that the chitosan-coated AuNFs were more stable at pH = 5 than at pH = 7.

In contrast to the improvement of the colloidal stability of the AuNFs, the polymeric coating was able to affect the analyte/reporter molecule adsorption on the gold surface, both qualitatively (adsorption geometry: favored orientation of the adsorbed molecule relative to the surface) and quantitatively (adsorption efficiency). As SERS is a short-range effect (best when the analyte/reporter is at less than 2 nm from the gold surface), the adsorption modality affects the SERS signal, both qualitatively (relative intensity of main bands) and quantitatively (overall intensity of the SERS signal). Thus, it is important to wisely choose the right polymer, able to ensure the colloidal stability and the biocompatibility while preserving the SERS activity.

It was also possible to coat our AuNFs with a more rigid and less porous silica shell than in the case of the polymeric layer described above but allowing good control of its thickness. The particularity of the protocol we used is that, unlike the standard sol-gel protocol [135, 136], the synthesis are made in an alcohol-free 100% aqueous medium (adapted from [137]). It is a

great advantage to be able to synthesize the silica shell directly in the same suspension of the freshly synthesized AuNFs without the need for intermediate washing steps or phase-transfer which often induces at least the partial aggregation of the colloids. Thus, the use of the MPTES preliminary hydrolyzed at showed very good results. The silica shell grown pretty homogeneously around the AuNFs. Even at the lowest concentration tried (MPTES/Au molar ratio of 0.02), when the silica shell was difficult to identify on the TEM images, it was revealed by its protective effect against the AuNFs oxidation and aggregation. The protocols gave a very good reproducibility between batches (three batches for each MPTES concentration) and no independent silica NPs had been observed for any batch. In contrast, the pre-coating of the AuNFs with PVP (required in standard sol-gel protocols [135]) did not improve the silica shell formation, but in contrast, led to a lot of big independent silica NPs observed on the TEM images. In comparison, with the standard sol-gel method, which works well for gold nanospheres and which we first tried to apply to our AuNFs, at a MPTES/Au molar ratio of 1, only a few AuNFs were fully coated with a thick silica layer, leading to objects of 2 to 3 times larger than the original AuNFs, or partially coated, preferentially at the tips of their petals - thus, the coating was inhomogeneous - and a lot of independent large silica NPs were generated (from 100 to 300 nm).

Shah et al. [137] showed that varying the incubation time allows tuning the silica shell thickness on their gold nanospheres but, for our AuNFs, we tuned it by varying their initial MPTES concentration without changing the incubation time between the batches (12 hours). We thus produced silica-coated AuNFs with up to 19 nm thick silica shell. They had a negative zeta potential of -50 mV and were colloidally stable in water. Therefore, in addition of the advantages previously described, this protocol seems to be pretty flexible.

Tuning the silica shell thickness of the AuNFs allows combining SERS, SEF and non-enhanced fluorescence (classic fluorescence) within the same nanoprobe, making it multimodal. Indeed, dye molecules which are the closest (< 2 nm) to the AuNF surface provide the SERS signal, while the more distant molecules from the gold surface will be more active in fluorescence. The SEF effect is dominant until ca. 10 nm and conventional fluorescence from 10 nm and beyond. The multimodal response of the silica-coated AuNFs is very promising for their applications in biosensing and imaging [57].

GENERAL CONCLUSION *(English version)*

To get the full potential of the SERS effect, practical and technical difficulties have to be overcome, mainly concerning plasmonic substrates synthesis and use. In this thesis, a one-step, facile, reliable, and conform with the bioanalytical constraints protocol was developed to synthesize aqueous suspensions of surfactant-free AuNFs presenting a surface free to interact with its environment and apparently able to adsorb a wide variety of products (analytes). Thus, these AuNFs have been further stabilized by coating them with silica or with biocompatible polymers. A strong SERS signal (exc. 690 nm laser) has been obtained with micromolar and sub-micromolar solutions of fluorophores: Nile blue and Crystal violet, without the need to aggregate the AuNFs. Furthermore, coating them with a silica shell allowed SERS and fluorescence to be generated simultaneously. In view of the observed properties, these nano-systems appear very promising as substrates for SERS spectroscopy, sensing, and imaging, as well as for a wide field of other bioanalytical applications, as we will discuss in the perspective section below.

PERSPECTIVES *(English version)*

Our surfactant-free AuNFs, by their polyvalence and their apparent affinity with a wide range of different compounds, can thus be used in many application fields.

1. Bioanalytical imaging and drug delivery

Despite that we developed these NPs in order to design polyvalent and stable SERS nanoprobes, they also can be used aside of this framework. The article by S. Ben Djemaa et al. (Annexe 1) shows another aspect of the possible use of our AuNFs as drug nanocarriers and multimodal nanoprobes. Due to the adjustment of a non-spectral laser-scanning confocal microscope (LSCM) to co-detect the dual optical response of the AuNFs: elastic scattering of light (enhanced by the plasmons) and fluorescence (from the Nile blue carried on the surface of the AuNFs), it was possible to observe that the Nile blue was desorbed from the AuNFs and diffused through the cellular membrane into the cells, while the AuNFs were attached on the membrane. Thus, associated with innovative analytical approaches based on LSCM, our AuNFs can contribute to an understanding of the nanomedicine - cell interactions. Therefore, their intrinsic various properties increase their application fields even outside of the scope of what they were originally designed for.

2. The AuNFs as a base for the design of magneto-plasmonic multimodal nanoprobes

The advantages of our AuNFs discussed above make them good candidates for the design of more complex multimodal nano-systems associating several materials of different properties. For instance, in order to enrich the potential of the AuNFs as multimodal nanoprobes, they can be associated with superparamagnetic iron oxide nanoparticles (SPIONs). SPIONs are useful as MRI (magnetic resonance imaging) imaging agents and as magnetic sorting templates. Many publications reported the association of gold and iron oxides at the nanometric scale, looking for a reliable multimodal nanoprobe [32, 65, 66, 138–144].

However, the difficulties met to reproduce their protocols, the poor investigation on the colloidal stability of the synthesized suspensions and the complexity or the final potential toxicity of the suspensions generated by these protocols show that optimizing work remains to be done in this area. In the framework of this Ph.D. thesis, such a combination has been also attempted, in various configurations (core-shell, nucleus-satellite, hybrid nano-worms, etc…) and using various protocols, based on *in situ* synthesis or on post-synthesis assembly [19, 20, 32, 57, 59, 65, 66, 136, 143, 145–147].

For instance, multimetallic AuNFs have been synthesized starting from an aqueous suspension of SPIONs (data not shown). The resulting AuNFs appeared surrounded by SPIONs, as seen in our TEM images. They have LSPR band red-shifted and enlarged but remained stable for days. That means that SPIONs stabilize the petals of the AuNFs but still allow a limited aggregation of the AuNFs. After some optimization of the SPION layer thickness, the AuNF@SPION assembly might be capped within a silica shell leading to plasmo-magnetic nanoprobes and broadening then, even more, their application field [142].

REFERENCES

[1] Fleischmann, M.; Hendra, P. J.; McQuillan, A. J. Raman Spectra of Pyridine Adsorbed at a Silver Electrode. *Chemical Physics Letters*, **1974**, *26* (2), 163–166. https://doi.org/10.1016/0009-2614(74)85388-1.

[2] Zhang, W.; Jiang, L.; Piper, J. A.; Wang, Y. SERS Nanotags and Their Applications in Biosensing and Bioimaging. *J. Anal. Test.*, **2018**, *2* (1), 26–44. https://doi.org/10.1007/s41664-018-0053-9.

[3] Jamieson, L. E.; Asiala, S. M.; Gracie, K.; Faulds, K.; Graham, D. Bioanalytical Measurements Enabled by Surface-Enhanced Raman Scattering (SERS) Probes. *Annu Rev Anal Chem (Palo Alto Calif)*, **2017**, *10* (1), 415–437. https://doi.org/10.1146/annurev-anchem-071015-041557.

[4] Li, P.; Long, F.; Chen, W.; Chen, J.; Chu, P. K.; Wang, H. Fundamentals and Applications of Surface-Enhanced Raman Spectroscopy–Based Biosensors. *Current Opinion in Biomedical Engineering*, **2020**, *13*, 51–59. https://doi.org/10.1016/j.cobme.2019.08.008.

[5] Zong, C.; Xu, M.; Xu, L.-J.; Wei, T.; Ma, X.; Zheng, X.-S.; Hu, R.; Ren, B. Surface-Enhanced Raman Spectroscopy for Bioanalysis: Reliability and Challenges. *Chem. Rev.*, **2018**, *118* (10), 4946–4980. https://doi.org/10.1021/acs.chemrev.7b00668.

[6] McNay, G.; Eustace, D.; Smith, W. E.; Faulds, K.; Graham, D. Surface-Enhanced Raman Scattering (SERS) and Surface-Enhanced Resonance Raman Scattering (SERRS): A Review of Applications. *Applied Spectroscopy*, **2011**, *65* (8), 825–837. https://doi.org/10.1366/11-06365.

[7] Wang, Y.; Yan, B.; Chen, L. SERS Tags: Novel Optical Nanoprobes for Bioanalysis. *Chemical Reviews*, **2013**, *113* (3), 1391–1428. https://doi.org/10.1021/cr300120g.

[8] Prado, E. Détection de l'ADN Par Spectrométrie de Diffusion Raman Exaltée de Surface Couplée à La Microfluidique. thesis, Bordeaux 1, 2011.

[9] Le Ru, E. C.; Etchegoin, P. G. *Principles of Surface-Enhanced Raman Spectroscopy: And Related Plasmonic Effects*, 1st ed.; Elsevier: Amsterdam ; Boston, 2009.

[10] Patel, I. S.; Premasiri, W. R.; Moir, D. T.; Ziegler, L. D. Barcoding Bacterial Cells: A SERS-Based Methodology for Pathogen Identification. *Journal of Raman Spectroscopy*, **2008**, *39* (11), 1660–1672. https://doi.org/10.1002/jrs.2064.

[11] Vo-Dinh, T. Biomedical Photonics Handbook. 1787.

[12] Smith, A. M.; Mancini, M. C.; Nie, S. Second Window for in Vivo Imaging: Bioimaging. *Nature Nanotechnology*, **2009**, *4* (11), 710–711. https://doi.org/10.1038/nnano.2009.326.

[13] Weissleder, R. A Clearer Vision for in Vivo Imaging. *Nat. Biotechnol.*, **2001**, *19* (4), 316–317. https://doi.org/10.1038/86684.

[14] Wang, Z.; Zhang, J.; Ekman, J. M.; Kenis, P. J. A.; Lu, Y. DNA-Mediated Control of Metal Nanoparticle Shape: One-Pot Synthesis and Cellular Uptake of Highly Stable and Functional Gold Nanoflowers. *Nano Lett.*, **2010**, *10* (5), 1886–1891. https://doi.org/10.1021/nl100675p.

[15] Vigderman, L.; Khanal, B. P.; Zubarev, E. R. Functional Gold Nanorods: Synthesis, Self-Assembly, and Sensing Applications. *Adv. Mater.*, **2012**, *24* (36), 4811–4841. https://doi.org/10.1002/adma.201201690.

[16] Yuan, H.; Khoury, C. G.; Hwang, H.; Wilson, C. M.; Grant, G. A.; Vo-Dinh, T. Gold Nanostars: Surfactant-Free Synthesis, 3D Modelling, and Two-Photon

Photoluminescence Imaging. *Nanotechnology*, **2012**, *23* (7), 075102. https://doi.org/10.1088/0957-4484/23/7/075102.
[17] De Silva Indrasekara, A. S.; Johnson, S. F.; Odion, R. A.; Vo-Dinh, T. Manipulation of the Geometry and Modulation of the Optical Response of Surfactant-Free Gold Nanostars: A Systematic Bottom-Up Synthesis. *ACS Omega*, **2018**, *3* (2), 2202–2210. https://doi.org/10.1021/acsomega.7b01700.
[18] Ayala-Orozco, C.; Liu, J. G.; Knight, M. W.; Wang, Y.; Day, J. K.; Nordlander, P.; Halas, N. J. Fluorescence Enhancement of Molecules Inside a Gold Nanomatryoshka. *Nano Lett.*, **2014**, 8.
[19] Turkevich, J.; Stevenson, P. C.; Hillier, J. A Study of the Nucleation and Growth Processes in the Synthesis of Colloidal Gold. *Discussions of the Faraday Society*, **1951**, *11*, 55. https://doi.org/10.1039/df9511100055.
[20] Ruiz-Sanchez, A. J.; Parolo, C.; Miller, B. S.; Gray, E. R.; Schlegel, K.; McKendry, R. A. Tuneable Plasmonic Gold Dendrimer Nanochains for Sensitive Disease Detection. *J. Mater. Chem. B*, **2017**, *5* (35), 7262–7266. https://doi.org/10.1039/C7TB01394A.
[21] Dykman, L.; Khlebtsov, N. Gold Nanoparticles in Biomedical Applications: Recent Advances and Perspectives. *Chem. Soc. Rev.*, **2012**, *41* (6), 2256–2282. https://doi.org/10.1039/C1CS15166E.
[22] Stiles, P. L.; Dieringer, J. A.; Shah, N. C.; Van Duyne, R. P. Surface-Enhanced Raman Spectroscopy. *Annual Rev. Anal. Chem.*, **2008**, *1* (1), 601–626. https://doi.org/10.1146/annurev.anchem.1.031207.112814.
[23] Mosier-Boss, P. A. Review of SERS Substrates for Chemical Sensing. *Nanomaterials (Basel)*, **2017**, *7* (6). https://doi.org/10.3390/nano7060142.
[24] Nikoobakht, B.; El-Sayed, M. A. Preparation and Growth Mechanism of Gold Nanorods (NRs) Using Seed-Mediated Growth Method. *Chem. Mater.*, **2003**, *15* (10), 1957–1962. https://doi.org/10.1021/cm020732l.
[25] Huang, X.; Neretina, S.; El-Sayed, M. A. Gold Nanorods: From Synthesis and Properties to Biological and Biomedical Applications. *Advanced Materials*, **2009**, *21* (48), 4880–4910. https://doi.org/10.1002/adma.200802789.
[26] Edgar, J. A.; Zareie, H. M.; Blaber, M.; Dowd, A.; Cortie, M. B. Synthesis of Hollow Gold Nanoparticles and Rings Using Silver Templates. In *2008 International Conference on Nanoscience and Nanotechnology*; 2008; pp 36–39. https://doi.org/10.1109/ICONN.2008.4639239.
[27] Maiorano, G.; Rizzello, L.; Malvindi, M. A.; Shankar, S. S.; Martiradonna, L.; Falqui, A.; Cingolani, R.; Pompa, P. P. Monodispersed and Size-Controlled Multibranched Gold Nanoparticles with Nanoscale Tuning of Surface Morphology. *Nanoscale*, **2011**, *3* (5), 2227–2232. https://doi.org/10.1039/c1nr10107b.
[28] Ahmed, W.; Kooij, E. S.; Silfhout, A. van; Poelsema, B. Controlling the Morphology of Multi-Branched Gold Nanoparticles. *Nanotechnology*, **2010**, *21* (12), 125605. https://doi.org/10.1088/0957-4484/21/12/125605.
[29] Rodríguez-Lorenzo, L.; Álvarez-Puebla, R. A.; de Abajo, F. J. G.; Liz-Marzán, L. M. Surface Enhanced Raman Scattering Using Star-Shaped Gold Colloidal Nanoparticles. *J. Phys. Chem. C*, **2010**, *114* (16), 7336–7340. https://doi.org/10.1021/jp909253w.
[30] Pazos-Perez, N.; Fitzgerald, J. M.; Giannini, V.; Guerrini, L.; Alvarez-Puebla, R. A. Modular Assembly of Plasmonic Core–Satellite Structures as Highly Brilliant SERS-Encoded Nanoparticles. *Nanoscale Adv.*, **2019**, *1* (1), 122–131. https://doi.org/10.1039/C8NA00257F.
[31] Rzeznicka, I.; Horino, H. Nanoscale Insights into Enhanced Raman Spectroscopy. In *Raman Spectroscopy*; Nascimento, G. M. do, Ed.; InTech, 2018; pp 67–89. https://doi.org/10.5772/intechopen.72284.

[32] Zhou, J.; Xiong, Q.; Ma, J.; Ren, J.; Messersmith, P. B.; Chen, P.; Duan, H. Polydopamine-Enabled Approach toward Tailored Plasmonic Nanogapped Nanoparticles: From Nanogap Engineering to Multifunctionality. *ACS Nano*, **2016**, 10.
[33] Zhang, T.; Li, H.; Hou, S.; Dong, Y.; Pang, G.; Zhang, Y. Construction of Plasmonic Core–Satellite Nanostructures on Substrates Based on DNA-Directed Self-Assembly as a Sensitive and Reproducible Biosensor. *ACS Appl. Mater. Interfaces*, **2015**, *7* (49), 27131–27139. https://doi.org/10.1021/acsami.5b07152.
[34] Raman, C. V.; Krishnan, K. S. A New Type of Secondary Radiation. *Nature*, **1928**, *121*, 501–502.
[35] Barbillat, J.; Bougeard, D.; Buntinx, G.; Delhaye, M.; Dhamelincourt, P.; Fillaux, F. Spectrométrie Raman. **1999**, 34.
[36] Humbert, B.; Mevellec, J.-Y.; Grausem, J.; Dossot, M.; Carteret, C. Spectrométrie d'absorption Dans l'infrarouge. *Techniques de l'ingénieur Spectrométries*, **2012**, *base documentaire : TIB390DUO.* (ref. article : p2850).
[37] Andrews, D. L. Rayleigh Scattering and Raman Spectroscopy, Theory. In *Encyclopedia of Spectroscopy and Spectrometry*; Lindon, J. C., Ed.; Elsevier: Oxford, 1999; pp 1993–2000. https://doi.org/10.1006/rwsp.2000.0260.
[38] Ferraro, J. R.; Nakamoto, K.; Brown, C. W. *Introductory Raman Spectroscopy*, 2nd ed.; Academic Press: Amsterdam ; Boston, 2003.
[39] Bohren, C. F.; Huffman, D. R. *Absorption and Scattering of Light by Small Particles*; Wiley: New York, 1983.
[40] Lakowicz, J. R.; Masters, B. R. Principles of Fluorescence Spectroscopy, Third Edition. *J. Biomed. Opt.*, **2008**, *13* (2), 029901. https://doi.org/10.1117/1.2904580.
[41] Nusimovici, M. Règles de sélection pour la diffusion Raman et l'absorption infrarouge dans la wurtzite. *J. Phys. France*, **1965**, *26* (11), 689–696. https://doi.org/10.1051/jphys:019650026011068900.
[42] Kuhar, N.; Sil, S.; Verma, T.; Umapathy, S. Challenges in Application of Raman Spectroscopy to Biology and Materials. *RSC Adv.*, **2018**, *8* (46), 25888–25908. https://doi.org/10.1039/C8RA04491K.
[43] Hildebrandt, P.; Lecomte, S. Biochemical Applications of Raman Spectroscopy. In *Encyclopedia of Spectroscopy and Spectrometry*; Lindon, J. C., Ed.; Elsevier: Oxford, 1999; pp 88–97. https://doi.org/10.1006/rwsp.2000.0017.
[44] Ishida, H.; Kamoto, R.; Uchida, S.; Ishitani, A.; Ozaki, Y.; Iriyama, K.; Tsukie, E.; Shibata, K.; Ishihara, F.; Kameda, H. Raman Microprobe and Fourier Transform-Infrared Microsampling Studies of the Microstructure of Gallstones. *Appl Spectrosc*, **1987**, *41* (3), 407–412. https://doi.org/10.1366/0003702874448779.
[45] Cui, X.; Zhao, Z.; Zhang, G.; Chen, S.; Zhao, Y.; Lu, J. Analysis and Classification of Kidney Stones Based on Raman Spectroscopy. *Biomed Opt Express*, **2018**, *9* (9), 4175–4183. https://doi.org/10.1364/BOE.9.004175.
[46] Kong, K.; Kendall, C.; Stone, N.; Notingher, I. Raman Spectroscopy for Medical Diagnostics--From in-Vitro Biofluid Assays to in-Vivo Cancer Detection. *Adv. Drug Deliv. Rev.*, **2015**, *89*, 121–134. https://doi.org/10.1016/j.addr.2015.03.009.
[47] Jeanmaire, D. L.; Van Duyne, R. P. Surface Raman Spectroelectrochemistry: Part I. Heterocyclic, Aromatic, and Aliphatic Amines Adsorbed on the Anodized Silver Electrode. *Journal of Electroanalytical Chemistry and Interfacial Electrochemistry*, **1977**, *84* (1), 1–20. https://doi.org/10.1016/S0022-0728(77)80224-6.
[48] Albrecht, M. G.; Creighton, J. A. Anomalously Intense Raman Spectra of Pyridine at a Silver Electrode. *J. Am. Chem. Soc.*, **1977**, *99* (15), 5215–5217. https://doi.org/10.1021/ja00457a071.

[49] Billmann, J.; Kovacs, G.; Otto, A. Enhanced Raman Effect from Cyanide Adsorbed on a Silver Electrode. *Surface Science*, **1980**, *92* (1), 153–173. https://doi.org/10.1016/0039-6028(80)90250-2.
[50] Caucheteur, C. Plasmons de surface : principes physiques et applications. **2014**, 17.
[51] Xu, H.; Aizpurua, J.; Käll, M.; Apell, P. Electromagnetic Contributions to Single-Molecule Sensitivity in Surface-Enhanced Raman Scattering. *Phys. Rev. E*, **2000**, *62* (3), 4318–4324. https://doi.org/10.1103/PhysRevE.62.4318.
[52] Le Ru, E. C.; Etchegoin, P. G. Single-Molecule Surface-Enhanced Raman Spectroscopy. *Annu Rev Phys Chem*, **2012**, *63*, 65–87. https://doi.org/10.1146/annurev-physchem-032511-143757.
[53] Le Ru, E. C.; Etchegoin, P. G.; Meyer, M. Enhancement Factor Distribution around a Single Surface-Enhanced Raman Scattering Hot Spot and Its Relation to Single Molecule Detection. *The Journal of Chemical Physics*, **2006**, *125* (20), 204701. https://doi.org/10.1063/1.2390694.
[54] Han, X.; Goebl, J.; Lu, Z.; Yin, Y. Role of Salt in the Spontaneous Assembly of Charged Gold Nanoparticles in Ethanol. *Langmuir*, **2011**, *27* (9), 5282–5289. https://doi.org/10.1021/la200459t.
[55] Pamies, R.; Cifre, J. G. H.; Espín, V. F.; Collado-González, M.; Baños, F. G. D.; de la Torre, J. G. Aggregation Behaviour of Gold Nanoparticles in Saline Aqueous Media. *J Nanopart Res*, **2014**, *16* (4), 2376. https://doi.org/10.1007/s11051-014-2376-4.
[56] Otto, A.; Bruckbauer, A.; Chen, Y. X. On the Chloride Activation in SERS and Single Molecule SERS. *Journal of Molecular Structure*, **2003**, *661–662*, 501–514. https://doi.org/10.1016/j.molstruc.2003.07.026.
[57] Carrouée, A.; Allard-Vannier, E.; Même, S.; Szeremeta, F.; Beloeil, J.-C.; Chourpa, I. Sensitive Trimodal Magnetic Resonance Imaging-Surface-Enhanced Resonance Raman Scattering-Fluorescence Detection of Cancer Cells with Stable Magneto-Plasmonic Nanoprobes. *Anal. Chem.*, **2015**, *87* (22), 11233–11241. https://doi.org/10.1021/acs.analchem.5b02419.
[58] Jana, N. R.; Gearheart, L.; Murphy, C. J. Seeding Growth for Size Control of 5−40 Nm Diameter Gold Nanoparticles. *Langmuir*, **2001**, *17* (22), 6782–6786. https://doi.org/10.1021/la0104323.
[59] Duff, D. G.; Baiker, A.; Edwards, P. P. A New Hydrosol of Gold Clusters. 1. Formation and Particle Size Variation. *Langmuir*, **1993**, *9* (9), 2301–2309. https://doi.org/10.1021/la00033a010.
[60] Shkilnyy, A.; Soucé, M.; Dubois, P.; Warmont, F.; Saboungi, M.-L.; Chourpa, I. Poly(Ethylene Glycol)-Stabilized Silver Nanoparticles for Bioanalytical Applications of SERS Spectroscopy. *Analyst*, **2009**, *134* (9), 1868. https://doi.org/10.1039/b905694g.
[61] Šimáková, P.; Gautier, J.; Procházka, M.; Hervé-Aubert, K.; Chourpa, I. Polyethylene-Glycol-Stabilized Ag Nanoparticles for Surface-Enhanced Raman Scattering Spectroscopy: Ag Surface Accessibility Studied Using Metalation of Free-Base Porphyrins. *J. Phys. Chem. C*, **2014**, *118* (14), 7690–7697. https://doi.org/10.1021/jp5005709.
[62] Li, J. F.; Huang, Y. F.; Ding, Y.; Yang, Z. L.; Li, S. B.; Zhou, X. S.; Fan, F. R.; Zhang, W.; Zhou, Z. Y.; Wu, D. Y.; et al. Shell-Isolated Nanoparticle-Enhanced Raman Spectroscopy. *Nature*, **2010**, *464* (7287), 392–395. https://doi.org/10.1038/nature08907.
[63] Reznickova, A.; Slavikova, N.; Kolska, Z.; Kolarova, K.; Belinova, T.; Hubalek Kalbacova, M.; Cieslar, M.; Svorcik, V. PEGylated Gold Nanoparticles: Stability, Cytotoxicity and Antibacterial Activity. *Colloids and Surfaces A: Physicochemical and Engineering Aspects*, **2019**, *560*, 26–34. https://doi.org/10.1016/j.colsurfa.2018.09.083.

[64] Mine, E.; Yamada, A.; Kobayashi, Y.; Konno, M.; Liz-Marzán, L. M. Direct Coating of Gold Nanoparticles with Silica by a Seeded Polymerization Technique. *Journal of Colloid and Interface Science*, **2003**, *264* (2), 385–390. https://doi.org/10.1016/S0021-9797(03)00422-3.
[65] Gao, Y.; Li, Y.; Wang, Y.; Chen, Y.; Gu, J.; Zhao, W.; Ding, J.; Shi, J. Controlled Synthesis of Multilayered Gold Nanoshells for Enhanced Photothermal Therapy and SERS Detection. *Small*, **2015**, *11* (1), 77–83. https://doi.org/10.1002/smll.201402149.
[66] Wu, W.; He, Q.; Chen, H.; Tang, J.; Nie, L. Sonochemical Synthesis, Structure and Magnetic Properties of Air-Stable Fe_3O_4 / Au Nanoparticles. *Nanotechnology*, **2007**, *18* (14), 145609. https://doi.org/10.1088/0957-4484/18/14/145609.
[67] Fratoddi, I.; Venditti, I.; Cametti, C.; Russo, M. V. How Toxic Are Gold Nanoparticles? The State-of-the-Art. *Nano Res.*, **2015**, *8* (6), 1771–1799. https://doi.org/10.1007/s12274-014-0697-3.
[68] Li, J.; Wu, J.; Zhang, X.; Liu, Y.; Zhou, D.; Sun, H.; Zhang, H.; Yang, B. Controllable Synthesis of Stable Urchin-like Gold Nanoparticles Using Hydroquinone to Tune the Reactivity of Gold Chloride. *J. Phys. Chem. C*, **2011**, *115* (9), 3630–3637. https://doi.org/10.1021/jp1119074.
[69] Jiji, S. G.; Gopchandran, K. G. Synthesis of Gold Nanoflowers and Their High SERS Performance. *Materials Today: Proceedings*, **2015**, *2* (3), 928–933. https://doi.org/10.1016/j.matpr.2015.06.011.
[70] Rodríguez-Lorenzo, L.; Álvarez-Puebla, R. A.; Pastoriza-Santos, I.; Mazzucco, S.; Stéphan, O.; Kociak, M.; Liz-Marzán, L. M.; García de Abajo, F. J. Zeptomol Detection Through Controlled Ultrasensitive Surface-Enhanced Raman Scattering. *Journal of the American Chemical Society*, **2009**, *131* (13), 4616–4618. https://doi.org/10.1021/ja809418t.
[71] Xie, W.; Schlücker, S. Hot Electron-Induced Reduction of Small Molecules on Photorecycling Metal Surfaces. *Nat Commun*, **2015**, *6* (1), 1–6. https://doi.org/10.1038/ncomms8570.
[72] Tang, L.; Yu, G.; Tan, L.; Li, M.; Deng, X.; Liu, J.; Li, A.; Lai, X.; Hu, J. Highly Stabilized Core-Satellite Gold Nanoassemblies in Vivo: DNA-Directed Self-Assembly, PEG Modification and Cell Imaging. *Sci Rep*, **2017**, *7* (1), 1–10. https://doi.org/10.1038/s41598-017-08903-0.
[73] Manson, J.; Kumar, D.; Meenan, B. J.; Dixon, D. Polyethylene Glycol Functionalized Gold Nanoparticles: The Influence of Capping Density on Stability in Various Media. *Gold Bulletin*, **2011**, *44* (2), 99–105. https://doi.org/10.1007/s13404-011-0015-8.
[74] Ajdari, N.; Vyas, C.; Bogan, S. L.; Lwaleed, B. A.; Cousins, B. G. Gold Nanoparticle Interactions in Human Blood: A Model Evaluation. *Nanomedicine: Nanotechnology, Biology and Medicine*, **2017**, *13* (4), 1531–1542. https://doi.org/10.1016/j.nano.2017.01.019.
[75] Liu, X. Y.; Nothias, J.-M.; Scavone, A.; Garfinkel, M.; Millis, J. M. Biocompatibility Investigation of Polyethylene Glycol and Alginate-Poly-l-Lysine for Islet Encapsulation: *ASAIO Journal*, **2010**, *56* (3), 241–245. https://doi.org/10.1097/MAT.0b013e3181d7b8e3.
[76] Cruje, C.; Chithrani, D. B. Polyethylene Glycol Functionalized Nanoparticles for Improved Cancer Treatment. *Reviews in Nanoscience and Nanotechnology*, **2014**, *3* (1), 20–30. https://doi.org/10.1166/rnn.2014.1042.
[77] Cauda, V.; Argyo, C.; Bein, T. Impact of Different PEGylation Patterns on the Long-Term Bio-Stability of Colloidal Mesoporous Silica Nanoparticles. *Journal of Materials Chemistry*, **2010**, *20* (39), 8693. https://doi.org/10.1039/c0jm01390k.

[78] Dobrovolskaia, M. A.; Aggarwal, P.; Hall, J. B.; McNeil, S. E. Preclinical Studies To Understand Nanoparticle Interaction with the Immune System and Its Potential Effects on Nanoparticle Biodistribution. *Molecular Pharmaceutics*, **2008**, *5* (4), 487–495. https://doi.org/10.1021/mp800032f.
[79] Laurent, S.; Boutry, S.; Mahieu, I.; Elst, L.; Muller, R. Iron Oxide Based MR Contrast Agents: From Chemistry to Cell Labeling. *Current Medicinal Chemistry*, **2009**, *16* (35), 4712–4727. https://doi.org/10.2174/092986709789878256.
[80] Maeda, H.; Wu, J.; Sawa, T.; Matsumura, Y.; Hori, K. Tumor Vascular Permeability and the EPR Effect in Macromolecular Therapeutics: A Review. *Journal of Controlled Release*, **2000**, *65* (1–2), 271–284. https://doi.org/10.1016/S0168-3659(99)00248-5.
[81] Adiseshaiah, P. P.; Hall, J. B.; McNeil, S. E. Nanomaterial Standards for Efficacy and Toxicity Assessment: Nanomaterial Standards for Efficacy and Toxicity Assessment. *Wiley Interdisciplinary Reviews: Nanomedicine and Nanobiotechnology*, **2010**, *2* (1), 99–112. https://doi.org/10.1002/wnan.66.
[82] Couvreur, P.; Vauthier, C. Nanotechnology: Intelligent Design to Treat Complex Disease. *Pharmaceutical Research*, **2006**, *23* (7), 1417–1450. https://doi.org/10.1007/s11095-006-0284-8.
[83] Alric, C.; Aubrey, N.; Allard-Vannier, É.; di Tommaso, A.; Blondy, T.; Dimier-Poisson, I.; Chourpa, I.; Hervé-Aubert, K. Covalent Conjugation of Cysteine-Engineered ScFv to PEGylated Magnetic Nanoprobes for Immunotargeting of Breast Cancer Cells. *RSC Adv.*, **2016**, *6* (43), 37099–37109. https://doi.org/10.1039/C6RA06076E.
[84] Hainfeld, J. F.; Slatkin, D. N.; Focella, T. M.; Smilowitz, H. M. Gold Nanoparticles: A New X-Ray Contrast Agent. *BJR*, **2006**, *79* (939), 248–253. https://doi.org/10.1259/bjr/13169882.
[85] De Jong, W. H.; Hagens, W. I.; Krystek, P.; Burger, M. C.; Sips, A. J. A. M.; Geertsma, R. E. Particle Size-Dependent Organ Distribution of Gold Nanoparticles after Intravenous Administration. *Biomaterials*, **2008**, *29* (12), 1912–1919. https://doi.org/10.1016/j.biomaterials.2007.12.037.
[86] Hoshyar, N.; Gray, S.; Han, H.; Bao, G. The Effect of Nanoparticle Size on in Vivo Pharmacokinetics and Cellular Interaction. *Nanomedicine (Lond)*, **2016**, *11* (6), 673–692. https://doi.org/10.2217/nnm.16.5.
[87] Shan, X.; Yuan, Y.; Liu, C.; Tao, X.; Sheng, Y.; Xu, F. Influence of PEG Chain on the Complement Activation Suppression and Longevity in Vivo Prolongation of the PCL Biomedical Nanoparticles. *Biomedical Microdevices*, **2009**, *11* (6), 1187–1194. https://doi.org/10.1007/s10544-009-9336-2.
[88] Karakoti, A. S.; Das, S.; Thevuthasan, S.; Seal, S. PEGylated Inorganic Nanoparticles. *Angewandte Chemie International Edition*, **2011**, *50* (9), 1980–1994. https://doi.org/10.1002/anie.201002969.
[89] Hervé, K.; Douziech-Eyrolles, L.; Munnier, E.; Cohen-Jonathan, S.; Soucé, M.; Marchais, H.; Limelette, P.; Warmont, F.; Saboungi, M. L.; Dubois, P.; et al. The Development of Stable Aqueous Suspensions of PEGylated SPIONs for Biomedical Applications. *Nanotechnology*, **2008**, *19* (46), 465608. https://doi.org/10.1088/0957-4484/19/46/465608.
[90] Lankveld, D. P.; Rayavarapu, R. G.; Krystek, P.; Oomen, A. G.; Verharen, H. W.; van Leeuwen, T. G.; De Jong, W. H.; Manohar, S. Blood Clearance and Tissue Distribution of PEGylated and Non-PEGylated Gold Nanorods after Intravenous Administration in Rats. *Nanomedicine*, **2011**, *6* (2), 339–349. https://doi.org/10.2217/nnm.10.122.
[91] Allard-Vannier, E.; Cohen-Jonathan, S.; Gautier, J.; Hervé-Aubert, K.; Munnier, E.; Soucé, M.; Legras, P.; Passirani, C.; Chourpa, I. Pegylated Magnetic Nanocarriers for Doxorubicin Delivery: A Quantitative Determination of Stealthiness in Vitro and in Vivo.

European Journal of Pharmaceutics and Biopharmaceutics, **2012**, *81* (3), 498–505. https://doi.org/10.1016/j.ejpb.2012.04.002.

[92] Allard-Vannier, E.; Hervé-Aubert, K.; Kaaki, K.; Blondy, T.; Shebanova, A.; Shaitan, K. V.; Ignatova, A. A.; Saboungi, M.-L.; Feofanov, A. V.; Chourpa, I. Folic Acid-Capped PEGylated Magnetic Nanoparticles Enter Cancer Cells Mostly via Clathrin-Dependent Endocytosis. *Biochimica et Biophysica Acta (BBA) - General Subjects*, **2017**, *1861* (6), 1578–1586. https://doi.org/10.1016/j.bbagen.2016.11.045.

[93] Gref, R.; Lück, M.; Quellec, P.; Marchand, M.; Dellacherie, E.; Harnisch, S.; Blunk, T.; Müller, R. H. 'Stealth' Corona-Core Nanoparticles Surface Modified by Polyethylene Glycol (PEG): Influences of the Corona (PEG Chain Length and Surface Density) and of the Core Composition on Phagocytic Uptake and Plasma Protein Adsorption. *Colloids and Surfaces B: Biointerfaces*, **2000**, *18* (3–4), 301–313. https://doi.org/10.1016/S0927-7765(99)00156-3.

[94] Peracchia, M. T.; Vauthier, C.; Passirani, C.; Couvreur, P.; Labarre, D. Complement consumption by poly(ethylene glycol) in different conformations chemically coupled to poly(isobutyl 2xyanoacrylate) nanoparticles. **1997**, *61* (7), 13.

[95] Sabharanjak, S. Folate Receptor Endocytosis and Trafficking. *Advanced Drug Delivery Reviews*, **2004**, *56* (8), 1099–1109. https://doi.org/10.1016/j.addr.2004.01.010.

[96] Leamon, C. Folate-Targeted Chemotherapy. *Advanced Drug Delivery Reviews*, **2004**, *56* (8), 1127–1141. https://doi.org/10.1016/j.addr.2004.01.008.

[97] Kaaki, K.; Hervé-Aubert, K.; Chiper, M.; Shkilnyy, A.; Soucé, M.; Benoit, R.; Paillard, A.; Dubois, P.; Saboungi, M.-L.; Chourpa, I. Magnetic Nanocarriers of Doxorubicin Coated with Poly(Ethylene Glycol) and Folic Acid: Relation between Coating Structure, Surface Properties, Colloidal Stability, and Cancer Cell Targeting. *Langmuir*, **2012**, *28* (2), 1496–1505. https://doi.org/10.1021/la2037845.

[98] Parker, N.; Turk, M. J.; Westrick, E.; Lewis, J. D.; Low, P. S.; Leamon, C. P. Folate Receptor Expression in Carcinomas and Normal Tissues Determined by a Quantitative Radioligand Binding Assay. *Analytical Biochemistry*, **2005**, *338* (2), 284–293. https://doi.org/10.1016/j.ab.2004.12.026.

[99] Milletti, F. Cell-Penetrating Peptides: Classes, Origin, and Current Landscape. *Drug Discovery Today*, **2012**, *17* (15), 850–860. https://doi.org/10.1016/j.drudis.2012.03.002.

[100] Kontermann, R. E. Immunoliposomes for Cancer Therapy. *Breast cancer, Current Opinion in Molecular Therapeutics,* 2006, 8(1), ISSN 1464-8431.

[101] Vigor, K. L.; Kyrtatos, P. G.; Minogue, S.; Al-Jamal, K. T.; Kogelberg, H.; Tolner, B.; Kostarelos, K.; Begent, R. H.; Pankhurst, Q. A.; Lythgoe, M. F.; et al. Nanoparticles Functionalised with Recombinant Single Chain Fv Antibody Fragments (ScFv) for the Magnetic Resonance Imaging of Cancer Cells. *Biomaterials*, **2010**, *31* (6), 1307–1315. https://doi.org/10.1016/j.biomaterials.2009.10.036.

[102] Debaisieux, S.; Rayne, F.; Yezid, H.; Beaumelle, B. The Ins and Outs of HIV-1 Tat. *Traffic*, **2012**, *13* (3), 355–363. https://doi.org/10.1111/j.1600-0854.2011.01286.x.

[103] Smith, C.-A. M.; Fuente, J. de la; Pelaz, B.; Furlani, E. P.; Mullin, M.; Berry, C. C. The Effect of Static Magnetic Fields and Tat Peptides on Cellular and Nuclear Uptake of Magnetic Nanoparticles. *Biomaterials*, **2010**, *31* (15), 4392–4400. https://doi.org/10.1016/j.biomaterials.2010.01.096.

[104] Falanga, A.; Galdiero, M.; Galdiero, S. Membranotropic Cell Penetrating Peptides: The Outstanding Journey. *International Journal of Molecular Sciences*, **2015**, *16* (10), 25323–25337. https://doi.org/10.3390/ijms161025323.

[105] Galdiero, S.; Falanga, A.; Vitiello, M.; Grieco, P.; Caraglia, M.; Morelli, G.; Galdiero, M. Exploitation of Viral Properties for Intracellular Delivery: Viral properties for

intracellular delivery. *Journal of Peptide Science*, **2014**, *20* (7), 468–478. https://doi.org/10.1002/psc.2649.
[106] Ben Djemaa, S.; Hervé-Aubert, K.; Lajoie, L.; Falanga, A.; Galdiero, S.; Nedellec, S.; Soucé, M.; Munnier, E.; Chourpa, I.; David, S.; et al. GH625 Cell-Penetrating Peptide Promotes the Endosomal Escape of Nanovectorized SiRNA in a Triple-Negative Breast Cancer Cell Line. *Biomacromolecules*, **2019**, *20* (8), 3076–3086. https://doi.org/10.1021/acs.biomac.9b00637.
[107] Fay, F.; Scott, C. J. Antibody-Targeted Nanoparticles for Cancer Therapy. *Immunotherapy*, **2011**, *3* (3), 381–394. https://doi.org/10.2217/imt.11.5.
[108] Jun, Y.; Lee, J.; Cheon, J. Chemical Design of Nanoparticle Probes for High-Performance Magnetic Resonance Imaging. *Angewandte Chemie International Edition*, **2008**, *47* (28), 5122–5135. https://doi.org/10.1002/anie.200701674.
[109] Yang, H.-M.; Park, C. W.; Woo, M.-A.; Kim, M. I.; Jo, Y. M.; Park, H. G.; Kim, J.-D. HER2/Neu Antibody Conjugated Poly(Amino Acid)-Coated Iron Oxide Nanoparticles for Breast Cancer MR Imaging. *Biomacromolecules*, **2010**, *11* (11), 2866–2872. https://doi.org/10.1021/bm100560m.
[110] Montenegro, J.-M.; Grazu, V.; Sukhanova, A.; Agarwal, S.; de la Fuente, J. M.; Nabiev, I.; Greiner, A.; Parak, W. J. Controlled Antibody/(Bio-) Conjugation of Inorganic Nanoparticles for Targeted Delivery. *Advanced Drug Delivery Reviews*, **2013**, *65* (5), 677–688. https://doi.org/10.1016/j.addr.2012.12.003.
[111] Shanehsazzadeh, S.; Gruettner, C.; Lahooti, A.; Mahmoudi, M.; Allen, B. J.; Ghavami, M.; Daha, F. J.; Oghabian, M. A. Monoclonal Antibody Conjugated Magnetic Nanoparticles Could Target MUC-1-Positive Cells *in Vitro* but Not *in Vivo*: c595-uspio could target muc-1 positive cells *in vitro* but not *in vivo*. *Contrast Media & Molecular Imaging*, **2015**, *10* (3), 225–236. https://doi.org/10.1002/cmmi.1627.
[112] Conde, J.; Bao, C.; Cui, D.; Baptista, P. V.; Tian, F. Antibody–Drug Gold Nanoantennas with Raman Spectroscopic Fingerprints for in Vivo Tumour Theranostics. *Journal of Controlled Release*, **2014**, *183*, 87–93. https://doi.org/10.1016/j.jconrel.2014.03.045.
[113] Nehl, C. L.; Liao, H.; Hafner, J. H. Optical Properties of Star-Shaped Gold Nanoparticles. *Nano Lett.*, **2006**, *6* (4), 683–688. https://doi.org/10.1021/nl052409y.
[114] Jena, B. K.; Raj, C. R. Seedless, Surfactantless Room Temperature Synthesis of Single Crystalline Fluorescent Gold Nanoflowers with Pronounced SERS and Electrocatalytic Activity. *Chem. Mater.*, **2008**, *20* (11), 3546–3548. https://doi.org/10.1021/cm7019608.
[115] Jiang, Y.; Wu, X.-J.; Li, Q.; Li, J.; Xu, D. Facile Synthesis of Gold Nanoflowers with High Surface-Enhanced Raman Scattering Activity. *Nanotechnology*, **2011**, *22* (38), 385601. https://doi.org/10.1088/0957-4484/22/38/385601.
[116] Veronese, F. M.; Pasut, G. PEGylation, Successful Approach to Drug Delivery. *Drug Discov. Today*, **2005**, *10* (21), 1451–1458. https://doi.org/10.1016/S1359-6446(05)03575-0.
[117] Gullotti_Yeo - 2009 - Extracellularly Activated Nanocarriers.Pdf.
[118] Xue, Y.; Li, X.; Li, H.; Zhang, W. Quantifying Thiol–Gold Interactions towards the Efficient Strength Control. *Nature Communications*, **2014**, *5* (1). https://doi.org/10.1038/ncomms5348.
[119] Wenzel, J. G. W.; Balaji, K. S. S.; Koushik, K.; Navarre, C.; Duran, S. H.; Rahe, C. H.; Kompella, U. B. Pluronic F127 Gel Formulations of Deslorelin and GnRH Reduce Drug Degradation and Sustain Drug Release and Effect in Cattle. *J Control Release*, **2002**, *85* (1–3), 51–59. https://doi.org/10.1016/s0168-3659(02)00271-7.
[120] Bourre, L.; Thibaut, S.; Briffaud, A.; Lajat, Y.; Patrice, T. Potential Efficacy of a Delta 5-Aminolevulinic Acid Thermosetting Gel Formulation for Use in Photodynamic Therapy

of Lesions of the Gastrointestinal Tract. *Pharmacol. Res.*, **2002**, *45* (2), 159–165. https://doi.org/10.1006/phrs.2001.0934.
[121] Yong, C. S.; Choi, J. S.; Quan, Q. Z.; Rhee, J. D.; Kim, C. K.; Lim, S. J.; Kim, K. M.; Oh, P. S.; Choi, H. G. Effect of Sodium Chloride on the Gelation Temperature, Gel Strength and Bioadhesive Force of Poloxamer Gels Containing Diclofenac Sodium. *Int J Pharm*, **2001**, *226* (1–2), 195–205. https://doi.org/10.1016/s0378-5173(01)00809-2.
[122] Dumortier, G.; Grossiord, J. L.; Agnely, F.; Chaumeil, J. C. A Review of Poloxamer 407 Pharmaceutical and Pharmacological Characteristics. *Pharm Res*, **2006**, *23* (12), 2709–2728. https://doi.org/10.1007/s11095-006-9104-4.
[123] Haug, A. Fractionation of Alginic Acid. *Acta Chem. Scand.*, **1959**, *13* (3), 601–603. https://doi.org/10.3891/acta.chem.scand.13-0601.
[124] Song, W.; Su, X.; Gregory, D. A.; Li, W.; Cai, Z.; Zhao, X. Magnetic Alginate/Chitosan Nanoparticles for Targeted Delivery of Curcumin into Human Breast Cancer Cells. *Nanomaterials (Basel)*, **2018**, *8* (11). https://doi.org/10.3390/nano8110907.
[125] Dutta, P. K.; Ravikumar, M. N. V.; Dutta, J. Chitin and Chitosan for Versatile Applications. *Journal of Macromolecular Science, Part C*, **2002**, *42* (3), 307–354. https://doi.org/10.1081/MC-120006451.
[126] Zargar, V.; Asghari, M.; Dashti, A. A Review on Chitin and Chitosan Polymers: Structure, Chemistry, Solubility, Derivatives, and Applications. *ChemBioEng Reviews*, **2015**, *2* (3), 204–226. https://doi.org/10.1002/cben.201400025.
[127] Thakur, V. K.; Thakur, M. K. Recent Advances in Graft Copolymerization and Applications of Chitosan: A Review. *ACS Sustainable Chem. Eng.*, **2014**, *2* (12), 2637–2652. https://doi.org/10.1021/sc500634p.
[128] Koczkur, K. M.; Mourdikoudis, S.; Polavarapu, L.; Skrabalak, S. E. Polyvinylpyrrolidone (PVP) in Nanoparticle Synthesis. *Dalton Trans.*, **2015**, *44* (41), 17883–17905. https://doi.org/10.1039/C5DT02964C.
[129] Simon, T.; Potara, M.; Gabudean, A.-M.; Licarete, E.; Banciu, M.; Astilean, S. Designing Theranostic Agents Based on Pluronic Stabilized Gold Nanoaggregates Loaded with Methylene Blue for Multimodal Cell Imaging and Enhanced Photodynamic Therapy. *ACS Appl. Mater. Interfaces*, **2015**, *7* (30), 16191–16201. https://doi.org/10.1021/acsami.5b04734.
[130] Arvizo, R.; Bhattacharya, R.; Mukherjee, P. Gold Nanoparticles: Opportunities and Challenges in Nanomedicine. *Expert Opinion on Drug Delivery*, **2010**, *7* (6), 753–763. https://doi.org/10.1517/17425241003777010.
[131] Boisselier, E.; Astruc, D. Gold Nanoparticles in Nanomedicine: Preparations, Imaging, Diagnostics, Therapies and Toxicity. *Chemical Society Reviews*, **2009**, *38* (6), 1759. https://doi.org/10.1039/b806051g.
[132] Sajanlal, P. R.; Sreeprasad, T. S.; Samal, A. K.; Pradeep, T. Anisotropic Nanomaterials: Structure, Growth, Assembly, and Functions. *Nano Rev*, **2011**, *2*. https://doi.org/10.3402/nano.v2i0.5883.
[133] Fales, A.; Crawford, B.; Vo-Dinh, T. Folate Receptor-Targeted Theranostic Nanoconstruct for Surface-Enhanced Raman Scattering Imaging and Photodynamic Therapy. *ACS Omega*, **2016**, *1*, 730–735. https://doi.org/10.1021/acsomega.6b00176.
[134] Rahme, K.; Oberdisse, J.; Schweins, R.; Gaillard, C.; Marty, J.-D.; Mingotaud, C.; Gauffre, F. Pluronics-Stabilized Gold Nanoparticles: Investigation of the Structure of the Polymer-Particle Hybrid. *ChemPhysChem*, **2008**, *9* (15), 2230–2236. https://doi.org/10.1002/cphc.200800358.
[135] Liz-Marzán, L. M.; Giersig, M.; Mulvaney, P. Synthesis of Nanosized Gold−Silica Core−Shell Particles. *Langmuir*, **1996**, *12* (18), 4329–4335. https://doi.org/10.1021/la9601871.

[136] Stöber, W.; Fink, A.; Bohn, E. Controlled Growth of Monodisperse Silica Spheres in the Micron Size Range. *Journal of Colloid and Interface Science*, **1968**, *26* (1), 62–69. https://doi.org/10.1016/0021-9797(68)90272-5.

[137] Shah, K. W.; Sreethawong, T.; Liu, S.-H.; Zhang, S.-Y.; Tan, L. S.; Han, M.-Y. Aqueous Route to Facile, Efficient and Functional Silica Coating of Metal Nanoparticles at Room Temperature. *Nanoscale*, **2014**, *6* (19), 11273–11281. https://doi.org/10.1039/C4NR03306J.

[138] Alonso-Cristobal, P.; Laurenti, M.; Lopez-Cabarcos, E.; Rubio-Retama, J. Efficient Synthesis of Core@shell Fe3O4@Au Nanoparticles. *Mater. Res. Express*, **2015**, *2* (7), 075002. https://doi.org/10.1088/2053-1591/2/7/075002.

[139] Xu, C.; Wang, B.; Sun, S. Dumbbell-like Au–Fe $_3$ O $_4$ Nanoparticles for Target-Specific Platin Delivery. *J. Am. Chem. Soc.*, **2009**, *131* (12), 4216–4217. https://doi.org/10.1021/ja900790v.

[140] Dong, W.; Li, Y.; Niu, D.; Ma, Z.; Gu, J.; Chen, Y.; Zhao, W.; Liu, X.; Liu, C.; Shi, J. Facile Synthesis of Monodisperse Superparamagnetic Fe3O4 Core@hybrid@Au Shell Nanocomposite for Bimodal Imaging and Photothermal Therapy. *Adv. Mater.*, **2011**, *23* (45), 5392–5397. https://doi.org/10.1002/adma.201103521.

[141] Wu, C.-H.; Sokolov, K. Synthesis of Immunotargeted Magneto-Plasmonic Nanoclusters. *Journal of Visualized Experiments*, **2014**, No. 90. https://doi.org/10.3791/52090.

[142] Nguyen, T.; Mammeri, F.; Ammar, S. Iron Oxide and Gold Based Magneto-Plasmonic Nanostructures for Medical Applications: A Review. *Nanomaterials*, **2018**, *8* (3), 149. https://doi.org/10.3390/nano8030149.

[143] Barnett, C. M.; Gueorguieva, M.; Lees, M. R.; McGarvey, D. J.; Darton, R. J.; Hoskins, C. Effect of the Hybrid Composition on the Physicochemical Properties and Morphology of Iron Oxide–Gold Nanoparticles. *J Nanopart Res*, **2012**, *14* (10), 1170. https://doi.org/10.1007/s11051-012-1170-4.

[144] Cai, H.; Li, K.; Li, J.; Wen, S.; Chen, Q.; Shen, M.; Zheng, L.; Zhang, G.; Shi, X. Dendrimer-Assisted Formation of Fe $_3$ O $_4$ /Au Nanocomposite Particles for Targeted Dual Mode CT/MR Imaging of Tumors. *Small*, **2015**, *11* (35), 4584–4593. https://doi.org/10.1002/smll.201500856.

[145] Ji, X.; Shao, R.; Elliott, A. M.; Stafford, R. J.; Esparza-Coss, E.; Bankson, J. A.; Liang, G.; Luo, Z.-P.; Park, K.; Markert, J. T.; et al. Bifunctional Gold Nanoshells with a Superparamagnetic Iron Oxide–Silica Core Suitable for Both MR Imaging and Photothermal Therapy. *J. Phys. Chem. C*, **2007**, *111* (17), 6245–6251. https://doi.org/10.1021/jp0702245.

[146] Mohammad-Beigi, H.; Yaghmaei, S.; Roostaazad, R.; Arpanaei, A. Comparison of Different Strategies for the Assembly of Gold Colloids onto Fe3O4@SiO2 Nanocomposite Particles. *Physica E: Low-dimensional Systems and Nanostructures*, **2013**, *49*, 30–38. https://doi.org/10.1016/j.physe.2013.01.004.

[147] Sun, W.; Mignani, S.; Shen, M.; Shi, X. Dendrimer-Based Magnetic Iron Oxide Nanoparticles: Their Synthesis and Biomedical Applications. *Drug Discovery Today*, **2016**, *21* (12), 1873–1885. https://doi.org/10.1016/j.drudis.2016.06.028.

ANNEX 1. Fluorescence Microscopy as a Tool for Nanomedicine-Cell Interactions Study: Input of Particle Design and of Analytical Strategy

Fluorescence Microscopy as a Tool for Nanomedicine-Cell Interactions Study: Input of Particle Design and of Analytical Strategy

Sanaa Ben Djemaa[1], Mathias Pacaud[1,2], Katel Hervé-Aubert[1], Stéphanie David[1], Emilie Allard-Vannier[1], Emilie Munnier[1], Anastasia Ignatova[3], Amir Fahmi[2], Alexey Feofanov[3,4] and Igor Chourpa[1]

[1.] EA6295 Nanomedicine & Nanoprobes, University of Tours, Tours, France.
[2.] Faculty Technology&Bionics, Rhein-Waal University of Applied Sciences, Kleve, Germany.
[3.] Shemyakin and Ovchinnikov Institute of Bioorganic Chemistry, Russian Academy of Sciences, Moscow, Russia.
[4.] Biological Faculty, Lomonosov Moscow State University, Moscow, Russia.

Various nanomedicine platforms are developed in perspective of disease diagnosis, therapy or theragnosis, namely those based on superparamagnetic iron oxide nanoparticles (SPIONs) and/or gold nanoparticles (AuNPs) [1]. For each nanomedicine platform, one of critical parameters to evaluate is its interaction with target cells, namely its adhesion to cell surface, its internalization, subcellular distribution and action mechanism(s) [2-4]. For this kind of studies, optical microscopy is often used, as it provides physiological and complete view of cells. Some of AuNPs and AgNPs can be detected by dark field microscopy, due to plasmon-enhanced scattering of light. For more specific and spatially resolved optical microscopy of a wide range of metal NPs (MNPs), usual strategy consists in labelling them with fluorescent dyes and detecting them with laser scanning confocal microscopy (LSCM). However, in order to take benefit of the fluorescence microscopy and make relevant conclusions from it, choice of an appropriate particle design and analytical strategy are critical.

Based on our recent studies of fluorescent MNPs coated with various organic shells, we have established several rules [2-4]. First of all, they concern the MNPs fluorescent labelling: (i) covalent binding of the dye can be not enough to ensure its chemical stability – it can be degraded and/or detached from the MNP inside cells; (ii) the dye covalently bound to the MNP core should be hidden under the organic shell (typically under the polymer like polyethylene glycol, PEG), otherwise it can be cleaved from the particle and/or quenched, as well as it may affect the colloidal stability of the particle and its interactions with biological targets. Secondly, relevant assessment of nanoparticle behavior within cells is also dependent on the ability to distinguish the fluorophore attached to the nanoparticles from that one detached from them. The latter is also very important to follow delivery of fluorescent active molecules.

We describe here two analytical strategies helpful in understanding of the fluorescence originating from cells treated with nanomedicine platforms. The first one consisted in using confocal spectral imaging (CSI, made with a LabRam microscope, Horiba SA, France) of the fluorescence (Fig 1): recording full spectra of AlexaFluor488-labelled siRNA from each point of the cell scanned with excitation laser beam (491 nm line of a Calypso 75 laser, Cobolt, France) allowed us to map separately the siRNA loaded into SPION-PEG and the siRNA released to the cytosol (em max at 521 and 527 nm, respectively, Fig 1 C).

The second strategy consisted in adjusting non-spectral LSCM microscope (Model SP2, Leica, Germany) for complementary spatially-resolved analysis of the elastic scattering from AuNPs (633 nm) together with the fluorescence from the Nile Blue dye (exc/em 633/(670-676) nm). This allowed us to establish that MNPs remain attached on the cellular membranes while the released dye enters the cells and accumulated in cytoplasmic vesicles (Fig 2).
To conclude, rational particle design together with innovative analytical approaches based on laser-scanning confocal microscopy (spectral and non-spectral detection of fluorescence and of light scattering) contribute into a reliable understanding of nanomedicine-cell interactions [5].

References:

[1] J Gautier et al. J Control Release **169**(1-2) 2013, p. 48.
[2] J Bruniaux et al. Int J Pharm. **S0378-5173**(17) (2017), p. 30432.
[3] E Allard-Vannier et al. Biochim Biophys Acta **1861**(6) (2017), p. 1578.
[4] E Perillo et al. J Colloid Interface Sci. **499** (2017), p. 209.
[5] The authors acknowledge funding from the following grants in the frames of MINERVA project (ERA-NET RUS PLUS program): RFBR 16-54-76013 (Russia), 01DJ16019 (Germany) and MENESR N°321 (France). We acknowledge also the support from Institut National du Cancer (INCa), Fondation ARC and Ligue Nationale Contre le Cancer (LNCC) (grant ARC_INCa_LNCC_7636).

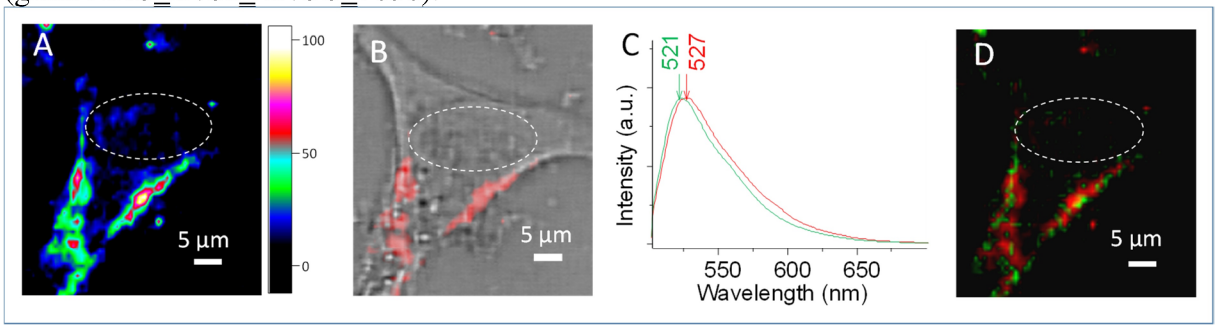

Figure 1. Delivery of siRNA to a live BT474 cancer cell by SPION-PEG nanovectors as studied by CSI: A - map of the total fluorescence intensity distribution over the cell (dashed line indicates nucleus); B – merge of the map A (red zones) with a white-light image of the cell; C – typical fluorescence emission spectra from Alexa 488-labelled siRNA loaded to the nanovectors suspended in PBS (green line) and once delivered to cytosol (red line); D: merge of two spectral maps: siRNA still carried by the nanovectors (green zones seen on the cell membrane) and siRNA released to cytosol (red zones).

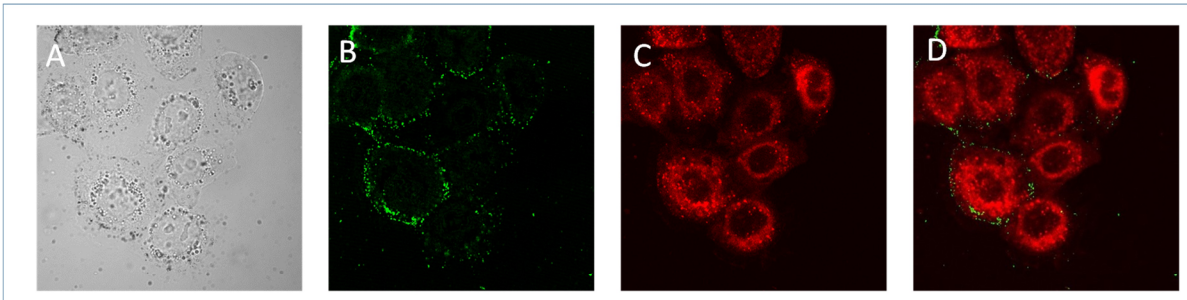

Figure 2. Delivery of fluorescent dye Nile Blue (NB) to SKBR3 cancer cells by plasmonic gold nanoparticles (AuNPs) as studied by LSCM: A – white-light image of cells; B – plasmon-enhanced elastic scattering image shows that AuNPs are mainly accumulated on cell membrane; C – far red fluorescence of NB shows that the dye is internalized and accumulated in vesicular cytoplasmic structures. D – merge of the B and C images.

Résumé

Un immense intérêt est porté sur les nanostructures métalliques anisotropes d'or (AuNFs) qui s'explique par les propriétés uniques qu'elles procurent et qui peuvent servir dans divers domaines, notamment dans le biomédicale. On cherche à maitriser leurs propriétés optiques liées aux oscillations collectives d'électrons de surface appelées plasmons. Elles possèdent une bande de résonance plasmonique localisée de surface (LSPR, comme *localized surface plasmon resonance*) située dans le rouge - proche infrarouge (> 600 nm). Leur capacité d'interagir avec la lumière rouge - proche IR (fenêtre optique biologique) les rend intéressantes en tant qu'agent d'imagerie optique et opto-acoustique. Dans le cas particulier de la diffusion Raman exaltée de surface (SERS, comme *surface-enhanced Raman scattering*), les AuNFs sont capables de procurer les zones d'exaltation à la fois sur les extrémités de leurs pétales et dans les jonctions entre celles-ci, appelées « hot spots ». Ainsi, on peut les utiliser comme substrat SERS sans avoir besoin de les agréger, à la différence des nanosphères d'or. Le protocole de synthèse des AuNFs que nous avons développé est rapide, en une seule étape et n'utilise qu'un nombre réduit de réactifs connus qui sont peu ou pas toxiques. De plus, notre protocole permet de contrôler les caractéristiques des AuNFs telles que leur taille et la position de leur bande LSPR, entre 600 et 900 nm. Afin de garantir une stabilité colloïdale dans des milieux divers, nous avons enrobé nos AuNFs avec des polymères biocompatibles (alginates, chitosan, Pluronics, PVP et PEG) ou les avons encapsulées dans une matrice de silice. Les substrats colloïdaux à base de ces AuNFs enrobées d'enveloppes biocompatibles ont ainsi montré leur potentiel pour procurer l'effet SERS sans agrégation et permettre l'analyse ultrasensible de petits chromophores (comme le Bleu de Nil). De plus, nos résultats montrent que ces nouveaux substrats sont capables de délivrer une charge de molécules dans des cellules cancéreuses. Ainsi, ils semblent prometteurs en tant qu'agents théranostiques, applicables non seulement en SERS, mais également en imagerie optique ou opto-acoustique et en thérapie.

Mots clés: Nanofleurs d'or, AuNF, plasmon de surface, spectroscopie SERS.

Abstract

A huge attention is paid on anisotropic gold metal nanostructures (AuNFs) because of the unique properties they can provide in various fields, in particular the biomedical applications. We are trying to control their optical properties related to the collective oscillations of surface electrons called plasmons. They have a localized surface plasmon resonance band (LSPR) located in the red - near infrared (> 600 nm). Their ability to interact with red light - near IR (optical biological window) makes them interesting as optical and optoacoustic imaging agents. In the specific case of the surface-enhanced Raman scattering (SERS), AuNFs are able to provide enhancement zones both on the tips of their petals and in the junctions between the petals, called "hot spots". Thus, they can be used as SERS substrates without the need to be aggregated, unlike for gold nanospheres. The protocol to synthesize AuNFs that we developed is fast, in one-step and uses only a small number of known reagents that are low or non-toxic. In addition, our protocol allows us to tune the characteristics of the AuNFs such as their size and the position of their LSPR band, between 600 and 900 nm. In order to guarantee their colloidal stability in various media, we have coated our AuNFs with biocompatible polymers (alginates, chitosan, Pluronics, PVP and PEG) or encapsulated them in a silica matrix. Colloidal substrates based on these AuNFs coated with biocompatible envelopes have thus shown their potential to provide the SERS effect without aggregation and allow the ultra-sensitive analysis of small chromophores (such as Nile blue). In addition, our results show that these new substrates are able to deliver a cargo of molecules to the cancer cells. Thus, they seem promising as theranostic agents, applicable not only in SERS, but also in optical or optoacoustic imaging and therapy.

Key words: Gold nanoflowers, AuNF, surface plasmon, SERS spectroscopy.